Venous Perfusion Source Mapping “in Reverse” with Magnetic Resonance Imaging

Ekin Karasan

Electrical Engineering and Computer Sciences
University of California, Berkeley

Technical Report No. UCB/EECS-2024-160
http://www2.eecs.berkeley.edu/Pubs/TechRpts/2024/EECS-2024-160.html

August 8, 2024

Venous Perfusion Source Mapping "in Reverse" with Magnetic Resonance Imaging

by

Ekin Karasan

A dissertation submitted in partial satisfaction of the

requirements for the degree of

Doctor of Philosophy

in

Engineering – Electrical Engineering and Computer Sciences

in the

Graduate Division

of the

University of California, Berkeley

Committee in charge:

Professor Michael Lustig, Chair
Professor Chunlei Liu
Professor Ana Claudia Arias
Professor Christopher Hess

Summer 2024

Venous Perfusion Source Mapping “in Reverse” with Magnetic Resonance Imaging

Abstract

Venous Perfusion Source Mapping "in Reverse" with Magnetic Resonance Imaging

by

Ekin Karasan

Doctor of Philosophy in Engineering – Electrical Engineering and Computer Sciences

University of California, Berkeley

Professor Michael Lustig, Chair

Magnetic resonance imaging (MRI) is a versatile medical imaging modality, which can be used for a variety of applications, including imaging soft tissue structure, measuring functional brain activity by probing blood oxygenation, assessing complex tissue dynamics, and quantifying tissue susceptibility. Measuring complex tissue dynamics such as perfusion and blood flow can offer essential information for diagnosis and provide insights into biophysical functions. Non-contrast enhanced methods to image these dynamics are particularly advantageous as they minimize the risk for patients and improve patient comfort.

While MRI tools for probing blood flow and perfusion are well-established for studying cerebral arterial disorders, the knowledge on the venous drainage mechanism of the brain is much more limited. This is largely attributed to the person-to-person variability in the cerebral venous physiology and the limitations of the current imaging technologies. Venous abnormalities play an important role in several important vascular and neurological conditions. Furthermore, venous effects also contribute significantly to functional MRI (fMRI) based on blood oxygenation level dependent (BOLD) contrast by reducing the spatial specificity of the BOLD signal.

Digital subtraction angiography (DSA) is currently the gold standard to image the venous system, however, it is an invasive procedure that has life-threatening risks. Primary non-invasive and non-contrast enhanced tools to probe the venous system with MRI are phase-contrast (PC) MRI, which probes the instantaneous velocity of blood and time of flight (TOF), which relies on inflow effects. TOF MRI is limited to imaging the venous structure and provides minimal information on flow dynamics. PC MRI requires very large velocity encoding gradients to capture slower flows, significantly increasing echo times, potentially leading to phase offset errors and reducing the accuracy of the measured velocities. Therefore, neither of the techniques can probe the venous system in its entirety.

To address current limitations in venous imaging, this dissertation proposes a novel venous

perfusion source mapping method using Displacement Spectrum (DiSpect) MRI, a non-contrast method that uses blood water as an endogenous contrast agent. This technique encodes spatial information into the magnetization of blood water spins during tagging and remotely detects it once the tagged blood reaches the imaging region – often near the brain's surface, where the signal-to-noise ratio is 3-4× higher. Through repeated spin-tagging and Fourier encoding, this method can resolve the sources of blood water entering the imaging slice across short (10ms) to long (3s) evolution times, effectively capturing venous perfusion sources in reverse. Blood sources can be traced regardless of their path and velocity, enabling measurement of slow blood flow in smaller veins and potentially in capillary beds.

The dissertation first introduces the theory behind DiSpect MRI and describes its application in venous perfusion source mapping in the superior cerebral veins. Next, the sensitivity of the proposed perfusion source mapping technique is established through perfusion modulation using caffeine and its specificity is demonstrated by measuring local perfusion changes during functional activation. Finally, the technique is validated with flow phantom experiments, and several advancements in acquisition techniques are presented.

To my parents and grandmothers

Contents

Contents **ii**

List of Figures **iv**

1 Introduction **1**
1.1 Outline 2

2 MR Imaging of Flow and Perfusion **5**
2.1 Basic MR Physics 5
2.2 Principles of MR Acquisitions 7
2.3 Non-contrast Enhanced Methods to Image Flow and Perfusion 11

3 Displacement Spectrum Imaging **19**
3.1 Introduction 19
3.2 Displacement Encoding with Stimulated Echoes (DENSE) 20
3.3 Displacement Spectrum (DiSpect) Imaging 25
3.4 Methods 31
3.5 Results 33
3.6 Discussion 35
3.7 Conclusion 36

4 Venous Perfusion Source Mapping with DiSpect **37**
4.1 Introduction 37
4.2 Methods 38
4.3 Results 43
4.4 Discussion 45
4.5 Conclusion 47

5 Sensitivity and Specificity of Venous Perfusion Source Mapping **50**
5.1 Introduction 50
5.2 Global Modulation of Venous Perfusion with Caffeine 51
5.3 Local Modulation of Venous Perfusion with Neural Activation 54
5.4 Discussion 66

5.5 Conclusion 69

6 Advances in Venous Perfusion Source Mapping **70**
6.1 Introduction 70
6.2 Methods 70
6.3 Results 76
6.4 Discussion 83
6.5 Conclusion 85

7 Conclusions and Future Work **86**
7.1 Summary of Contributions 86
7.2 Suggestions for Future Work 87

Bibliography **90**

List of Figures

2.1 a) Equilibrium magnetization of a spin in the presence of an external magnetic field B_0. The magnetization (denoted by M) is pointed in the z direction. b) When a B_1 RF pulse tuned to the frequency w_0 is applied, the magnetization rotates towards the transverse plane, while precessing at a frequency ω_0. The corresponding flip angle is denoted by α. 6

2.2 Spatial localization in MRI. a) Variation in precession frequencies occurs based on spatial position when a gradient field is applied in the y direction. Spins at the center ($y = 0$) will be precessing at frequency w_0, while spins at positions $y > 0$ and $y < 0$ will be precessing at frequencies faster and slower than w_0, respectively. b) **Top:** Signal received by the RF coils from three spins at different locations. **Bottom:** A Fourier transform reveals the precession frequency of each spin. . . 8

2.3 Sampling of k-space in MR acquisitions. The sampling rates in each dimension are denoted by Δk_x and Δk_y and the maximum extents covered are k_{xmax} and k_{ymax}. An image can be reconstructed from the sampled k-space by performing an inverse Fourier transform. The FOV and resolution of the reconstructed image are defined as FOV $= \frac{1}{\Delta k}$ and $\delta = \frac{1}{2k_{max}}$. 9

2.4 Common 2D sampling trajectories for k-space. In Cartesian acquisitions, k-space is sampled in a line-by-line fashion. With EPI, multiple k-space lines are sampled in a single acquisition by traversing k-space back and forth. Finally, with Cartesian sampling, k-space is sampled in a non-Cartesian spiral grid. 10

2.5 Slice-selective excitation to excite spins from a thin slice of tissue. a) An RF pulse with a specific frequency bandwidth is played out along with a gradient magnetic field. b) This pulse selectively excites spins that have resonant frequencies within a frequency bandwidth, corresponding to a slice. 10

2.6 Details of PC acquisitions. a) Bipolar gradients and the phase accumulated when these gradients are played out for three spins with different velocities. The accumulated phase is zero for a static spin and increases with increasing velocity. b) In order to eliminate any effects due to background phase, two acquisitions are made with flipped flow encoding gradients. The measured phase from the two acquisitions is subtracted to isolate the phase change due to velocity. c) The maximum velocity that can be mapped is called the encoding velocity, v_{enc}, and the velocities between $\pm v_{enc}$ are mapped to the phase range between $\pm\pi$. . . . 12

2.7 Magnitude and velocity images obtained from a 4D flow acquisition imaging water flowing through a set of tubes. A single coronal slice is displayed. **Left:** Magnitude image showing the direction of flow in the set of tubes. **Middle and Right:** The velocity images for the two in-plane directions, z and x. 13
2.8 Acquisition scheme for FVE MRI with slice-selective 2D imaging. a) To perform a Fourier encoding of the bipolar gradients, multiple acquisitions are performed with incrementing velocity encoding. b) Each acquisition with a set of bipolar gradients will sample another point in the k_v space. Once enough points have been sampled, an inverse Fourier transform can be performed to obtain a velocity spectrum for each image voxel. 14
2.9 Summary of different labeling strategies. **Left:** CASL uses a long, continuous labeling pulse followed by an image acquisition covering the entire brain. **Middle:** PCASL uses a train of shorter RF and gradient pulses instead of a long continuous pulse. **Right:** PASL inverts magnetization in a large slab with a shorter labeling duration. 16
2.10 Vessel-selective ASL. Feeding arteries are selected individually at the neck and the vascular territories can be mapped using ASL. 17

3.1 The difference between velocity and displacement imaging. **Left:** In velocity imaging, the measurement corresponds to the direction in which spins are travelling to at the particular time of imaging. **Right:** With displacement imaging, spins are initially tagged. After a delay period, imaging is performed and the locations from which spins displaced from into the imaging voxel can be traced. 20
3.2 Pulse sequence diagram for DENSE. A 1-1 SPAMM tagging module is applied to cosine modulate the longitudinal magnetization according to the initial position of spins. After a particular mixing time, T_{mixing}, an image is acquired. The image phase is proportional to the displacement that has occurred during the mixing time. 21
3.3 DENSE echo separation. a) An image acquired with DENSE will have stripes due to the cosine modulation during tagging. If we look at the k-space of this image, we observe three echoes. The displacement echo and the conjugate echo are a result of the cosine modulation during tagging. The T_1 echo is due to the T_1 relaxation that occurs during the mixing time. The displacement echo contains the displacement information in its phase and therefore we would like to isolate it. b) In order to isolate the displacement echo, three acquisitions are made by varying the phase of the second RF pulse in the SPAMM module. These three acquisitions are linearly combined to isolate the displacement echo. 23
3.4 DiSpect pulse sequence. a) The pulse sequence is very similar to DENSE, however, instead of making a single acquisition with a single set of displacement encoding gradients, multiple acquisitions with increasing displacement encoding gradients are performed. b) Each acquisition with a different set of displacement encoding gradients samples a new point in the displacement k-space k_d. 24

3.5 Summary of the DiSpect acquisition process. In this example, 2D displacement spectra are acquired by varying the displacement encoding gradients on two axes. For each set of displacement encoding gradients, three phase cyclings are performed to isolate the displacement echo. This isolated displacement echo corresponds to one point in the 2D displacement k-space. The gradients can be incremented to make more acquisitions and fill the 2D displacement k-space. . 26
3.6 Displacement spectra characteristics for different tissue dynamics. For static tissue, it is expected that the displacement spectra will be symmetric and centered at 0. If there is bulk motion, the displacement spectrum will be shifted according to the direction and strength of the motion. In the case of vessel flow, there will be multiple peaks observed in the displacement spectra. The large center peak corresponds to the static tissue in the voxel. The smaller peaks correspond to the blood arriving to the voxel from different branches of the vessel. 27
3.7 DiSpect reconstruction pipeline. For ease of visualization, the reconstruction pipeline is displayed for 1D displacement encoding. The raw data contains three echoes in k-space. Echo separation is performed to obtain the displacement encoded image k-space. Then, regular image reconstruction can be performed to obtain displacement encoded images. Finally, an inverse Fourier transform(s) performed in the displacement encoding dimension(s) results in displacement spectra for each target image voxel. 1D displacement spectra are shown for two example target voxels. 28
3.8 Spatial saturation and selective excitation. a) Spatial saturation bands are applied before and after tagging. The directions of spoiler gradients used for each spatial saturation block are different to avoid any additional stimulated echoes from forming. b) For selective excitation, the non-selective hard RF pulses used during tagging are replaced with selective RF pulses. 29
3.9 Repeated image acquisitions after tagging can be used to obtain the temporal dynamics of flow and perfusion. 30
3.10 Demonstrating the ability of DiSpect to trace the sources of water flowing through a planar set of tubes. a) Experimental setup showing the 3D printed set of tubes connected to a continuous flow pump. b) The axial imaging slice with a target location marked in green. The acquired displacement spectra in the LR and AP directions for the target region are combined to determine the sources of water entering this region. c) Two more target regions are selected and their sources are determined in a similar fashion. 31
3.11 Generating color-coded displacement maps from the displacement spectra. a) Three color filter functions are defined, which equally span the displacement FOV, to give weights to red, green and blue colors based on the amount of displacement. b) These color filters are applied to the displacement spectra of all image voxels. Two color-coded displacement maps are generated corresponding to LR and AP displacement-encoding directions. 32

3.12 In-vivo study demonstrating the ability of DiSpect to trace arterial sources. a) Imaging setup showing the placement of the axial imaging slice and saturation band on the coronal MR angiography image. b) Three regions are selected from the target imaging slice. c) The sources of each target region, measured by DiSpect, are overlaid on the coronal MRA image in the corresponding colors. The sources of each region were traced to the left carotid, right carotid and vertebral arteries. With increasing mixing times, blood coming from sources farther away can be measured. 34

4.1 Perfusion source mapping of the superior sagittal sinus. a) A 2D coronal slice was imaged at the back of the head with a spatial saturation band placed around it to suppress static tissue signal. A DiSpect acquisition with 2D sagittal displacement encoding was performed. b) During the mixing time, blood from the superior veins and capillary beds will drain into the superior sagittal sinus where they will get imaged. c) An ROI containing the superior sagittal sinus was selected from the image. The perfusion source map for the selected ROI at a mixing time of $800ms$ is shown. 40

4.2 Concept of venous perfusion source mapping. a) An axial imaging slice that goes through the superior sagittal sinus and several smaller superior veins is placed at the top of the head. b) 3D view of the superior cerebral veins and the axial imaging slice. Different superior veins will drain into different regions of the imaging slice. While an axial slice is imaged, the tagged spins will hold information to re-trace the sources of blood coming into each image voxel. . . . 41

4.3 Imaging setup for perfusion source mapping of individual superior veins. a) A sagittal image showing the placement of the axial imaging slice and saturation band. b) From the DiSpect acquisition, different vessels that flow through the imaging slice can be identified by examining the displacement spectrum energy of target image voxels and detecting peaks. The detected peaks are overlaid with white ROIs on the image. Four color-coded ROIs are selected out of these regions each containing a different superior vein that drains into the slice. c) The color-coded draining veins overlaid on a 3D QSM-venogram. 42

4.4 The QSM reconstruction pipeline. The magnitude images from the 3D multi-echo GRE acquisition were used to obtain a brain mask [58]. Next, the V-SHARP method is employed for background field removal from the phase images [59]. Finally, dipole inversion was performed using the iLSQR method to obtain QSM images [60]. 42

4.5 Illustration of the differences between PC and QSM venograms. Axial and coronal projections are shown for each case. The QSM venogram can reveal the detailed structure of smaller veins that the PC venogram cannot resolve. Note that some superficial veins are present in the PC venogram but not in the QSM venogram due to the brain mask. 44

4.6 Perfusion source maps at different mixing times depicting the sources of blood draining into the superior sagittal sinus. At the shorter mixing times, the signal is mostly contained in the superior sagittal sinus. At longer mixing times, blood starts arriving from the superior veins lower down. 45
4.7 Perfusion source maps for four target vein ROIs selected from the imaging slice overlaid on the corresponding coronal sections of the QSM-venograms at mixing times from $700ms$ to $1900ms$ in $300ms$ intervals. For each superior vein, the venous territory is marked with a dashed line. 48
4.8 Plotting the 1D mixing time signal series at selected ROIs within venous territories of each superior vein. a) The perfusion source maps are displayed for each vein at a mixing time of 1900ms. Two ROIs are selected from the territory of each vein. b) The perfusion source signal from each ROI is plotted as a percentage of the total source signal entering the target image voxel at that mixing time. It is evident from the 1D signal series that the distribution of perfusion sources shows changes across mixing times. 49

5.1 Summary of BOLD fMRI. a) During neural activation, the blood flow near the activated site increases. This results in a rise in the amount of oxyhemoglobin. b) The rise in oxyhemoglobin increases the local blood oxygenation. BOLD fMRI relies on measuring changes in T_2^*, which increases with higher oxygenation levels. c) In a task-based fMRI study, the subject performs a task on and off and the BOLD signal fluctuates according to a hemodynamic response function. The acquired signal can be fit to a general linear model to identify regions that are activated. 52
5.2 Caffeine study demonstrating the ability of DiSpect to detect global changes in perfusion. a) Imaged slice with two selected vein ROIs. b) Selected veins overlaid on a 3D venogram. c) The blood source maps of the selected veins at two mixing times ($850ms$ and $1600ms$). d) Two color-coded source ROIs are selected from the blood source maps of each vein. The signal amplitude of each ROI is corrected for T_1 decay, normalized by maximum amplitude and plotted at different mixing times for baseline and post-caffeine states. For all ROIs the peak of the baseline signal occurs earlier than post-caffeine suggesting a delayed arrival after caffeine. e) The delay in arrival time was estimated for each source location in the displacement spectra and displayed for a range of $0 - 400ms$. . 53

5.3 Acquisition strategy for the functional study. The DiSpect acquisition is split into 20s partitions, each containing 6 TRs. This corresponds to two points sampled in the displacement k-space. Each partition is repeated during the task and at baseline before moving to the next. A multi-slice Spiral-BOLD acquisition is interleaved between partitions to ensure that activation occurs consistently throughout the scan. Volunteers are instructed to begin and stop the task using automated voice commands. At the end of the acquisition, the acquired data from different partitions is combined to obtain two blood source maps: one at baseline and one during task. 55
5.4 Conceptualization of the detection of local perfusion changes. During neural activation, blood flow and volume in the veins and capillaries within an activated region are modulated. I hypothesize that these perfusion changes can be detected downstream when blood from this region moves into the imaging slice. Some of the blood entering a single target image voxel may come from areas within the activated region, while some may come from surrounding non-activated regions. 56
5.5 Overview of BOLD fMRI processing. The acquired raw image time series is pre-processed by performing realignment, slice-timing correction, co-registration to the 3D QSM volume and smoothing with a kernel size of 3x3x3mm^3. The pre-processed data is then fit to a general linear model and statistical inference is performed to obtain t-statistic images with a significance threshold of $p < 0.01$. 57
5.6 Processing setup for bilateral motor cortex activation in Subject 1. a) Imaging slice showing four selected veins: two (orange) drain the activated motor cortices and two (blue) that do not and used as control. b) The color-coded veins overlaid on a 3D QSM-venogram. c) BOLD activations (green) overlaid on the 3D QSM-venogram showing bilateral motor cortex activation. 58
5.7 Results for bilateral motor cortex activation in Subject 1. **Top:** Perfusion source maps for activated and control veins at two mixing times. **Middle:** The percentage change showing mostly positive and some negative percentage differences in veins draining the activated regions. Little or no percentage change is observed in the veins selected as control. Bottom: BOLD activation map for the coronal sections containing each vein. Venous territories are marked with yellow dashed lines. 59
5.8 Left motor cortex activation in Subject 2. a) Imaging slice showing two selected veins: one (orange) drains the activated left motor cortex and one (blue) is selected as control. b) The color-coded veins overlaid on a 3D QSM-venogram. c) BOLD activations (green) overlaid on the 3D QSM-venogram. d) **Top:** Perfusion source image for activated and control veins at two mixing times. **Middle:** The percentage change showing positive local changes near the BOLD activated regions. **Bottom:** BOLD activation map for the coronal sections containing each vein. Venous territories are marked with yellow dashed lines. 60

5.9 Repeatability analysis for Subject 1. Percentage change in perfusion source maps at three mixing times for the vein draining the right motor cortex shown for the initial and repeat scans. BOLD activations (green) of the coronal section containing the vein are shown as a reference on the bottom. To visualize functionally activated regions in more detail, the BOLD activations are shown with a higher significance threshold on the right bottom corner. The initial and repeat scans show good overlap, in regions that exhibit positive and negative percentage change. Note that the scans were performed on different sessions leading to some differences in the head orientation and imaging slice position. Venous territories are marked with yellow dashed lines. 62
5.10 Repeatability analysis for Subject 2. Percentage change in perfusion source maps at three mixing times for the vein draining the left motor cortex shown for the initial and repeat scans. BOLD activations (green) of the coronal section containing the vein are shown as a reference on the bottom. The initial and repeat scans show good overlap, in regions that exhibit positive percentage change. Note that the scans were performed on different sessions leading to some differences in the head orientation and imaging slice position. Venous territories are marked with yellow dashed lines. 63
5.11 ROI analysis for Subject 1. a) BOLD activations (green) of the coronal section containing the vein draining the right motor cortex. b) Two ROIs are selected from the venous territory and their normalized perfusion source map amplitude during task (orange) and at baseline (blue) are shown across mixing times for the first scan and repeat scan. The first ROI shows consistent increase in source signal amplitude while the second ROI shows consistent decrease. 64
5.12 ROI analysis for Subject 2. a) BOLD activations (green) of the coronal section containing the vein draining the left motor cortex. b) Two ROIs are selected from the venous territory and their normalized perfusion source map amplitude during task (orange) and at baseline (blue) are shown across mixing times for the first scan and repeat scan. The first ROI shows consistent increase in source signal amplitude while the second ROI shows no change. 65
5.13 DiSpect T-test results for Subject 1 with bilateral activation (left) and Subject 2 with unilateral left motor cortex activation (right). For Subject 1 with bilateral activation, regions with significant changes in perfusion source signal amplitude are identified in veins draining both motor cortices, whereas for Subject 2, significant changes are only identified in the vein draining the left motor cortex. 66

5.14 Analysis of Spiral BOLD acquisitions at the beginning of DiSpect partitions for the first scan of each subject. a) EPI BOLD activations for the coronal sections containing veins draining left and right motor cortices of each subject. Three ROIs are selected on the activated regions determined by the commercial BOLD acquisition. b) The percent modulation for each ROI measured by the custom Spiral-BOLD performed at each DiSpect partition is displayed across the entire acquisition. Red markers indicate the last Spiral-BOLD acquisition performed during task and green markers indicate the last Spiral-BOLD acquisition performed during rest. All three regions exhibit consistent activation throughout the scan. 67

6.1 Setup for flow phantom experiment mimicking the superior cerebral veins. a) A phantom is constructed and 3D printed to mimic the superior cerebral veins. The phantom is placed in a large pool and a peristaltic pump is used to draw water out of the tubes. As water is drawn out, more water gets drawn into the tubes from the main pool (as shown by the white arrows). The placement of the imaging slice and spatial saturation band for the DiSpect acquisition are shown. b) Coronal and c) Sagittal View of the phantom marking four sets of tubes in different colors. Tubes shown in each color carry flow into a different location within the imaging slice. 71

6.2 DAVF angiographic stages: no fistula, low risk DAVF and high risk DAVF. In the case where there is no fistula, cortical veins drain normally into the sinus. When there is a low risk DAVF, arteries form direct connections into the veins, however, there is no cortical flow reversal. With a high risk DAVF, cortical flow reversal is observed where blood from the arteries directly drain into the cortical veins, reversing the direction of blood flow. 73

6.3 Flow phantom experiment to demonstrate the potential of DiSpect to risk-stratify DAVFs. a) The phantom was constructed to simulate flow in a cortical vein located near a DAVF. An imaging slice was positioned to cover the cortical vein and sinus. b) The pump was connected in two configurations to simulate low risk and high risk DAVFs. 74

6.4 Setup for two-slice DiSpect acquisition. a) Two slices are selected to image the superior (top) and deep (bottom) cerebral veins. b) The two imaging slices with vein ROIs selected in different colors. c) Modified pulse sequence showing two slices acquired consecutively for each of the repeated image acquisitions after tagging. 75

6.5 3D displacement encoding. a) A sagittal projection of the 3D QSM-venogram showing the axial imaging slice placed lower down in the head. b) Three target vein ROIs are selected from the imaging slice and shown in different colors. The sources of each vein ROI will come from a smaller region below it. 76

6.6 Results for flow phantom mimicking the superior veins. The source maps for image voxels containing the four tubes are shown for mixing times of $1300ms$, $2800ms$ and $4300ms$. For the tubes with slower flows (green and blue) the source maps show water coming from within the tubes, while for the faster flowing tubes (yellow and red) water comes from within the tubes as well as from the main water pool. 77
6.7 Results of particle trajectory simulations from the 4D flow acquisitions. a) A coronal slice of the velocity maps in the z (left) and x (right) directions for one set of tubes. The measured velocities are shown for the range between -3 and 3 cm/s. b) Example particle trajectories simulated from regions selected towards the bottom of the tubes. c) A comparison between the **Top:** simulated source maps from the particle trajectories and **Bottom:** measured source maps from DiSpect. While the measured and simulated source maps show good overlap for the shorter mixing times, there are several discrepancies at the longer mixing times as shown by the red arrows. The simulated source maps from the 4D flow acquisition completely miss water coming from one region of the tubes. 78
6.8 Results for the flow phantom simulating **left:** low risk and **right:** high risk DAVFs. The source maps for the image voxels containing cortical vein and sinus tubes are shown for low risk and high risk configurations at three mixing times. For the low risk scenario (left) source maps show that water in the cortical vein comes from upstream venous flow whereas for the high risk scenario (right) source maps show water coming from the fistula. 80
6.9 Perfusion source maps for five vein ROIs selected from the **top** slice of the two-slice acquisition are overlaid on the corresponding sagittal section of the PC venogram. The maps are shown at mixing times of $450ms$, $900ms$ and $1350ms$ in the corresponding colors. The imaging slice with the selected vein ROIs is shown at the top as a reference. 81
6.10 Perfusion source maps for five vein ROIs selected from the **bottom** slice of the two-slice acquisition are overlaid on the corresponding sagittal section of the PC venogram. The maps are shown at mixing times of $450ms$, $900ms$ and $1350ms$ in the corresponding colors. The imaging slice with the selected vein ROIs is shown at the top as a reference. 82
6.11 3D perfusion source maps at a mixing time of $1200ms$ overlaid on a 3D QSM-venogram. The source maps are shown at two orientations for each vein. The orientation of each image is depicted with the corresponding orientation marker. 83

7.1 The perfusion source maps for four superior veins shown at different evolution times demonstrating the ability to trace the sources of blood in individual veins. 87

Acknowledgments

I always found the acknowledgements of dissertations very intriguing as they somewhat summarize the PhD journeys. I am very excited to be writing the acknowledgements for my dissertation.

First and foremost, I would like to express my deepest gratitude to Miki, who has been a great advisor, mentor and teacher. Throughout my PhD, I always felt your full support and knew that you always had my best interest in mind. Whenever I had any roadblock in my research, you provided me with the perfect resources and guidance that I needed. You were always extremely generous with your time. You stayed up late to help me debug flow phantom experiments and spent many motionless hours inside the scanner for my crazy scans. On top of academic settings, you also offered your full support when I had any issues outside of research. I believe that MikGroup has an amazingly positive group dynamic and we owe a lot of that to you. I am very grateful to have been part of your group for the last six years, which have undoubtedly been some of my best years.

I would also like to thank my dissertation committee members: Chunlei Liu, Ana Arias and Christopher Hess. Chunlei, thank you so much for giving me the opportunity to come to Berkeley and always being a great source of support and guidance throughout my PhD. Thank you for joining many of my meetings with Miki, whenever he knocked on your wall, and for inviting me to your group events. Ana, thank you for all of your positive energy and hugs throughout the years. I truly appreciate all of the encouragement you gave me when I needed it the most. Prof. Hess, thank you so much for all your insights and for helping us find a clinical application for our method.

Throughout my PhD, I have been fortunate to collaborate with many researchers. In my first project, I was extremely lucky to work with our collaborators from GE: Fraser Robb and Victor Taracila. Thank you so much for being so supportive, even though I had no prior experience in the area. I really enjoyed having meetings with you and I truly learned a lot through this project. I would like to thank Prof. Peder Larson for helping me use the scanner at UCSF and letting me shadow their experiments. I would also like to express my gratitude to Prof. Shreyas Vasanwala for all of the support and resources. Finally, I would like to thank our collaborators from UCSF, David Saloner and Matt Amans, for their support in translating our method to the clinic and for hosting me at UCSF to shadow an experiment. I am very excited to continue our collaboration.

When I first joined MikGroup, I was welcomed by a very supportive and collaborative environment. My greatest mentor Zhiyong, a.k.a ZZ/Shuayong, you taught me so much in such a short time. I truly appreciate your positive attitude and constant energy that inspired me to work harder. I am so lucky to have had a mentor like you and I am very happy that I get to see you every year at ISMRM. Hopefully, I can come visit you in China very soon! Jon, thank you so much for being an amazing mentor throughout the years. You are extremely knowledgeable, kind and full of amazing ideas. I was very lucky to have your continuous support and guidance starting from my first year at Berkeley. Karthik, thank you so much for teaching me a lot of what I know about building hardware. You were very

patient with me and answered all of my simple questions. I am very glad that you are back in the group again, it is great to have you! Frank, thank you for giving many Ueckerfests to get us started in our first year.

I would also like to thank other past and current MikGroup members: Ke, Suma, Shreya, Alfredo, Julian, Rebekah, Alan, Efrat, Katie, Alison, Naz, Xucheng, Michael, Volkert and Anita. Ke, you have been one of the highlights of my PhD and I could not imagine this journey without you. Thank you for making me smile and laugh so much. I have so many fun memories from the last six years and I think most of them involve you. You are so kind, supportive and positive and I am very lucky to have a friend like you. I hope that I can get to see you more when you move back to the Bay!

Suma, I am so lucky to have a labmate like you. Thank you for always being there to support and help me whenever I needed. You always provided extremely helpful suggestions whenever I presented at meetings. I really learned a lot from you over these years and will truly miss you when you graduate.

Shreya, I really do not know what I would do without you. Thank you for always being a shoulder to rely on and a person to go to whenever I needed help. Whenever I see and talk to you I feel extremely comfortable and happy. You are truly an amazing person and I am so lucky to have you as a friend. Thank you for being such a thoughtful and generous person.

Rebekah, I think you are the only person who can make me laugh when I am very upset. Thank you for being my housemate for 5+ years. You always push me to be better and call me out whenever I am being lazy. Whenever I need someone to talk to, you are always there for me and listen to me. My PhD experience would have been much more dull and boring without you, thank you so much for being there!

Alfredo, I think you are the most efficient person I have met in my life, I am truly inspired to be more like you. Thank you for always answering my very simple questions about servers and helping me whenever I have any issues. I am very grateful that during one of the hardest times in my PhD, you were there for me and helped me get through it. Also, thank you for helping me improve my skiing, hopefully I can actually get better one day!

Julian, thank you for bringing so much energy to the group. Whenever I work and interact with you, it is really a pleasure. I am so amazed by how much you learned and developed over the last four years and thank you for teaching me so much in the process as well. You are an amazing friend and collaborator and I am so lucky to have you.

Efrat, I am grateful to have you as a mentor and friend. Thank you for being so supportive. Your guidance really means a lot to me. Alison, thank you so much for working with me on the traps project, I really would not have been able to do it without you! Katie, you bring me so much energy and excitement. Thank you for volunteering for my scans so many times and for being an amazing labmate and roommate.

I would also like to thank my friends in Liu and Arias groups: Tanya, Engin, Jingjia, Victor, Jasmine and Yuhan. Tanya, you are an amazing friend, I am so grateful to have you. Thank you so much for always being there for me no matter what and always knowing when

I needed help. I am always very happy when I see you in the office and you always brighten my day. I am extremely lucky to have a friend like you.

Engin, even though you stayed here for only one year you made such a big impact on my life. I cannot imagine my PhD journey without you. You are such a positive, kind, patient and supportive person. I wish you could have been at Berkeley for more years but I am grateful that you will always be part of my life.

Jingjia, you are one of the sweetest and funniest people I know. I hope you will come visit Turkey again and we will finally get to go to Cappadocia together. Victor, you are one of the most creative people I know and I am always very inspired by you. I am sure you will have a very successful career ahead of you.

I would also like to thank other members of the Turkish Mafia: Efe Sr., Efe Jr., Kadircan, Oguzhan, Baturalp. I had some of the best times with you and I hope we have many more! Rozhan, thank you so much for being such an amazing housemate. I loved driving together to work every day. I am really sad that you are not at the house anymore but I hope I will get to see you regularly. Naz, thank you for always brightening my day whenever you come to talk to me. I am glad you will still be around for many more years!

Lastly, I would to extend my greatest love and gratitude to my parents and my grandmothers. My parents were my greatest inspiration to pursue a PhD. Mom and Dad, I always felt your endless love and support even though we were many thousands of miles away. Whenever I had any problem, you were always there to help me and guide me through it. I really could not have done this without you. Thank you for being the best parents I could have ever asked for, you are my greatest luck in life. My grandmothers, thank you for always believing that I could do anything. Thank you for giving me so much love constantly.

Chapter 1

Introduction

Magnetic resonance imaging (MRI) is a powerful and versatile imaging modality. MRI leverages the spin angular momentum that the nuclei in atoms with an odd number of protons/neutrons exhibit. These nuclei can be considered as spinning charges, or spins, that produce a small magnetic moment. Magnetic fields are used to manipulate these spins and produce a signal. Most commonly, hydrogen spins in water are imaged in MRI, which are abundantly found in the human body. Unlike many other medical imaging modalities such as X-ray, Computed Tomography (CT), Positron Emission Tomography (PET), MRI requires no ionizing radiation, making it a safer option for human subjects.

MRI is used for a variety of applications, including imaging soft tissue structure, measuring functional brain activity by probing blood oxygenation, assessing water diffusion, flow as well as perfusion, and quantifying tissue susceptibility. Measuring perfusion and blood flow can offer essential information for diagnosis and provide insights into biophysical functions [1–3]. Contrast enhanced tools to probe these dynamics, such as dynamic contrast enhanced (DCE) [4] MRI and dynamic susceptibility contrast (DSC) [5] MRI require injecting a contrast agent intravenously to alter the magnetic properties of blood water spins. Non-contrast enhanced methods are particularly advantageous as they minimize the risk for patients and improve patient comfort. These include phase-contrast (PC) MRI [2, 6], which probes the instantaneous velocity of blood, arterial spin labeling (ASL) [7, 8], which uses blood water as an endogenous tracer to measure tissue perfusion, and time of flight (TOF) MRI, which relies on inflow effects.

While MRI tools for probing blood flow and perfusion are well-established for studying cerebral arterial disorders, the knowledge on the venous drainage mechanism of the brain is much more limited [9]. This is largely attributed to the person-to-person variability in the cerebral venous physiology and the limitations of the current imaging technologies [10]. Nevertheless, venous abnormalities play an important role in several important vascular conditions such as venous sinus thrombosis [11], dural arteriovenous fistulas [12], and idiopathic intracranial hypertension [13]. Emerging evidence suggests potential venous involvement in several other neurological disorders including multiple sclerosis, idiopathic Parkinson's disease, leukoaraiosis and normal-pressure hydrocephalus [14, 15]. Additionally, improved

venous imaging methods could reveal the interplay between venous and cerebrospinal fluid (CSF) flows and pressures [16].

Venous effects also contribute significantly to functional MRI (fMRI) based on blood oxygenation level dependent (BOLD) contrast. Veins draining the site of neural activity may carry BOLD signals that are displaced from the activated site. This mis-localization of neural activation limits the spatial specificity of the BOLD signal [17–20]. In addition, there is a limited understanding on how the changes in venous blood flow are regulated during functional activation. Non invasive methods that measure perfusion, flow and volume may help decipher the underlying complex biophysics.

Digital subtraction angiography (DSA) is currently the gold standard to image many vascular disorders involving the venous system, however, it is an invasive procedure that has life-threatening stroke risks [21, 22]. Time-resolved DCE MRI is an alternative non-invasive tool to study the venous system, however, it is less reliable than DSA, and requires exogenous contrast agents [23]. While ASL is frequently used to study arterial perfusion, it is not suitable for veins due to the lack of a single labeling plane. Primary non-invasive tools to probe the venous system are TOF and PC MRI [9, 24, 25]. TOF MRI is limited to imaging the venous structure and provides minimal information on flow dynamics. PC MRI requires very large velocity encoding gradients to capture slower flows, significantly increasing echo times, potentially leading to phase offset errors and reducing the accuracy of the measured velocities [26]. Therefore, it is mainly limited to probing flow velocity in sinuses and larger veins.

To address current limitations in venous imaging, this dissertation describes a novel venous perfusion source mapping method using Displacement Spectrum (DiSpect) MRI, a non-contrast method that uses blood water as an endogenous contrast agent. This technique encodes spatial information into the magnetization of blood water spins during tagging and remotely detects it once the tagged blood reaches the imaging region – often near the brain's surface, where the signal-to-noise ratio is 3-4× higher. Through repeated spin-tagging and Fourier encoding, this method can resolve the sources of blood water entering the imaging slice across short (10ms) to long (3s) evolution times, effectively capturing venous perfusion sources in reverse. Blood sources can be traced regardless of their path and velocity, enabling measurement of slow blood flow in smaller veins and potentially in capillary beds. This dissertation first introduces DiSpect MRI and then demonstrates perfusion source mapping in the superior cerebral veins. The sensitivity and the specificity of the novel perfusion source mapping technique are established with a caffeine study and by measuring local perfusion modulation due to neural activation.

1.1 Outline

The remainder of this dissertation is organized as follows:

Chapter 2: MR Imaging of Flow and Perfusion

This chapter provides an overview of MRI physics and principles of MR acquisitions to equip the readers with the preliminaries for understanding the subsequent chapters. First, I will review how the components of the MRI system can be used to manipulate spins. Then, I will present the frequency domain perspective of MRI and introduce the MR signal equation. Finally, I will describe two non-contrast enhanced MRI methods to image blood flow and perfusion: PC MRI and ASL.

Chapter 3: Displacement Spectrum Imaging

This chapter will introduce DiSpect, a highly versatile technique for probing various complex tissue dynamics. DiSpect is a Fourier encoding variant of a Displacement Encoding with Stimulated Echoes (DENSE), which can measure bulk displacement. First the theory behind DENSE and DiSpect acquisitions will be presented. Next, I will detail the processing of the rich DiSpect dataset. Finally, I will present a validation of DiSpect using flow phantom and in-vivo experiments.

Chapter 4: Venous Perfusion Source Mapping with DiSpect

Leveraging DiSpect, I propose a novel venous perfusion source mapping method, which can dynamically trace venous perfusion sources in reverse. This technique can track blood sources regardless of their path and velocity, allowing the measurement of both faster blood flow in the sinuses and slower flow in smaller veins and capillary beds in a single acquisition. Through experiments, I show that venous perfusion source mapping can be used to trace the sources of blood in individual superior veins.

Chapter 5: Sensitivity and Specificity of Venous Perfusion Source Mapping

In this chapter, I establish the sensitivity and specificity of venous perfusion source mapping through a series of experiments. First, I present results from a caffeine study, demonstrating that the proposed method is sensitive to global venous perfusion changes. Then, I show its specificity to local perfusion changes during functional activation in two subjects.

Chapter 6: Advances in Venous Perfusion Source Mapping

In this chapter, I will present results from flow phantom experiments to validate this method and to demonstrate its clinical potential. Following this, I will show several advancements in acquisition techniques, including multi-slice imaging and 3D displacement encoding.

Chapter 7: Conclusions and Future Work

This chapter gives an overview of the methods described in this dissertation and discusses potential future directions.

Chapter 2

MR Imaging of Flow and Perfusion

This chapter aims to give an overview of fundamental MRI principles and image acquisition techniques to enhance understanding of the methods developed in this dissertation. It covers the basic physics underlying MRI and the principles governing MR acquisitions. Additionally, I describe two non-contrast MRI methods for probing the dynamics of flow and perfusion and discuss the remaining challenges in this area.

For readers seeking a more fundamental understanding of MR imaging, I recommend Nishimura's excellent book, "Principles of Magnetic Resonance Imaging" [27].

2.1 Basic MR Physics

Atoms with an odd number of protons, such as hydrogen, can be visualized as spinning charges that produce a small magnetic moment. MRI is composed of the interaction of these nuclear spinning charges, called spins, with three magnetic fields: main static magnetic field (B_0), radiofrequency (RF) field (B_1), and linear gradient field (G).

Without an external magnetic field, the nuclear spins are oriented randomly. When placed in the large static B_0 field, the spins align in parallel or anti-parallel with the direction of the main magnetic field, called the longitudinal or z-direction (Figure 2.1a). The spins also start to precess at the Larmor frequency, $\omega_0 = \gamma B_0$, where γ is a constant called the gyromagnetic ratio that depends on the nuclei.

In order to obtain a signal from spins an RF (B_1) pulse, which is tuned to the frequency w_0, is applied in the transverse (xy) plane to excite or rotate these spins (Figure 2.1b). The angle of rotation that the spins experience, or flip angle (α), depends on the strength and duration of the B_1 pulse. A 90^o flip angle corresponds to the spins being fully rotated into the transverse plane. Based on Faraday's law of induction, the rotating magnetization vectors of spins induce an electromotive force on an RF receiver coil placed nearby. The received signal from these RF coils are processed to obtain MR images.

After the RF pulse is turned off, the magnetization (M) starts to return back to its equilibrium state at the presence of a B_0 field. This process occurs through two mechanisms.

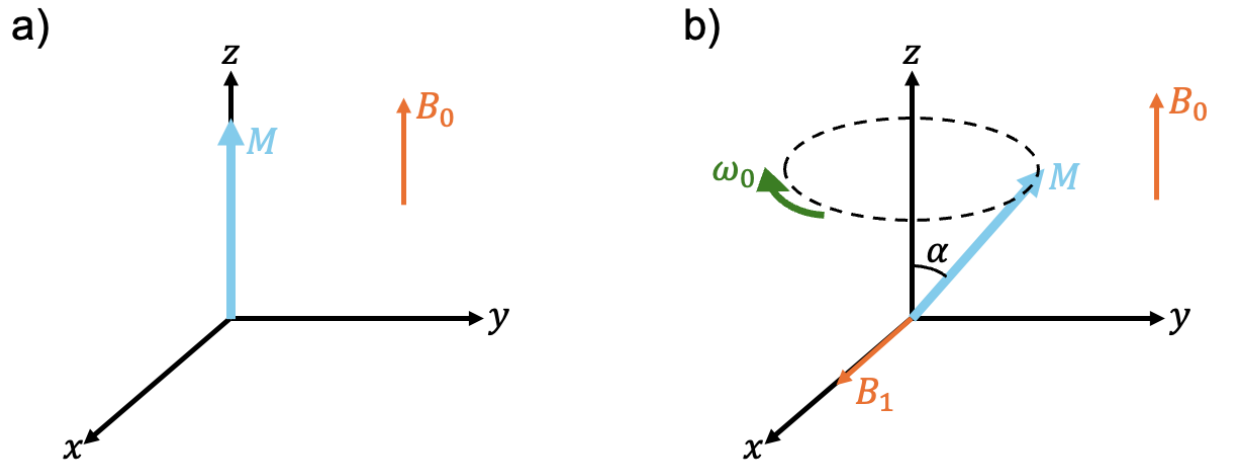

Figure 2.1: a) Equilibrium magnetization of a spin in the presence of an external magnetic field B_0. The magnetization (denoted by M) is pointed in the z direction. b) When a B_1 RF pulse tuned to the frequency w_0 is applied, the magnetization rotates towards the transverse plane, while precessing at a frequency ω_0. The corresponding flip angle is denoted by α.

The longitudinal magnetization exponentially recovers to the equilibrium magnetization with a time constant T_1. On the other hand, the transverse magnetization exponentially decays back to 0 with a time constant T_2. These relaxation time constants, T_1 and T_2, have specific values for different tissue types, with T_1 always longer than T_2. The equations for T_1 recovery and T_2 relaxation are given by

$$M_z(t) = M_z(0)e^{\frac{-t}{T_1}} + M_0(1 - e^{\frac{-t}{T_1}}), \tag{2.1}$$

$$M_{xy}(t) = M_{xy}(0)e^{\frac{-t}{T_2}}, \tag{2.2}$$

where M_z and M_{xy} are the longitudinal and transverse magnetizations respectively, M_0 is the magnitude of the magnetization at equilibrium and $M_z(0)$ and $M_{xy}(0)$ are the initial conditions for each magnetization. Assuming that $M_z(0) = 0$ and $M_{xy}(0) = M_0$ these equations become

$$M_z(t) = M_0(1 - e^{\frac{-t}{T_1}}), \tag{2.3}$$

$$M_{xy}(t) = M_0e^{\frac{-t}{T_2}}. \tag{2.4}$$

It is important to note that the measured decay of the transverse magnetization is often faster than the intrinsic T_2 decay. This faster decay is due to effects of magnetic field inhomogeneities in the static field B_0 as well as magnetic susceptibility differences in the tissue. This faster decay time constant is denoted by T_2^*.

To achieve spatial localization of spins, linearly varying gradient fields, which create a linear mapping between spatial positions and precession frequencies of spins, are used. For example, if a gradient field G_y is applied along the y dimension, the spatially varying magnetic field would be $B(y) = B_0 + G_y y$. This will in turn result in spatially varying precession frequencies $w(y) = \omega_0 + \gamma G_y y$ (Figure 2.2a). The measured time signal series by the RF receive coils will consist of contributions from all precessing spins, resulting in a superposition of signals at various frequencies. A Fourier transform of this signal can determine the contribution from each precession frequency, which linearly maps to spatial positions (Figure 2.2b).

2.2 Principles of MR Acquisitions

k-space

The signal time series picked up by the RF coils can be expressed as

$$s(t) = \int_{\vec{r}} M_{xy}(\vec{r}) e^{-i\phi(\vec{r},t)} d\vec{r} \tag{2.5}$$

where $M_{xy}(\vec{r})$ is the total transverse magnetization at position $\vec{r}$ and $\phi(\vec{r}, t)$ is the phase of the magnetization at that position. The phase factor, $\phi(\vec{r}, t)$, is given by

$$\phi(\vec{r}, t) = \gamma \int_0^t B_0 d\tau + \gamma \int_0^t \vec{r} \cdot \vec{G}(\tau) d\tau = \omega_0 t + 2\pi \vec{k}(t) \cdot \vec{r}. \tag{2.6}$$

By demodulating the signal equation at a carrier frequency $e^{-i\omega_0 t}$ and making substitutions we obtain the final signal equation

$$s(t) = \int_{\vec{r}} M_{xy}(\vec{r}) e^{-i2\pi \vec{k}(t)\cdot\vec{r}} d\vec{r}. \tag{2.7}$$

This signal equation can be further expressed as

$$s(t) = M(\vec{k}(t)) \tag{2.8}$$

where $M(\vec{k}(t))$ is the Fourier transform of $M_{xy}(\vec{r})$. The locations, $\vec{k}(t)$, denote spatial frequencies called the k-space. The gradients can be varied to traverse to different locations of the k-space. Once the k-space has been sufficiently sampled, an image is obtained by performing an inverse Fourier transform.

Sampling

Most commonly, in MR acquisitions k-space is sampled in a Cartesian grid as shown in Figure 2.3. The distances between consecutive samples, or the sampling rates, are denoted

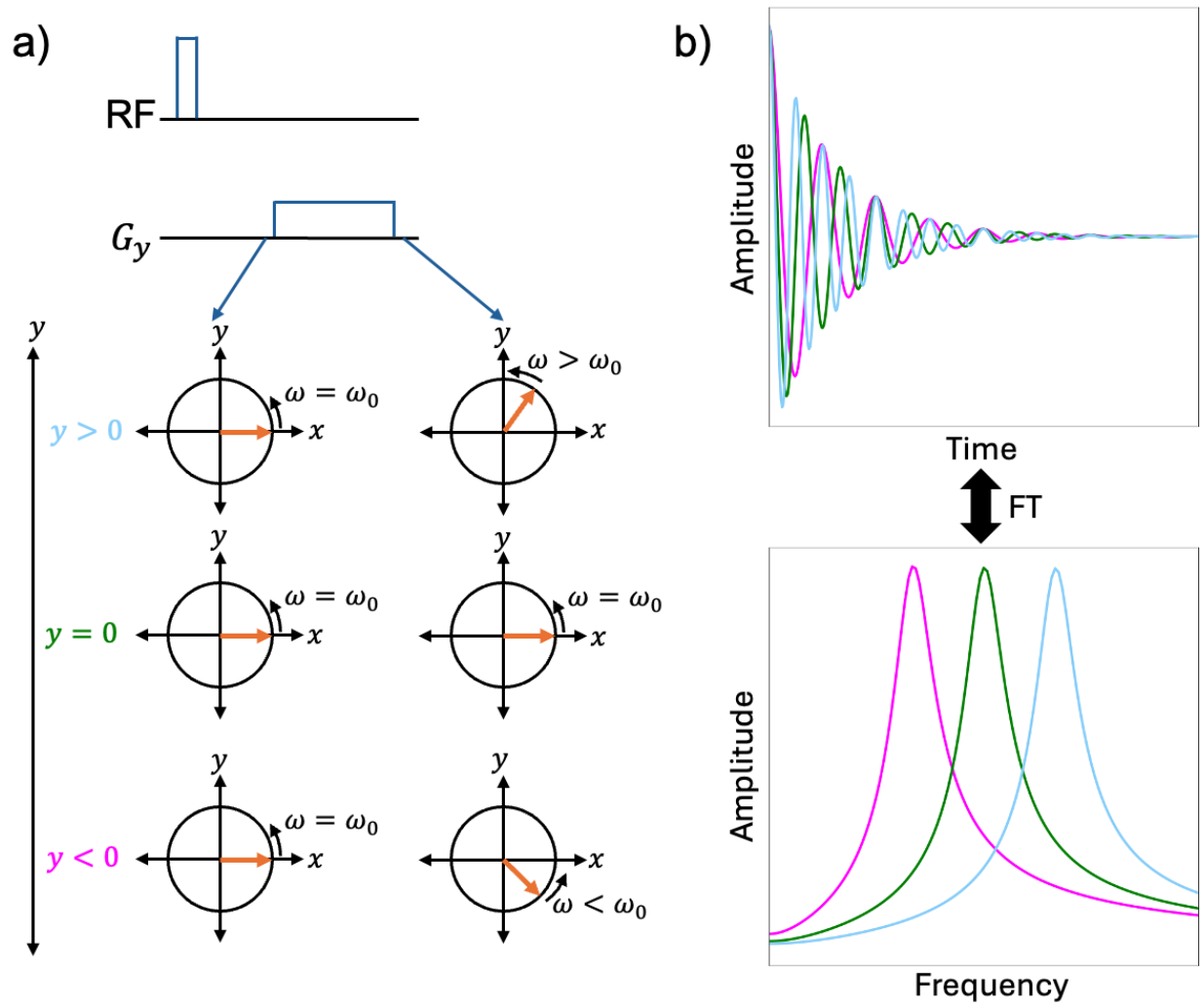

Figure 2.2: Spatial localization in MRI. a) Variation in precession frequencies occurs based on spatial position when a gradient field is applied in the y direction. Spins at the center ($y = 0$) will be precessing at frequency w_0, while spins at positions $y > 0$ and $y < 0$ will be precessing at frequencies faster and slower than w_0, respectively. b) **Top:** Signal received by the RF coils from three spins at different locations. **Bottom:** A Fourier transform reveals the precession frequency of each spin.

by Δk_x and Δk_y and the maximum k-space extents covered are denoted by k_{xmax} and k_{ymax}. According to the Nyquist theorem, the k-space sampling rate determines the field of view (FOV) that can be reconstructed without aliasing: FOV $= \frac{1}{\Delta k}$. On the other hand, the resolution (δ) of an MR image depends on the extent of k-space covered, where $\delta = \frac{1}{2k_{max}}$.

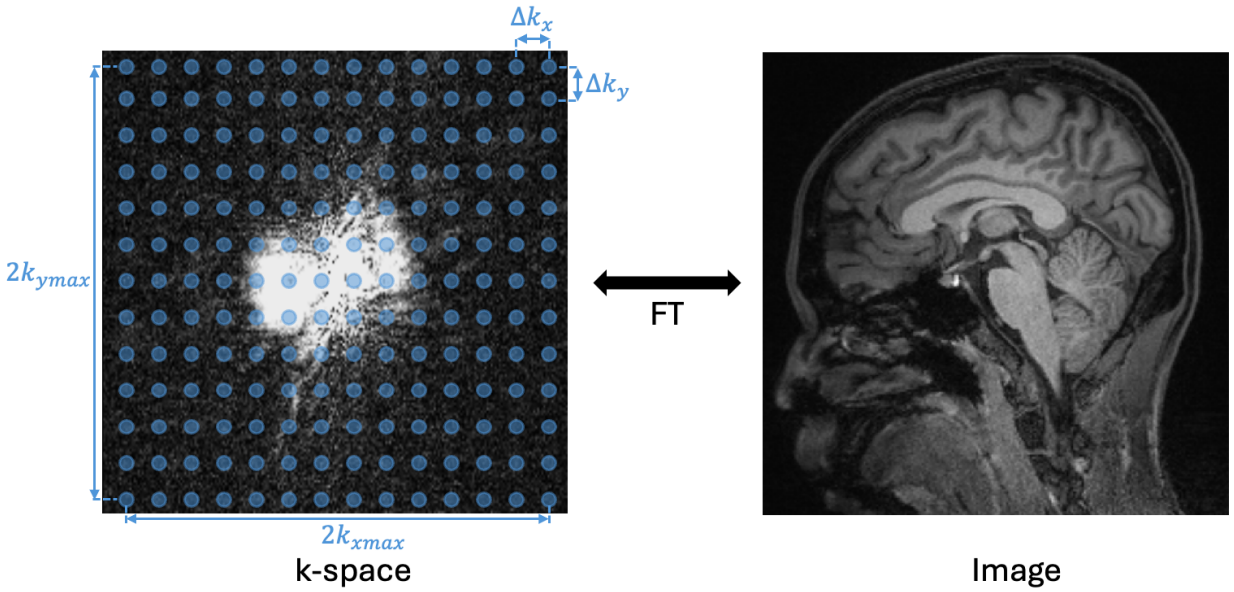

Figure 2.3: Sampling of k-space in MR acquisitions. The sampling rates in each dimension are denoted by Δk_x and Δk_y and the maximum extents covered are k_{xmax} and k_{ymax}. An image can be reconstructed from the sampled k-space by performing an inverse Fourier transform. The FOV and resolution of the reconstructed image are defined as FOV $= \frac{1}{\Delta k}$ and $\delta = \frac{1}{2k_{max}}$.

k-space Sampling Trajectories

Due to physical constraints of the MRI scanner, the k-space points need to be to be sampled consecutively, constrained by the gradient amplitude and slew rate of the hardware. The most common sampling strategy is to acquire the k-space in a line-by-line fashion. However, this is very time consuming as only a single line is sampled at each acquisition. Many acquisitions need to be performed to sufficiently sample the entire k-space. More efficient k-space sampling schemes exist where a larger portion of k-space, or possibly the entire k-space, is covered in a single acquisition. Two examples of such sampling trajectories are echo-planar imaging (EPI) and Spiral (Figure 2.4). With EPI, multiple lines of the Cartesian grid are sampled at once by traversing the k-space back and forth. On the other hand, with spiral acquisitions, the k-space is sampled in a non-Cartesian spiral grid.

Selective Excitation

When an RF pulse is applied in the presence of only the B_0 field, spins from the entire volume get excited, as they all have the same precession frequency. In order to limit the excitation to a single slice or slab, selective excitation is used. The RF pulse is amplitude-modulated

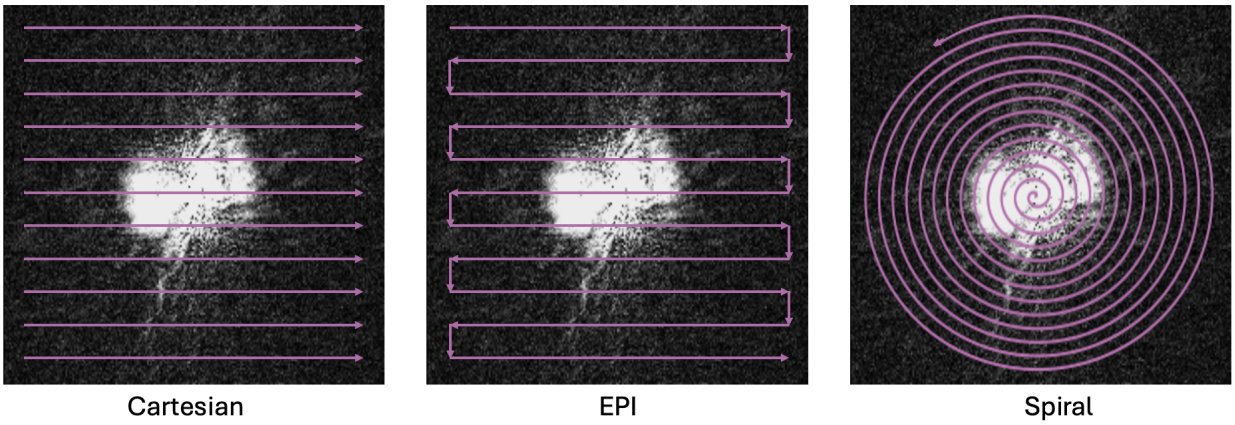

Figure 2.4: Common 2D sampling trajectories for k-space. In Cartesian acquisitions, k-space is sampled in a line-by-line fashion. With EPI, multiple k-space lines are sampled in a single acquisition by traversing k-space back and forth. Finally, with Cartesian sampling, k-space is sampled in a non-Cartesian spiral grid.

to have a specific frequency bandwidth. Generally, sinc-like RF pulses are used to have a rectangular frequency profile. When the gradient magnetic field is applied along a particular axis, the resonance frequency of the spins varies linearly with position. As a result, only the protons within a particular slice, where the local resonance frequency is within the RF pulse frequency bandwidth, are excited (Figure 2.5).

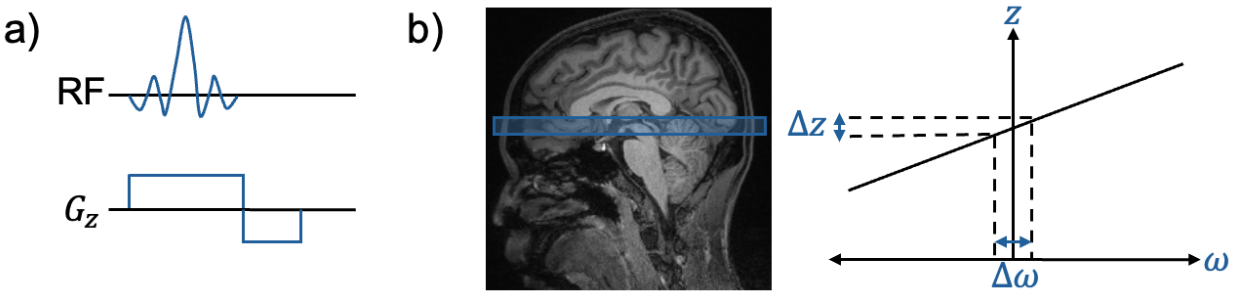

Figure 2.5: Slice-selective excitation to excite spins from a thin slice of tissue. a) An RF pulse with a specific frequency bandwidth is played out along with a gradient magnetic field. b) This pulse selectively excites spins that have resonant frequencies within a frequency bandwidth, corresponding to a slice.

2.3 Non-contrast Enhanced Methods to Image Flow and Perfusion

In addition to structural imaging, MRI can measure complex tissue dynamics, including perfusion, flow, and diffusion, offering essential information for diagnosis and providing insights into biophysical functions [1–3, 28]. Non-contrast enhanced methods are particularly advantageous as they minimize the risk for patients and improve patient comfort. Non-contrast enhanced tools to probe tissue dynamics include phase-contrast (PC) MRI [2, 6], arterial spin labeling (ASL) [7, 8] and diffusion MRI [29–31]. PC MRI encodes information about instantaneous velocity into the phase of spins to assess blood flow. ASL uses blood water as an endogenous tracer to measure tissue perfusion. Diffusion MRI measures the random motion of water molecules within tissue to provide information about tissue microstructure. Intravoxel incoherent motion (IVIM) [32] is another technique based on diffusion MRI, which models and quantifies both diffusion and perfusion within a single image voxel. Another technique is time-of-flight (TOF) MRI, which relies on inflow effects of unsaturated spins into a saturated imaging region to visualize vascular structure [33]. In this chapter, I will focus on two of these tools that are most relevant to the methods developed in this thesis, namely PC MRI and ASL.

Phase-Contrast (PC) MRI

Velocity Encoding

The data acquired by the MRI scanner is complex-valued, however, most MR images displayed are the magnitude of the reconstructed complex valued data. Nevertheless, the image phase can contain additional useful information on local magnetic field variations, tissue susceptibility as well as spin velocity. The phase term given by Equation (2.6) can be modified to include these additional, time-varying, effects as follows [34]

$$\phi(\vec{r},t) = \gamma B_0 t + \gamma \Delta B_0 t + \gamma \int_0^t \vec{r}(\tau)\cdot\vec{G}(\tau)d\tau \tag{2.9}$$

where ΔB_0 represents any variation in the static magnetic field and the spin positions $\vec{r}(t)$ are now assumed to be time-varying. The received signal can be demodulated to remove dependency on the B_0 field. Assuming a constant velocity, the gradient term can be simplified using a Taylor series expansion, resulting in the phase term being simplified to

$$\phi(\vec{r},t) = \phi_0 + \gamma\vec{r}_0\int_0^t \vec{G}(\tau)d\tau + \gamma\vec{v}\int_0^t \vec{G}(\tau)\tau d\tau. \tag{2.10}$$

Here, ϕ_0 denotes the background phase, and the subsequent two terms correspond to the zeroth (M_0) and first-order (M_1) gradient moments [34]. These describe the influence of gradient fields on the phase of static spins and spins moving at a constant velocity $\vec{v}$, respectively.

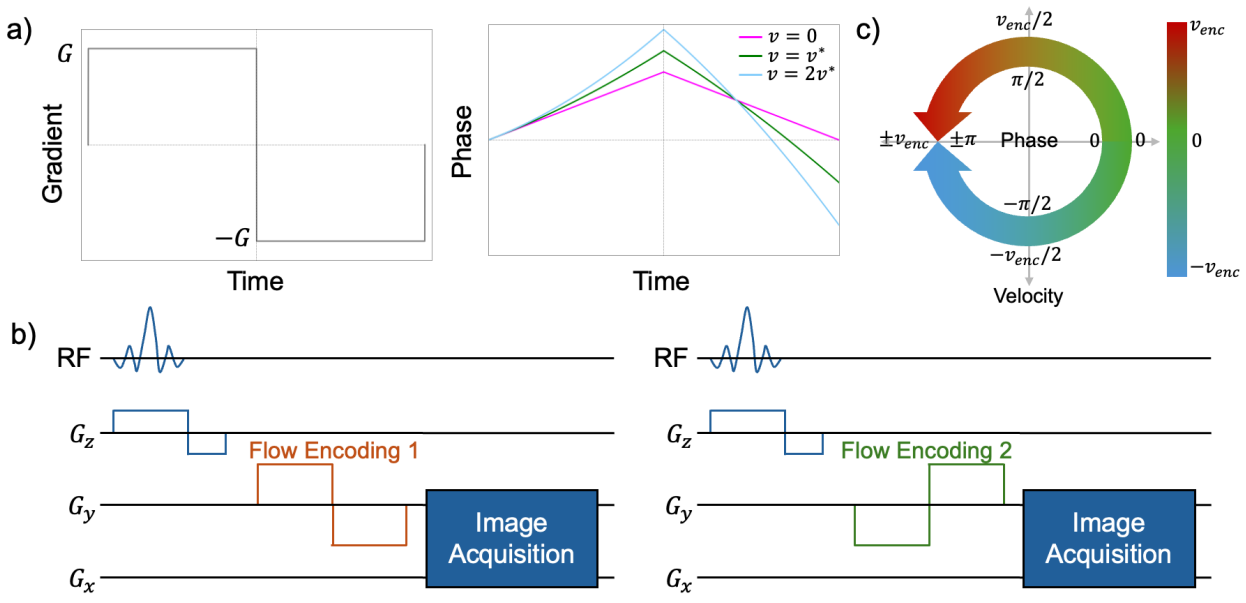

Figure 2.6: Details of PC acquisitions. a) Bipolar gradients and the phase accumulated when these gradients are played out for three spins with different velocities. The accumulated phase is zero for a static spin and increases with increasing velocity. b) In order to eliminate any effects due to background phase, two acquisitions are made with flipped flow encoding gradients. The measured phase from the two acquisitions is subtracted to isolate the phase change due to velocity. c) The maximum velocity that can be mapped is called the encoding velocity, v_{enc}, and the velocities between $\pm v_{enc}$ are mapped to the phase range between $\pm\pi$.

Bipolar gradients are used to perform velocity encoding as they have a zero zeroth-order moment and a non-zero first-order moment. Therefore, static spins will not accumulate any phase whereas moving spins will experience a phase change that is proportional to their velocity (Figure 2.6a). This phase change can be expressed as

$$\phi(v) = -\gamma M_1 v = \gamma G(T/2)^2 v \tag{2.11}$$

where G is the bipolar gradient amplitude in the direction of the velocity v and T is the bipolar gradient duration [34].

Nevertheless, the phase accumulation after the bipolar gradients will also have contributions from the background phase ϕ_0. In order to eliminate these effects, two acquisitions are made with flipped gradient directions (Figure 2.6b). These two acquisitions will have identical ϕ_0 whereas the phase change due to the first-moment will be opposite in direction. The phase difference between the two acquisitions only depends on the difference in first-moments (ΔM_1) and is proportional to the underlying velocity [34].

One important factor to consider is that the ranges of angles are limited. For example, if the measured angle reaches 2π it will wrap back around to 0. Therefore, only a certain

range of velocities can be mapped for a particular ΔM_1, without needing to perform phase unwrapping. The maximum velocity that can be mapped is called the encoding velocity v_{enc} and is defined in [34] as

$$v_{enc} = \frac{\pi}{\gamma \Delta M_1} \tag{2.12}$$

For a particular v_{enc} the velocities from $-v_{enc}$ to v_{enc} will be mapped to $-\pi$ to π (Figure 2.6c) [2]. The noise in the velocity measurements scales with the magnitude of v_{enc}, therefore, it is important to choose a v_{enc} that is as small as possible without causing any phase wrapping [2].

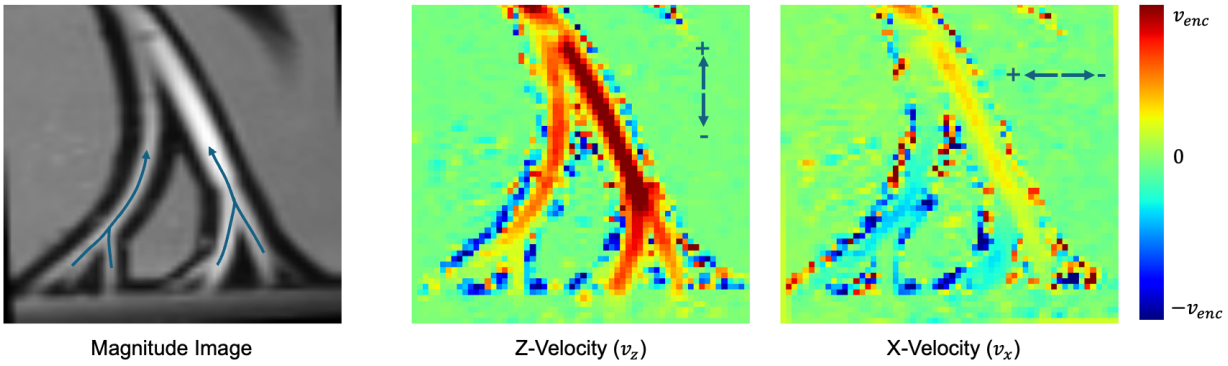

Figure 2.7: Magnitude and velocity images obtained from a 4D flow acquisition imaging water flowing through a set of tubes. A single coronal slice is displayed. **Left:** Magnitude image showing the direction of flow in the set of tubes. **Middle and Right:** The velocity images for the two in-plane directions, z and x.

4D Flow Imaging

When an acquisition is made with bipolar gradients along one axis, information about the velocity component along this particular axis gets encoded. It is possible to make three acquisitions with bipolar gradients along orthogonal directions along with a single reference acquisition to recover the three-directional velocity vector, $\vec{v}$. Figure 2.7, shows an example of how velocity can be measured along different directions for a flow phantom. The acquired image magnitude is shown, displaying the direction of flow in the tubes, as well as the velocity measurements along the z and x directions.

Traditionally, PC has been performed on a single 2D imaging slice. Development in PC techniques have allowed for a time-resolved 3D PC acquisition with three-directional velocity encoding. This acquisition is referred to as 4D Flow MRI [35]. By resolving velocities in a 3D volume, 4D Flow can be used to generate 3D particle trajectories for better visualization of

flow patterns. These trajectories can be displayed dynamically across different time points, for example, to better understand changes in blood flow over the cardiac cycle.

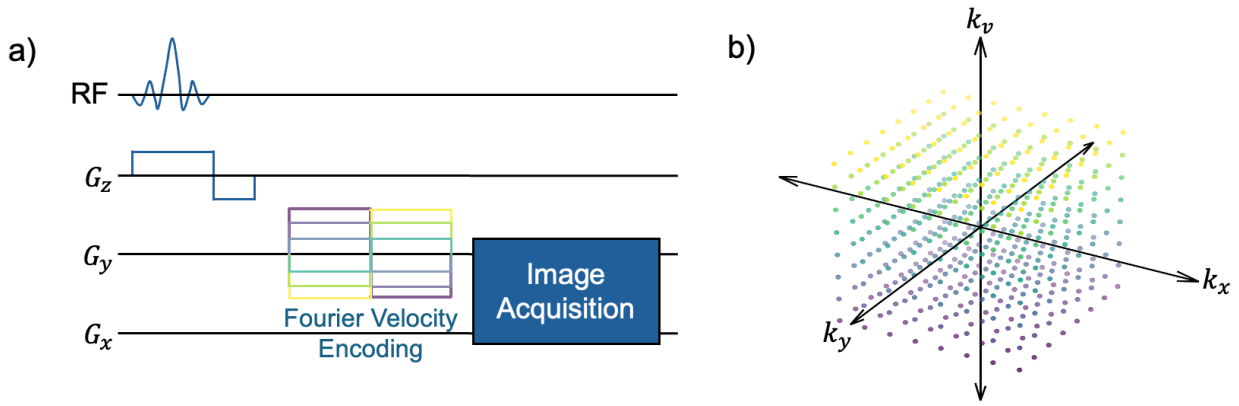

Figure 2.8: Acquisition scheme for FVE MRI with slice-selective 2D imaging. a) To perform a Fourier encoding of the bipolar gradients, multiple acquisitions are performed with incrementing velocity encoding. b) Each acquisition with a set of bipolar gradients will sample another point in the k_v space. Once enough points have been sampled, an inverse Fourier transform can be performed to obtain a velocity spectrum for each image voxel.

Fourier Velocity Encoded (FVE) MRI

One limitation of PC is that it is unable to resolve any partial volume effects when there is a distribution of different velocities within a single image voxel, for example, during complex flow patterns [36]. The measurement obtained through PC will be a complex average of all of the spins within the voxel, which may obscure essential flow dynamics. It is possible to increase the spatial resolution of the PC acquisition to reduce partial volume effects, however, this lowers SNR. Fourier Velocity Encoded (FVE) MRI performs a Fourier encoding of the bipolar gradients by making multiple acquisitions with incrementing velocity encoding (Figure 2.8a) [36, 37]. Each acquisition with different bipolar gradient amplitude will sample another point in the velocity k-space (k_v) as shown in Figure 2.8b. An inverse Fourier transform of the k_v space will give a velocity spectrum for each image voxel. Despite the increase in scan time due to the increased dimensionality of the dataset, FVE is useful in resolving complex flow patterns like flow jets due to stenosis [36].

Limitations

The limitations of PC MRI can be summarized as follows:

1. **Measurement Errors:** Eddy currents, concomitant gradients and gradient field distortions lead to errors in velocity measurements [26]. These effects depend on the gradient waveform applied, therefore, they do not cancel out after subtraction from a reference image.

2. **Limitations in Measuring Slower Flows:** In order to measure slower flows, smaller velocity encodings are required, which in turn necessitate larger bipolar gradients. Effects due to eddy currents and concomitant gradients are exacerbated for larger bipolar gradients [34]. In addition, larger bipolar gradients require increasingly longer echo times, which may worsen the signal quality. For this reason, PC MRI has limited success in studying slower flows and has been primarily employed to image flow in larger vessels with faster flows, i.e. the aorta.

3. **Encoding Velocity Dependency:** Due to the limitation in angles, only a specific range of velocities can be encoded. Setting a too low encoding velocity could result in aliasing for faster flows. On the other hand, setting a too high encoding velocity will increase the noise for slower flows. Therefore, it is difficult to select a single velocity encoding to image faster and slower flows in a single acquisition.

Arterial Spin Labeling (ASL)

Arterial spin labeling (ASL) magnetically labels blood water spins and uses the labeled spins as endogenous tracers to track tissue perfusion [7, 8]. In order to label spins, selective inversion pulses are used to invert the magnetization of arterial blood in the neck. Imaging is then performed downstream after a post-labeling delay once blood from the neck perfuses into tissue. ASL performs two acquisitions: one with labeling at the neck and another control acquisition. The control acquisition is subtracted from the labeled one to obtain a perfusion weighted image, which can be converted to a quantitative value of the cerebral blood flow (CBF) in units of ml of blood per $100g$ of tissue per minute [38].

One key parameter for ASL acquisitions is the post-labeling delay. This has to be set to ensure that there has been sufficient time for the blood to be transported into the tissue. However, the labeled arterial blood magnetization experiences T_1 decay throughout this time, which reduces the labeled signal. Therefore, the post-labeling delay has to be chosen carefully with consideration of the trade-off between the transit time and T_1 of arterial blood [38].

Another important factor is the labeling efficiency. This is a measure of how effectively the arterial blood is inverted at the neck, which needs to be taken into account when quantifying CBF. There are three types of ASL acquisitions that utilize different labeling strategies: continuous ASL (CASL), pseudocontinuous ASL (PCASL) and pulsed ASL (PASL), as summarized in Figure 2.9 [38, 39].

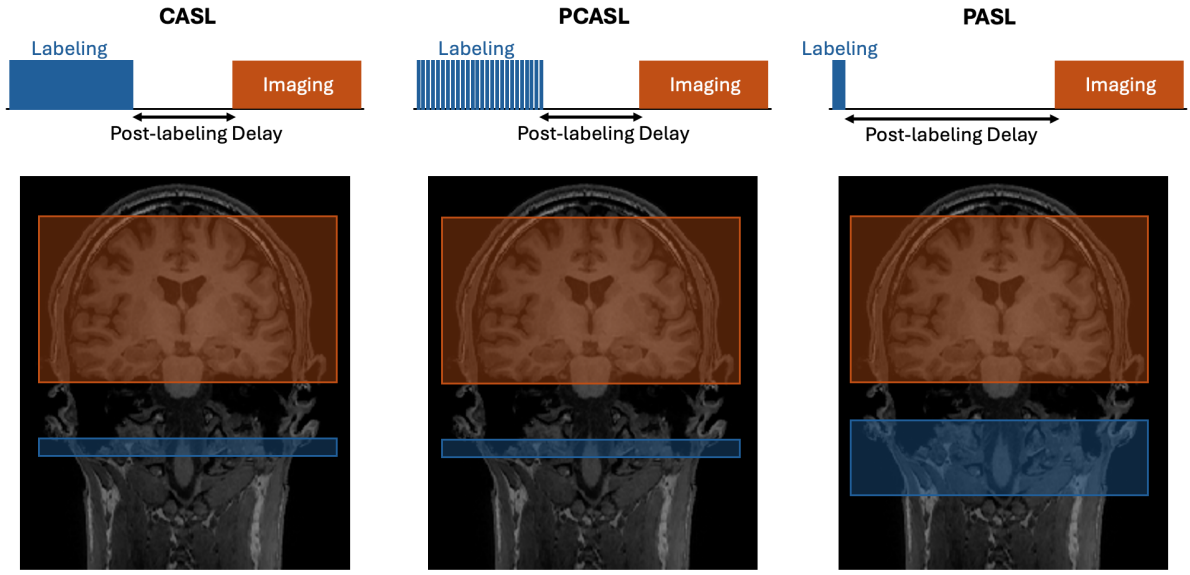

Figure 2.9: Summary of different labeling strategies. **Left:** CASL uses a long, continuous labeling pulse followed by an image acquisition covering the entire brain. **Middle:** PCASL uses a train of shorter RF and gradient pulses instead of a long continuous pulse. **Right:** PASL inverts magnetization in a large slab with a shorter labeling duration.

Labeling Strategies

CASL: In CASL [40, 41], a long RF pulse is applied along with a gradient in the z direction, for a duration of 2-4s, to invert blood flowing in the arteries. The image acquisition covers a large FOV of the entire brain. This acquisition has high labelling efficiency, however, it also requires very high energy deposition into the tissue due to the long RF pulse duration [38].

PCASL: To overcome the limitations of CASL, PCASL uses a train of shorter RF and gradient pulses instead of a long continuous pulse [42, 43]. PCASL has the same labeling efficiency as CASL, with lower energy deposition. One limitation of PCASL is that it is sensitive to off-resonance effects during labeling, which may lead to reduction in the labeling efficiency [38].

PASL: Unlike CASL and PCASL, which invert blood spins at a thin slice located at the neck, PASL inverts magnetization in a large slab with a significantly shorter labeling duration [44]. This technique results in lower energy deposition and shorter scan times due to its shorter labeling duration. However, its primary limitation is a lower SNR caused by the smaller labeling bolus.

Owing to its high labeling efficiency and lower energy deposition, PCASL is the recommended labeling strategy for most ASL acquisitions.

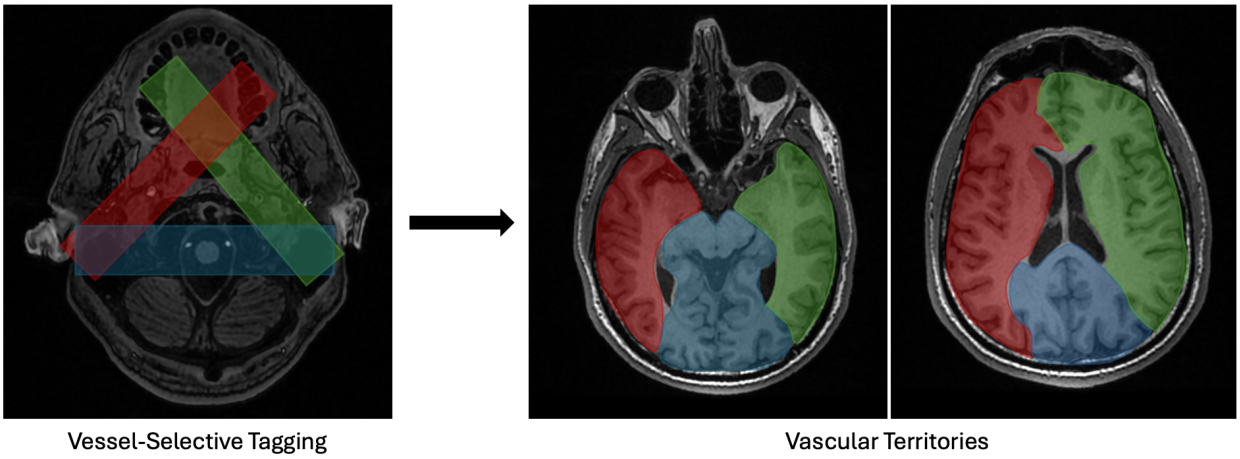

Figure 2.10: Vessel-selective ASL. Feeding arteries are selected individually at the neck and the vascular territories can be mapped using ASL.

Vessel-Selective and Vessel-Encoded ASL

In order to image different vascular territories, specific arteries or groups of arteries can be selectively tagged at the neck, isolating the CBF contribution from individual feeding arteries. With the vessel-selective ASL approach [45–48], individual arteries are selectively labelled, one vessel at a time, and their vascular perfusion territories can be determined (Figure 2.10). In contrast, with the vessel-encoded ASL spatially varying gradients are applied during tagging to tag combinations of arteries in encoding schemes, for example with a Hadamard encoding scheme [8]. This can provide a more efficient method to map vascular territories of individual feeding arteries.

Limitations

The limitations of ASL can be summarized as follows:

1. **Labeling Efficiency:** The labeling efficiency in ASL can be dependent on several factors including arterial flow velocity and the position of the labeling plane, which can in turn lead to inaccuracies in CBF quantification [38].

2. **Arterial Transit Time Variability:** ASL is also sensitive to the arterial transit time that can show variability across brain regions and individuals, especially during disease [38].

3. **Susceptibility to Imperfections:** ASL is susceptible to magnetic field inhomogeneities and flow artifacts [38].

4. **Geometry Limitations:** ASL is constrained to configurations where a single labeling plane can be selected, reducing its versatility.

Chapter 3

Displacement Spectrum Imaging

3.1 Introduction

Non-contrast and non-invasive MRI methods to study flow and perfusion in-vivo allow for wider accessibility in the patient population as well as an improved patient experience. These methods have been successfully applied across a range of applications, however, for many pathologies, contrast-enhanced acquisitions remain to be the clinical standard for diagnosis. This is mainly due to the limitations of the current non-contrast techniques. One such limitation is the dependence on patient-specific physiological factors, which can affect the accuracy and reliability of quantification [49]. Furthermore, these non-contrast methods have limited versatility and are not always easily adaptable to different anatomies as well as to hemodynamics involving different blood flow velocities [34].

In this chapter, I will describe a new non-contrast enhanced tool called Displacement Spectrum (DiSpect) Imaging [1] [50], which is a highly versatile technique based on Displacement Encoding with Stimulated Echoes (DENSE) [51, 52]. DiSpect acquires a rich dataset, which can be used to image various complex tissue dynamics including blood flow and tissue perfusion over various different time scales. First, I will present the theory behind DENSE and DiSpect acquisitions. Next, I will describe the multi-dimensional dataset acquired by DiSpect and provide details on how we process this dataset. I will talk about different sequence adjustments and modifications that can be performed to tailor the acquisition for specific applications. Finally, I will present a validation of the technique with flow-phantom and in-vivo experiments.

[1] The content of this chapter is derived from previously published co-authored material in [50].

3.2 Displacement Encoding with Stimulated Echoes (DENSE)

Velocity vs. Displacement Imaging

Unlike phase-contrast (PC), which performs velocity imaging, DENSE measures displacement. Before moving into details of the DENSE acquisition, I will demonstrate the difference between velocity and displacement imaging on a schematic of a tree of vessels as shown in Figure 3.1. A velocity measurement in PC MRI determines what direction spins are travelling to, at the particular time of imaging. On the other hand, to measure displacement, spins are initially tagged. After a particular time, imaging is performed and the positions from which spins are displaced from can be traced.

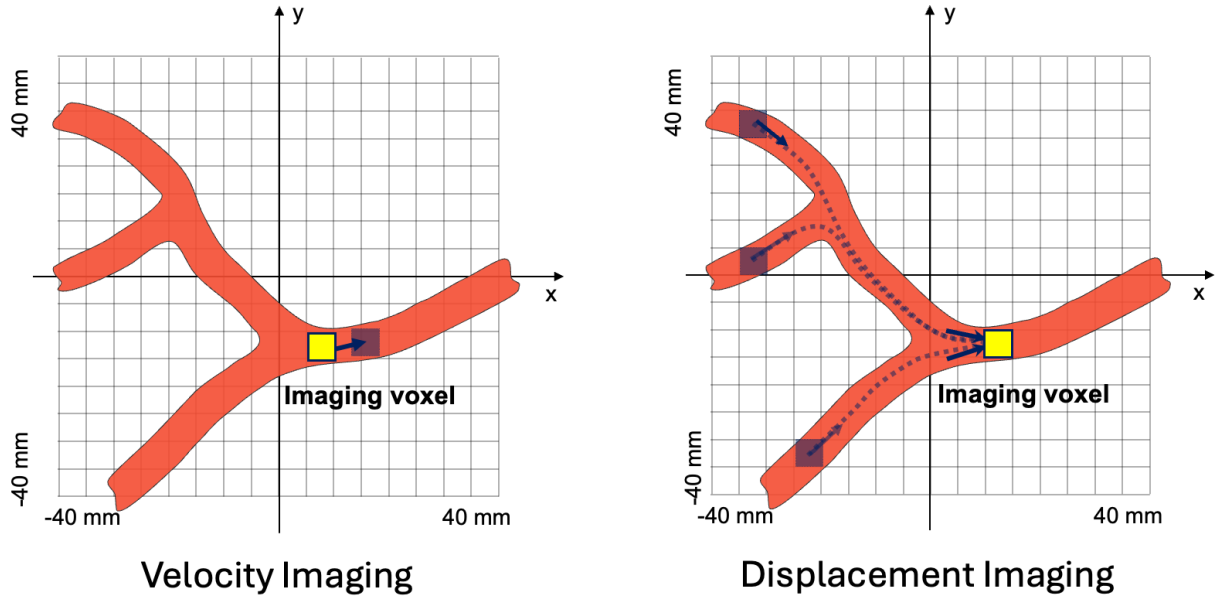

Figure 3.1: The difference between velocity and displacement imaging. **Left:** In velocity imaging, the measurement corresponds to the direction in which spins are travelling to at the particular time of imaging. **Right:** With displacement imaging, spins are initially tagged. After a delay period, imaging is performed and the locations from which spins displaced from into the imaging voxel can be traced.

Mathematically, the displacement measurement corresponds to the integration of instantaneous velocities:

$$D = \int_0^T v(t)dt \tag{3.1}$$

where D is the displacement, $v(t)$ are the time-dependent velocities and T is the time interval between tagging and imaging.

Pulse Sequence

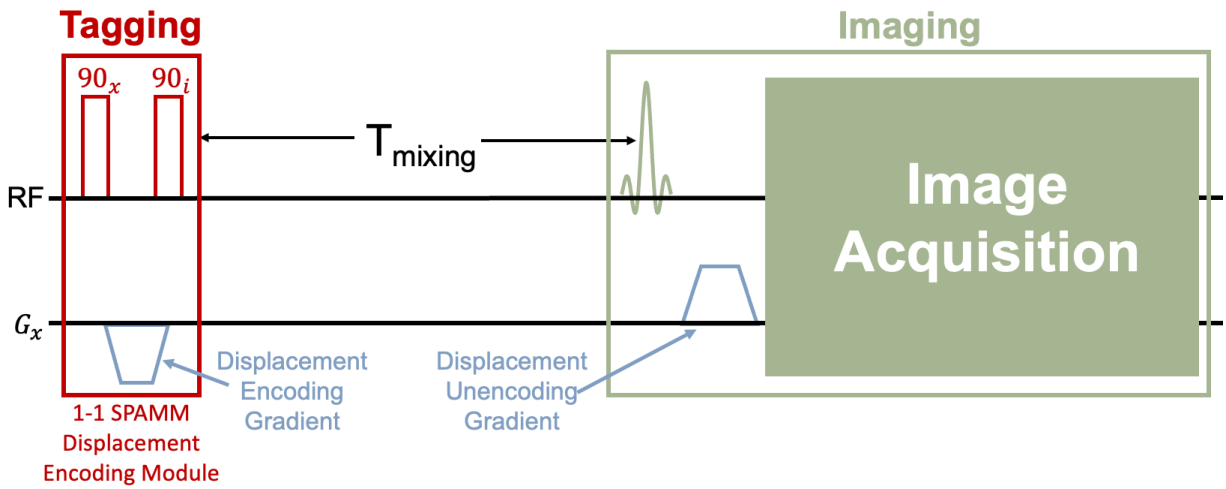

Figure 3.2: Pulse sequence diagram for DENSE. A 1-1 SPAMM tagging module is applied to cosine modulate the longitudinal magnetization according to the initial position of spins. After a particular mixing time, T_{mixing}, an image is acquired. The image phase is proportional to the displacement that has occurred during the mixing time.

The DENSE pulse sequence is shown in Figure 3.2. The acquisition begins with a 1-1 spatial modulation of magnetization (SPAMM) tagging module, which cosine modulates the longitudinal magnetization according to the initial position of spins [53]. The longitudinal magnetization at the end of the tagging pulse will be

$$M_z(\vec{r}) = M_0(\vec{r}) \cos(\vec{k}_d \cdot \vec{r}). \tag{3.2}$$

Here, $M_0(\vec{r})$ corresponds to the equilibrium longitudinal magnetization at position $\vec{r}$ right before the tagging pulse, $\vec{k}_d$ is the displacement encoding frequency proportional to the area of the displacement encoding gradient and $\vec{r}$ is the initial position of the spins. In Figure 3.2, the displacement encoding gradient is performed in the x direction, however, in general, the gradient can be applied in any direction.

Imaging is performed after a mixing time, T_{mixing}. During this mixing time, the longitudinal magnetization experiences T_1 relaxation. The magnetization right before the image acquisition is given by

$$M_z(\vec{r}, T_{mixing}) = M_0(\vec{r})\cos(\vec{k}_d \cdot \vec{r})e^{-T_{mixing}/T_1} + M_0(\vec{r})(1 - e^{-T_{mixing}/T_1}). \tag{3.3}$$

Assuming that imaging is performed with a flip angle of 90^o, the transverse magnetization $M_{xy}(\vec{r})$ after RF excitation will be equal to $M_z(\vec{r}, T_{mixing})$. By expanding the cosine into a sum of exponentials we obtain

$$M_{xy}(\vec{r}) = \frac{M_0(\vec{r})}{2}e^{-T_{mixing}/T_1}e^{j\vec{k}_d\cdot\vec{r}} + \frac{M_0(\vec{r})}{2}e^{-T_{mixing}/T_1}e^{-j\vec{k}_d\cdot\vec{r}} + M_0(\vec{r})(1 - e^{-T_{mixing}/T_1}). \tag{3.4}$$

Next, an unencoding gradient pulse is applied with the same gradient area as the encoding pulse but in the opposite direction. We can assume that the spins have displaced by an amount $\Delta\vec{r}$ during the mixing time and are now at positions $\vec{r} + \Delta\vec{r}$. Therefore, the unencoding gradient pulse will apply a phase $e^{-j\vec{k}_d(\vec{r}+\Delta\vec{r})}$ to the transverse magnetization. The new transverse magnetization after the unencoding gradient can be written as

$$\begin{aligned} M_{xy}(\vec{r}) = {} & \frac{M_0(\vec{r})}{2}e^{-T_{mixing}/T_1}e^{-j\vec{k}_d\cdot\Delta\vec{r}} + \frac{M_0(\vec{r})}{2}e^{-T_{mixing}/T_1}e^{-j\vec{k}_d\cdot\Delta\vec{r}}e^{-j2\vec{k}_d\cdot\vec{r}} \\ & + M_0(\vec{r})(1 - e^{-T_{mixing}/T_1})e^{-j\vec{k}_d\cdot(\vec{r}+\Delta\vec{r})}. \end{aligned} \tag{3.5}$$

Equation (3.5) is the sum of three terms, called echoes [54], which can be described as:

1. **Displacement-encoded Echo** with a phase of $e^{-j\vec{k}_d\cdot\Delta\vec{r}}$, which is proportional to the displacement.
2. **Conjugate displacement-encoded Echo** with a phase of $e^{-j\vec{k}_d\cdot\Delta\vec{r}}e^{-j2\vec{k}_d\cdot\vec{r}}$.
3. **T1 Echo**, which occurs due to the T_1 recovery during the mixing time, $M_0(\vec{r})(1 - e^{-T_{mixing}/T_1})$, with a phase $e^{-j\vec{k}_d\cdot(\vec{r}+\Delta\vec{r})}$ due to the unencoding gradient.

These three echoes can be visualized in Figure 3.3a. Isolating the displacement-encoded echo will yield an image, which has a phase that is proportional to the displacement that occurred during the mixing time, i.e. $\vec{k}_d \cdot \Delta\vec{r}$.

Echo Separation

In order to isolate the displacement encoded echo, phase-cycling is performed by varying the phase of the second RF pulse applied during the SPAMM module [54]. For 3-point phase-cycling, the phase is varied in 120^o increments and three acquisitions are made. For each of

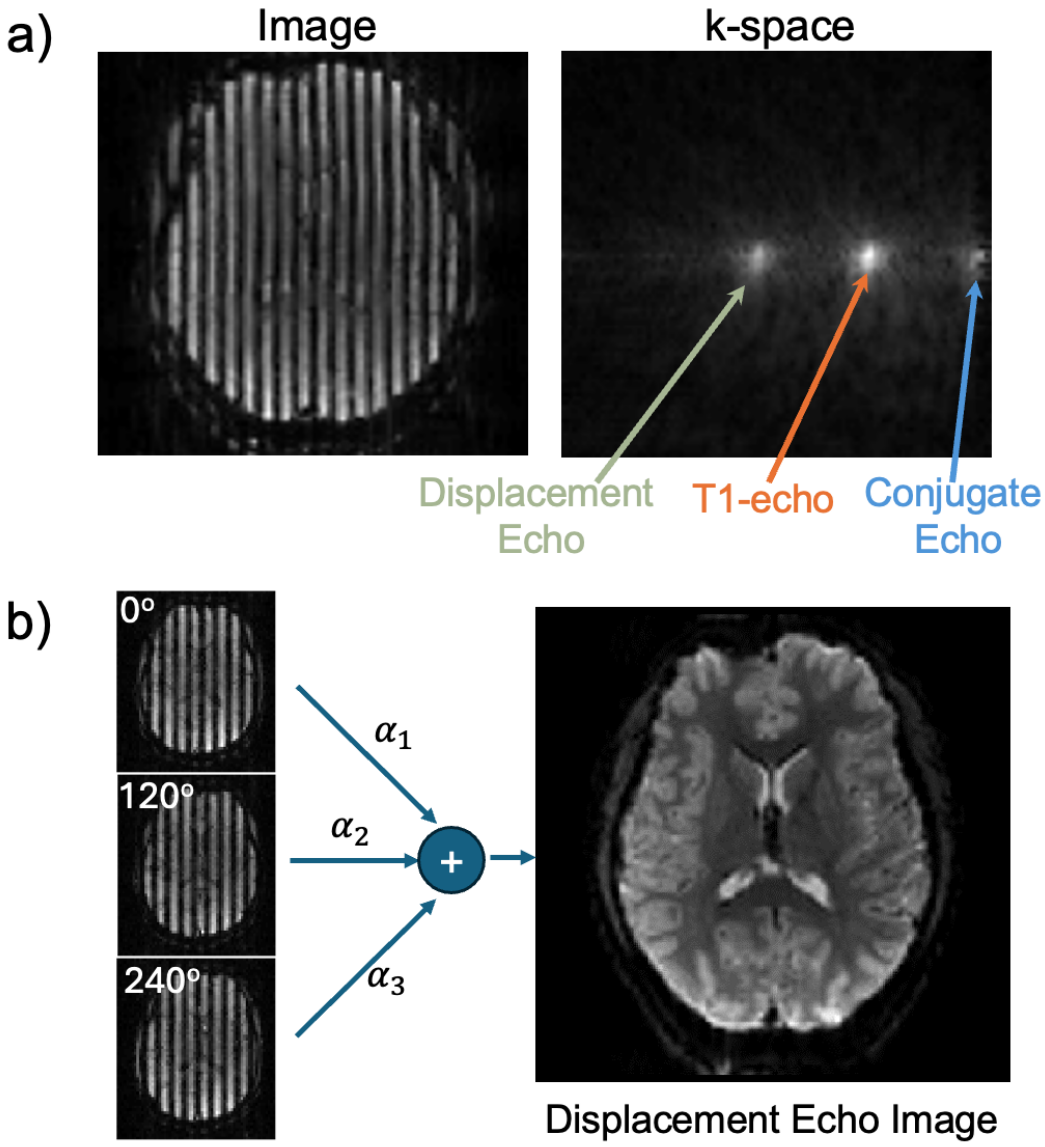

Figure 3.3: DENSE echo separation. a) An image acquired with DENSE will have stripes due to the cosine modulation during tagging. If we look at the k-space of this image, we observe three echoes. The displacement echo and the conjugate echo are a result of the cosine modulation during tagging. The T_1 echo is due to the T_1 relaxation that occurs during the mixing time. The displacement echo contains the displacement information in its phase and therefore we would like to isolate it. b) In order to isolate the displacement echo, three acquisitions are made by varying the phase of the second RF pulse in the SPAMM module. These three acquisitions are linearly combined to isolate the displacement echo.

these acquisitions, the three echoes will be combined with different coefficients. The forward model of the phase-cycling operation, for acquisitions made with phases of $0^o, 120^o, 240^o$, can be expressed as

$$\begin{bmatrix} 1 & 1 & 1 \\ e^{-2\pi/3} & e^{2\pi/3} & 1 \\ e^{2\pi/3} & e^{-2\pi/3} & 1 \end{bmatrix} \begin{bmatrix} s_{conj} \\ s_{disp} \\ s_{T_1} \end{bmatrix} = \begin{bmatrix} s_{0^o} \\ s_{120^o} \\ s_{240^o} \end{bmatrix}. \tag{3.6}$$

Here, s_{conj}, s_{disp} and s_{T_1} correspond to the three echoes, while s_{0^o}, s_{120^o} and s_{240^o} correspond to the three acquisitions made with different phase cyclings. Equation 3.6 is of the form $A\vec{x} = \vec{y}$, where A is an invertible matrix. The three echoes can be obtained as $\vec{x} = A^{-1}\vec{y}$. The displacement echo image is thus a linear combination of the three acquisitions (Figure 3.3b).

Applications and Limitations

In DENSE acquisitions, the displacement encoding gradient amplitude and direction as well as the mixing time can be set to measure displacement across different time scales. However, similar to phase-contrast, this technique only captures a single displacement value per voxel, which is an average of all of the displacing spins in that voxel. Therefore, it can not resolve any partial volume effects when there is a distribution of displacements within a single voxel. DENSE is mainly used to study bulk displacement, for example, to measure cardiac myocardial strain [51, 52, 55].

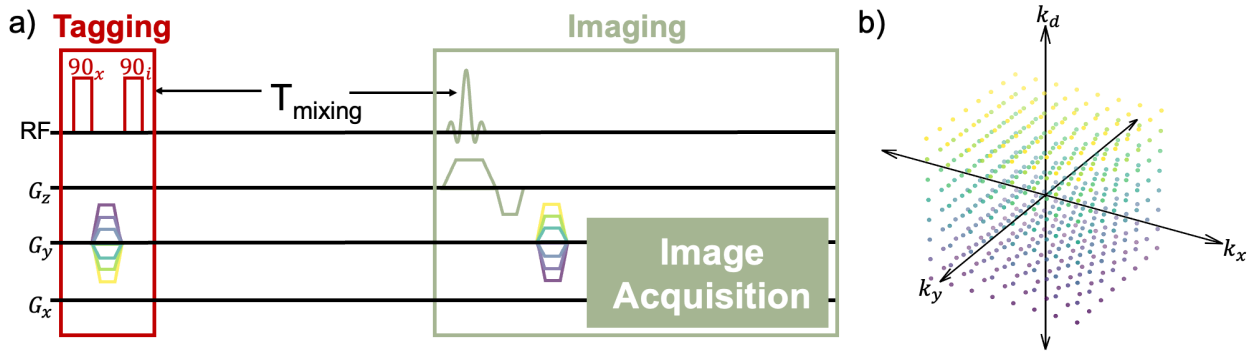

Figure 3.4: DiSpect pulse sequence. a) The pulse sequence is very similar to DENSE, however, instead of making a single acquisition with a single set of displacement encoding gradients, multiple acquisitions with increasing displacement encoding gradients are performed. b) Each acquisition with a different set of displacement encoding gradients samples a new point in the displacement k-space k_d.

3.3 Displacement Spectrum (DiSpect) Imaging

Displacement Spectrum (DiSpect) Imaging is a Fourier encoding variant of DENSE, which can be used to image flow and tissue perfusion over short (few milliseconds) to long (few seconds) time scales. DiSpect performs multiple acquisitions with increasing DENSE encoding to resolve a spectrum of displaced spins for each image voxel. This spectrum is called the displacement spectrum and can be up to three dimensional. The pulse sequence of DiSpect is shown in Figure 3.4a. In a way, DiSpect is the displacement equivalent to Fourier velocity encoded MRI, while DENSE is the displacement equivalent to PC MRI. Instead of performing multiple acquisitions to sample the velocity k-space, k_v, DiSpect samples the displacement k-space, k_d (Figure 3.4b).

Similar to DENSE, the displacement information is captured in the phase of the signal. However, because a displacement spectrum is acquired for each image voxel, more complex tissue dynamics can be resolved. Since the displacement information is encoded into the longitudinal magnetization, DiSpect acquisitions can be made with long mixing times, only limited by T_1 relaxation. DiSpect can be performed with different image acquisition strategies, for example, EPI, Spiral or Cartesian readouts.

Acquisition

The DiSpect data acquisition process is summarized in Figure 3.5. In general, if Fourier encodings of the displacement encoding gradients are performed on all three axes, a 3D displacement spectrum will be measured for every image voxel. In this example, we are acquiring a 2D displacement spectrum for each image voxel, by varying the displacement encoding gradients on only the x and y axes.

For each set of displacement encoding gradients three acquisitions are performed for echo separation. With each phase cycling the bands in the image are shifted as a result of differences in RF pulse phase. The isolated displacement echo corresponds to one point in the 2D displacement k-space.

Additional acquisitions can be performed with increasing displacement encoding gradients to fill new points in the displacement k-space. The frequency of the cosine modulation increases with increasing displacement encoding gradients (Figure 3.5). Due to the need to perform multiple acquisitions with different displacement encodings, the DiSpect acquisition is time consuming. To fully sample a 2D displacement k-space with $M \times N$ points, a total of $M \times N \times 3$ acquisitions need to be made.

Once the displacement k-space is fully sampled, an inverse Fourier transform is performed to obtain the displacement spectra for each image voxel. In DiSpect, voxels in the imaging plane are referred to as **target** locations, whereas locations in the displacement spectra of each target voxel are referred to as the **sources**. It is important to note that encodings in the target and source dimensions are independent. The target FOV and the target resolution depend on the parameters of the image acquisition. On the other hand, the source FOV and

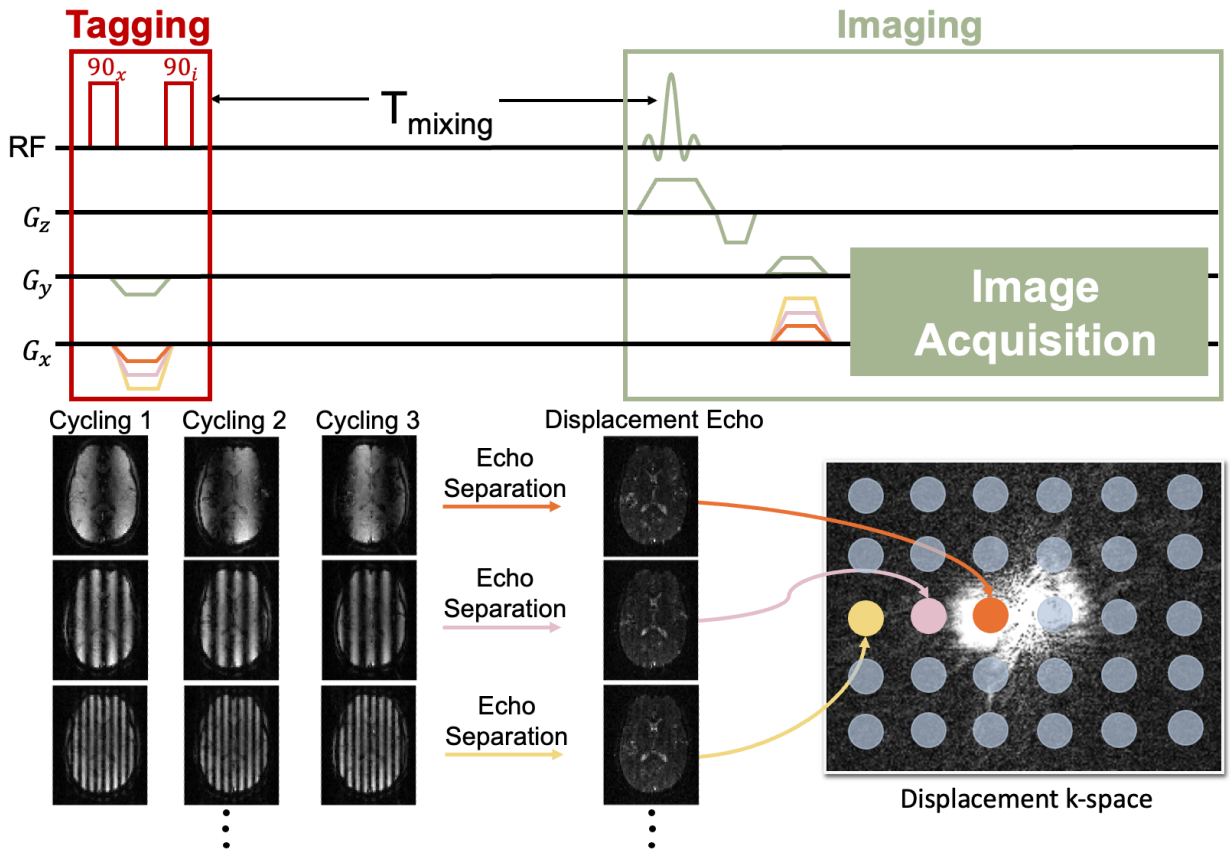

Figure 3.5: Summary of the DiSpect acquisition process. In this example, 2D displacement spectra are acquired by varying the displacement encoding gradients on two axes. For each set of displacement encoding gradients, three phase cyclings are performed to isolate the displacement echo. This isolated displacement echo corresponds to one point in the 2D displacement k-space. The gradients can be incremented to make more acquisitions and fill the 2D displacement k-space.

the source resolution are determined by the usual Nyquist criteria on the step size, Δk_d and maximum extent, k_{dmax}, of the sampled displacement frequencies.

The displacement spectrum of each target voxel represents sources in relative coordinates to the position of that voxel. In order to represent the sources in absolute coordinates, they need to be translated by the coordinate of the target image voxel.

Displacement Spectra for Different Tissue Dynamics

Different tissue dynamics will have different displacement spectra characteristics. The expected 1D displacement spectra are displayed, along the left-right (LR) and anterior-posterior

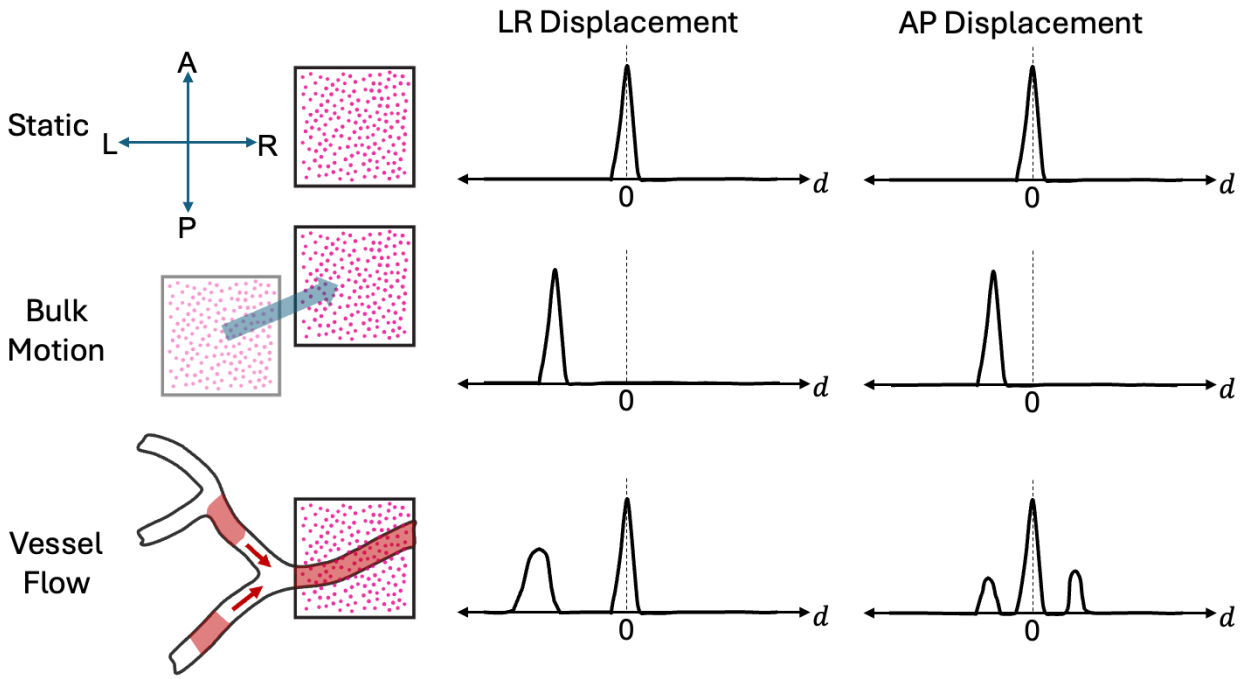

Figure 3.6: Displacement spectra characteristics for different tissue dynamics. For static tissue, it is expected that the displacement spectra will be symmetric and centered at 0. If there is bulk motion, the displacement spectrum will be shifted according to the direction and strength of the motion. In the case of vessel flow, there will be multiple peaks observed in the displacement spectra. The large center peak corresponds to the static tissue in the voxel. The smaller peaks correspond to the blood arriving to the voxel from different branches of the vessel.

(AP) dimensions, for three different tissue dynamics in Figure 3.6. For static tissue, it is expected that the displacement spectra will be symmetric and centered at 0. If there is bulk motion, the displacement spectrum will be shifted according to the direction and strength of the motion. Since there are no partial volume effects in this case, only two displacement encodings are sufficient to estimate displacement by measuring the phase accumulation between the two encodes. This is how the DENSE technique measures myocardial displacement maps to assess cardiac function.

In the case of a vessel flowing into the target image voxel there will be multiple peaks observed in the displacement spectra. The large center peak corresponds to the static tissue in the voxel. The smaller peaks correspond to the blood arriving to the voxel from different branches of the vessel. 1D displacement spectra may not always be sufficient to resolve the blood sources coming from different vessel branches, in which case higher dimensional displacement encoding might be necessary.

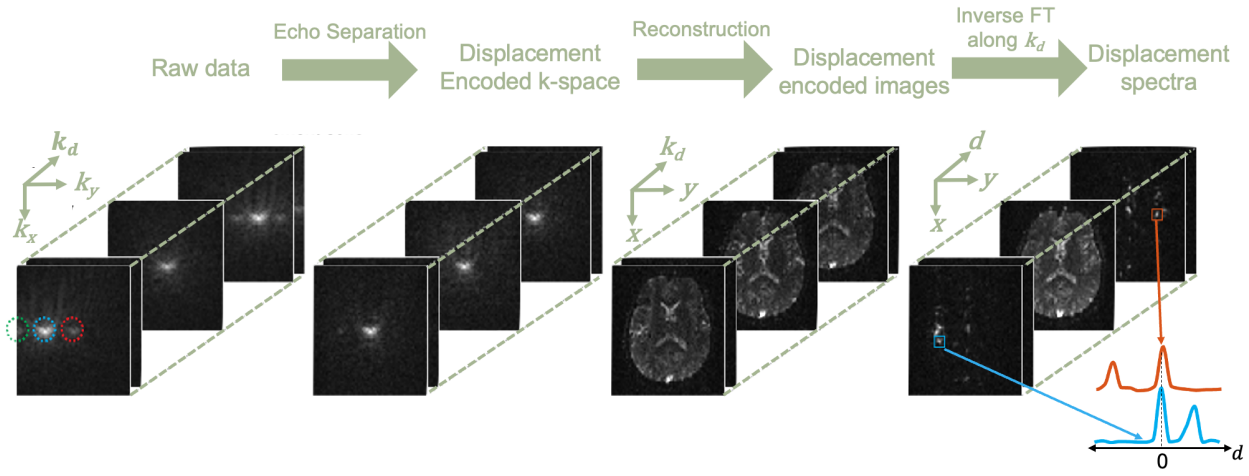

Figure 3.7: DiSpect reconstruction pipeline. For ease of visualization, the reconstruction pipeline is displayed for 1D displacement encoding. The raw data contains three echoes in k-space. Echo separation is performed to obtain the displacement encoded image k-space. Then, regular image reconstruction can be performed to obtain displacement encoded images. Finally, an inverse Fourier transform(s) performed in the displacement encoding dimension(s) results in displacement spectra for each target image voxel. 1D displacement spectra are shown for two example target voxels.

Reconstruction

DiSpect has a straightforward reconstruction pipeline (Figure 3.7). The raw data that is collected from the scanner contains three echoes in k-space. Echo separation is performed to obtain the displacement encoded image k-space. Then, regular image reconstruction can be performed to obtain displacement encoded images. Finally, an inverse Fourier transform(s) performed in the displacement encoding dimension(s) results in displacement spectra for each target image voxel. It is important to note that, since echo separation is just a linear combination of the phase cycled acquisitions, it is also possible to perform this after reconstructing the displacement encoded images.

Pulse Sequence Modifications

Several modifications can be made to the DiSpect pulse sequence in order to tailor it to different applications.

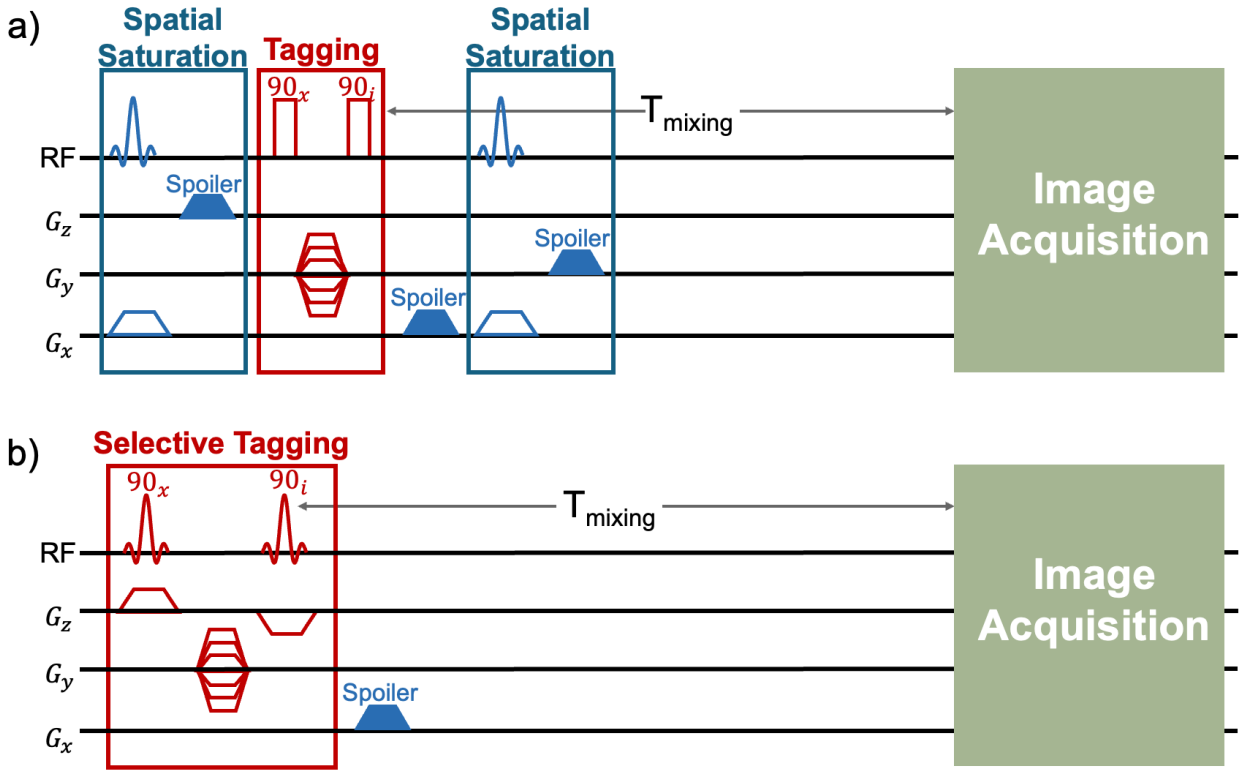

Figure 3.8: Spatial saturation and selective excitation. a) Spatial saturation bands are applied before and after tagging. The directions of spoiler gradients used for each spatial saturation block are different to avoid any additional stimulated echoes from forming. b) For selective excitation, the non-selective hard RF pulses used during tagging are replaced with selective RF pulses.

Saturation Bands

Spatial saturation bands can be used to suppress signal from certain regions of the displacement spectrum. For example, saturation bands could be used to suppress signal from static tissue, which could otherwise lead to undesired physiological noise. Saturation bands can also be used to eliminate signal from certain regions where spins displace into the imaging slice. By reducing the regions where blood can displace into the imaging slice, a smaller displacement FOV can be prescribed, without resulting in aliasing.

To achieve better saturation, spatial saturation bands are placed before and after the SPAMM tagging module (Figure 3.8a). Different spoiler gradient amplitudes and directions are used for each saturation pulse to avoid any additional stimulated echoes from forming. Multiple saturation bands can also be applied consecutively to suppress signals from multiple regions.

Selective Tagging

Instead of limiting the displacement FOV by suppressing certain regions, it is also possible to selectively tag the magnetization of spins within a particular region, for example, a slab. Selective tagging can also reduce scan time by reducing the number of points that need to be sampled in the displacement k-space.

Selective tagging can be achieved by replacing the non-selective hard RF pulses applied during tagging with selective pulses (Sinc RF, Shinnar–Le Roux (SLR) pulses). It is important to note that the gradient amplitude must be reversed for the first and second tagging pulses to ensure that phase accumulation originates solely from the displacement encoding gradient (Figure 3.8b). It is also possible to use selective excitation in combination with spatial saturation, for example, to limit the displacement FOV simultaneously while also saturating signal from static tissue.

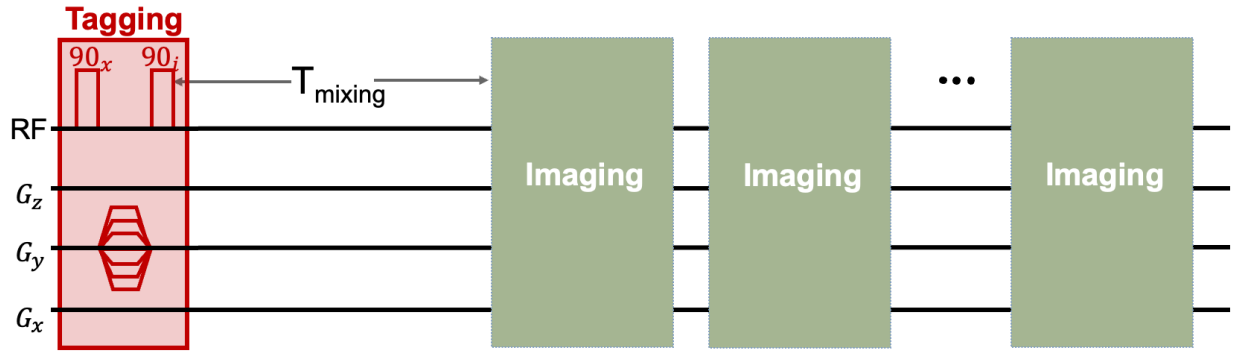

Figure 3.9: Repeated image acquisitions after tagging can be used to obtain the temporal dynamics of flow and perfusion.

Repeated Image Acquisitions

In order to obtain the temporal dynamics of blood flow, imaging can be performed repeatedly after tagging (Figure 3.9). With repeated imaging, the displacement spectra are sampled at multiple mixing times. The temporal resolution is only limited by the duration of each image acquisition. However, when selecting a temporal resolution, it is also important to consider the flow velocity at target image locations. For example, if a too high temporal resolution is used while imaging slower flows or tissue perfusion, the repeated image acquisitions could saturate the magnetization within the imaging slice. This could result in little or no signal from the area of interest. Therefore, the flow velocity should be taken into consideration when choosing the temporal resolution.

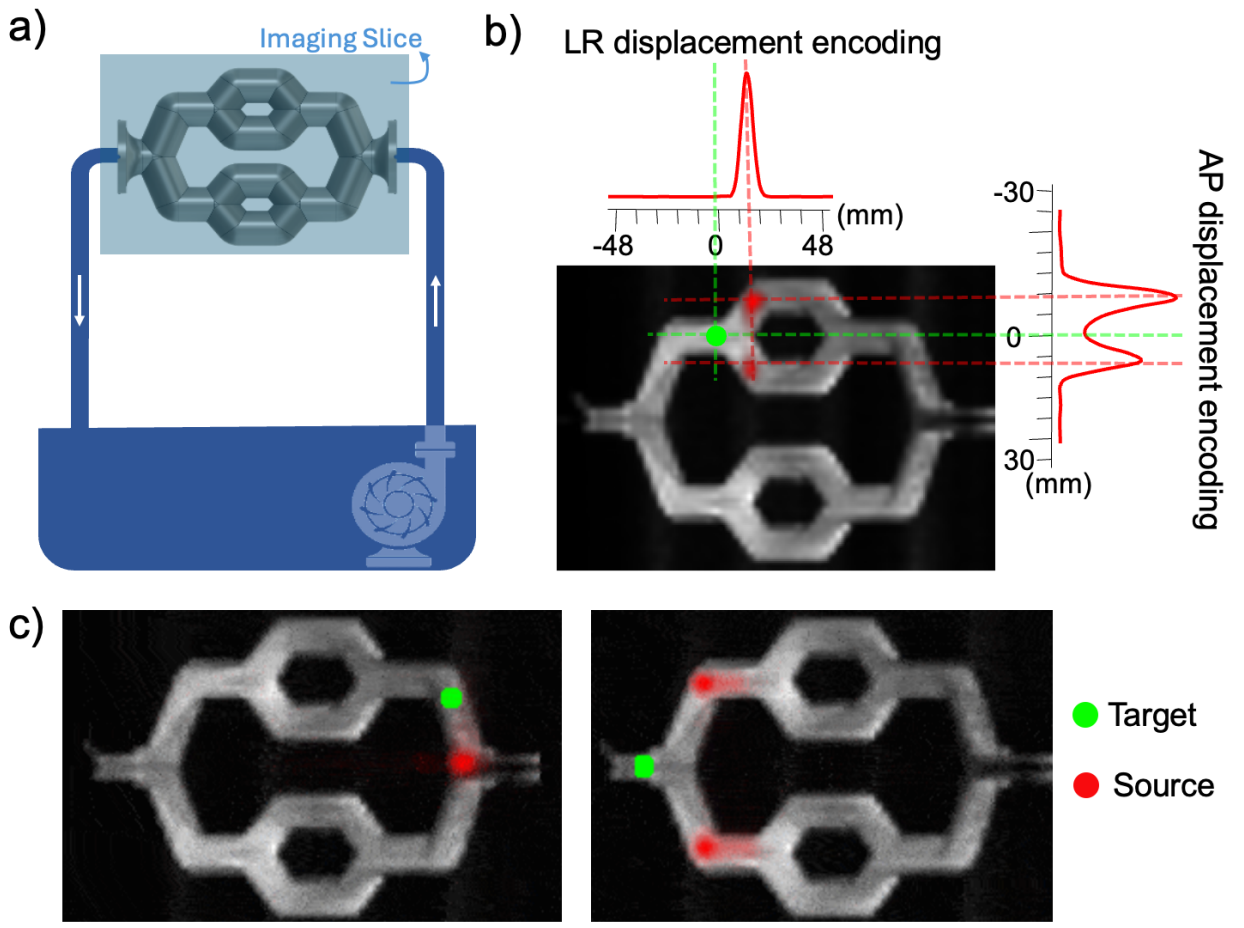

Figure 3.10: Demonstrating the ability of DiSpect to trace the sources of water flowing through a planar set of tubes. a) Experimental setup showing the 3D printed set of tubes connected to a continuous flow pump. b) The axial imaging slice with a target location marked in green. The acquired displacement spectra in the LR and AP directions for the target region are combined to determine the sources of water entering this region. c) Two more target regions are selected and their sources are determined in a similar fashion.

3.4 Methods

Simple Planar Flow Phantom Study

We performed a simple flow phantom study in order to demonstrate that DiSpect can trace water flow even in the presence of partial volume effects, when a single image voxel contains spins displacing from multiple different regions. A set of tubes that splits and merges flows was designed and 3D-printed (Figure 3.10a). The tube structure was designed to be planar

to limit the displacement into two dimensions. The tubes were connected at both ends to an external continuous flow pump, which was used to pump water through the tubes. The experiment was performed on a Siemens Trio 3T (Erlangen, Germany) scanner.

Two DiSpect acquisitions with a 2D gradient-echo (GRE) readout were performed to image the phantom. For both acquisitions an axial imaging slice was placed as shown in Figure 3.10a. For the first scan, a 1D displacement spectrum was acquired in the LR direction, and in the second a 1D displacement spectrum was acquired in the AP direction. The 1D displacement spectra are projected along the other axes. Both scans were acquired with a target image resolution of $3 \times 3\text{mm}^2$, a target image FOV of $19.2 \times 12\text{cm}^2$, a repetition time (TR) of $500ms$ and a single mixing time of $400ms$. The source resolution was 3mm with a FOV of 150mm along the LR direction, and 90mm along the AP direction. The total scan time was 66.7 minutes for LR encoding and 40 minutes for AP encoding. Between tagging and imaging, the water spins in the phantom flow and displace. The DiSpect acquisitions can trace the sources of the water spins within the tubes.

Unlike PC MRI, which provides information on the direction spins are going to, at the time of imaging, DiSpect provides information on where spins came from into the target image voxel. Assuming that the velocity of the spins do not change across a short mixing time, it is possible to estimate a velocity-like measurement from the displacement spectra. To accomplish this, we can define three color filter functions (Figure 3.11a), which equally span the displacement FOV, to give weights to red, green and blue colors based on the amount of displacement. These color filters are then applied to the displacement spectra of all image voxels.

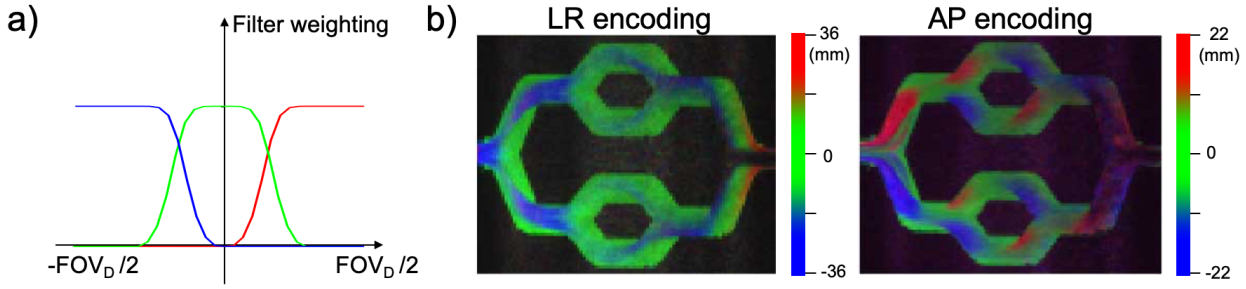

Figure 3.11: Generating color-coded displacement maps from the displacement spectra. a) Three color filter functions are defined, which equally span the displacement FOV, to give weights to red, green and blue colors based on the amount of displacement. b) These color filters are applied to the displacement spectra of all image voxels. Two color-coded displacement maps are generated corresponding to LR and AP displacement-encoding directions.

In-vivo Study to Probe Arterial Sources

Next, we perform an in-vivo study to show that DiSpect can be used to trace more complex geometries, for example, determine the arterial sources that supply different regions of the brain. In order to shorten the total acquisition time, a faster single-shot EPI readout was used for image acquisition. A spatial saturation band was placed covering the imaging slice and the top of the head, which was used to suppress signal from veins and static tissue. The axial imaging slice and saturation band were placed as shown in Figure 3.12a. Electrocardiogram (ECG) triggering was used to synchronize the acquisitions with the cardiac cycle.

In general, the sources of each location in the target imaging slice are three dimensional. To limit the scan time, 2D coronal displacement encoding along the LR and superior–inferior (SI) directions are performed. The coronal displacement spectra, orthogonal to the axial imaging slice, are projected along the AP direction. The acquisition was conducted with a TR of $2s$, a target image resolution of $3 \times 3\text{mm}^2$, target FOV of $19.2 \times 19.2\text{cm}^2$, source displacement resolution of $6 \times 6\text{mm}^2$, and a source FOV of $48 \times 60\text{mm}^2$. Multiple image acquisitions were performed repeatedly after tagging between mixing times of $100ms$ to $800ms$, in $100ms$ intervals.

3.5 Results

Simple Planar Flow Phantom Study

The two DiSpect acquisitions were combined to trace the sources of water flowing through the flow phantom. The 1D displacement spectra in the LR and AP displacement-encoding directions are displayed for a target image voxel in Figure 3.10b. The information from the two 1D spectra can be combined to determine the sources that flow into the target voxel. The corresponding sources are shown in red. Two additional target voxels can be selected in green and their sources can be resolved similarly in red (Figure 3.10c). It can be seen that DiSpect can resolve contributions to the target voxel from two different branches of the phantom.

As a result of applying the color filter functions defined in Figure 3.11a, two color-coded displacement maps are generated corresponding to LR and AP displacement-encoding directions (Figure 3.11b). Assuming that water moves at a constant velocity during the mixing time, these color-coded displacement maps can provide a measurement proportional to the velocity of water in different regions of the imaging slice.

In-vivo Study to Probe Arterial Sources

To demonstrate the capability of DiSpect to trace arterial sources, we selected three target regions from the imaging slice (Figure 3.12b). The sources of each target region were overlaid on a coronal MR Angiography (MRA) image, in the corresponding colors (Figure 3.12c). DiSpect can successfully identify the arterial sources corresponding to the left and right

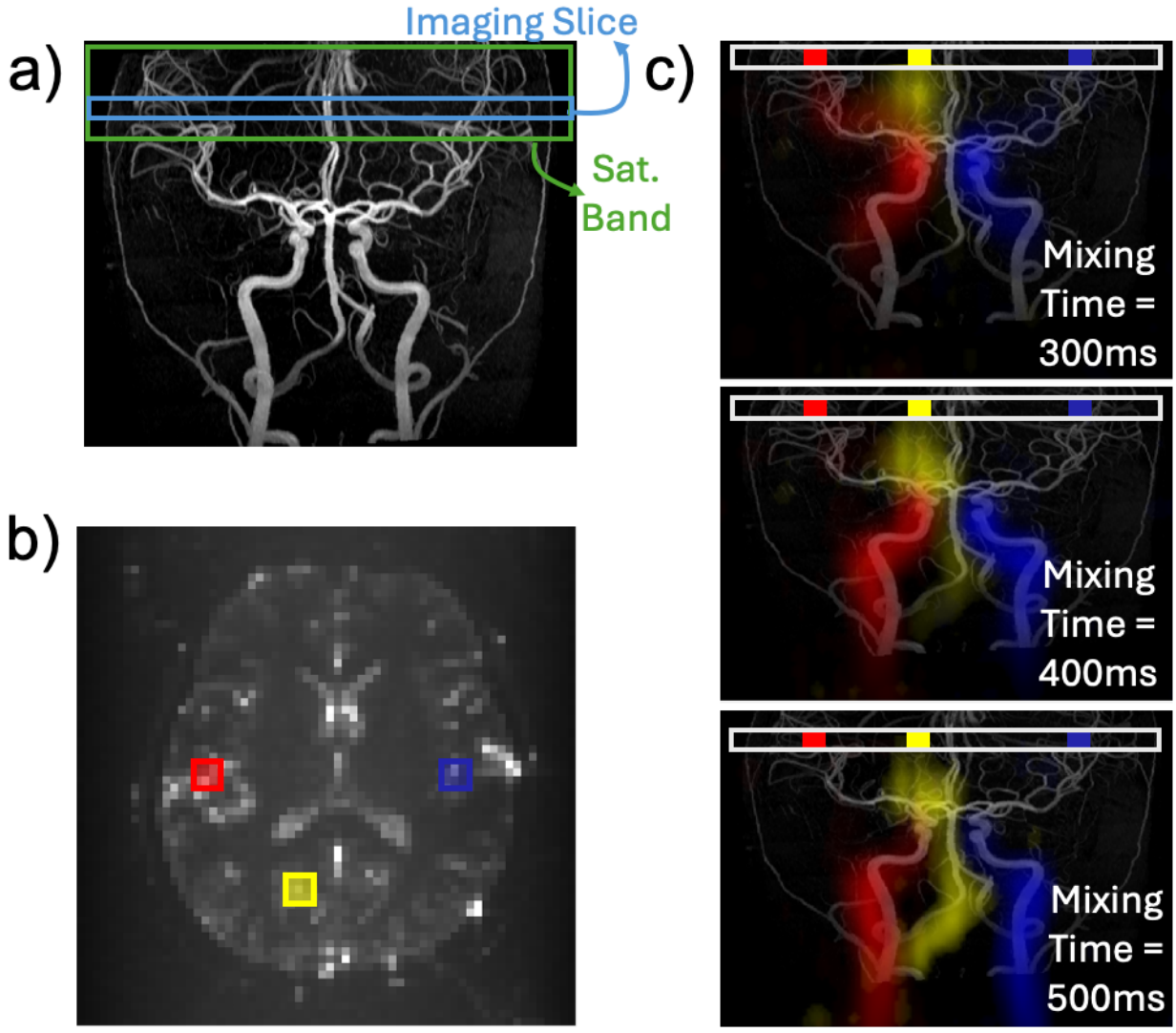

Figure 3.12: In-vivo study demonstrating the ability of DiSpect to trace arterial sources. a) Imaging setup showing the placement of the axial imaging slice and saturation band on the coronal MR angiography image. b) Three regions are selected from the target imaging slice. c) The sources of each target region, measured by DiSpect, are overlaid on the coronal MRA image in the corresponding colors. The sources of each region were traced to the left carotid, right carotid and vertebral arteries. With increasing mixing times, blood coming from sources farther away can be measured.

carotid arteries as well as the vertebral arteries. The measured sources align nicely with the underlying vessel structure depicted by the MRA. With longer mixing times, sources farther

away are able to reach the imaging slice and can be detected with DiSpect.

3.6 Discussion

DiSpect produces a rich dataset, which can be used to study various complex spin dynamics. In the first experiment, we demonstrate that DiSpect can trace fluid pathway of water moving through a simple, planar phantom. It would not be possible to capture the full dynamics of this phantom with DENSE, as there are partial volume effects when water from different tube sections merge into the same region. With DiSpect we can resolve contributions from multiple sources by measuring a 1D displacement spectrum along two directions. We also show that we can use the measured displacement spectra to estimate flow velocity in the two directions. For this simple phantom design, 1D displacement spectra are sufficient to capture the full dynamics of flow. However, in the presence of more complex geometries, higher dimensional displacement spectra are needed to resolve the sources in its entirety. However, the total acquisition time increases with the number of displacement encodings, making the acquisition of a 3D displacement spectrum very time-consuming. Therefore, in the in-vivo experiment, 2D fully sampled displacement spectra are acquired.

In our in-vivo experiment, target regions from the imaging slice were selected and the displacement spectra were used to determine their respective arterial sources. By acquiring a 2D displacement spectrum, DiSpect can resolve more complex arterial sources that feed different target regions. The arterial sources were nicely aligned with the underlying structure depicted by the MRA.

One limitation of our in-vivo study was that although DiSpect was able to resolve the sources of target regions that were rich with large vessels, it showed limited signal in other areas. This was due to the fact that displacement spectra were acquired repeatedly after tagging. Once blood water spins arrive at the imaging slice, their magnetization is crushed due to the image acquisition, even though these spins continue to perfuse within the slice. Therefore, the signal contribution was mainly coming from spins that were previously outside the imaging slice, which are the larger arteries with faster flows. A potential way to resolve this issue could be to acquire images with a lower temporal resolution, or to only acquire a single image after tagging.

By using a stimulated echo approach DiSpect can trace sources of blood flow over long evolution times, only limited by T_1 decay. DiSpect alleviates any gradient amplitude limitations, which are present in PC MRI. We have shown that DiSpect provides information to trace the sources of water in a simple flow phantom as well as more complex arterial sources in-vivo.

3.7 Conclusion

In this chapter, I describe and demonstrate a new tool, DiSpect, which can probe complex tissue dynamics. DiSpect performs multiple DENSE acquisitions with increasing displacement encodings to resolve a multi-dimensional source displacement spectrum for each image voxel. The potential of DiSpect was demonstrated with flow phantom and in-vivo experiments. DiSpect is a highly versatile technique, which can be used in various alternative ways, opening the possibility to qualitatively and quantitatively measure complex spin dynamics.

Chapter 4

Venous Perfusion Source Mapping with DiSpect

4.1 Introduction

The hemodynamics of the cerebral venous system play a crucial role in ensuring sufficient brain perfusion to maintain cerebral function [56]. While cerebral arterial disorders are well studied and understood, the knowledge on the venous drainage mechanism of the brain is much more limited [9]. This is largely attributed to the person-to-person variability in the cerebral venous physiology and the limitations of current imaging technologies [10]. Nevertheless, venous abnormalities play an important role in the pathophysiology of several important neurological conditions. For instance, veins are involved in vascular disorders such as venous sinus thrombosis [11], dural arteriovenous fistulas [12], and idiopathic intracranial hypertension [13]. Emerging evidence suggests potential venous involvement in several other neurological disorders including multiple sclerosis, idiopathic Parkinson's disease, leukoaraiosis and normal-pressure hydrocephalus [14, 15]. Moreover, it is believed that there is an interplay between venous and cerebrospinal fluid (CSF) flows and pressures; however, the exact relationship, particularly concerning venous and CSF hypertension remains unclear [16].

Digital subtraction angiography (DSA), albeit being the gold standard to image many vascular disorders involving the venous system, is an invasive procedure with life-threatening stroke risks [21, 22]. Several non-invasive, non-contrast-agent based MRI methods have been developed to resolve vascular structure, blood flow velocity and arterial perfusion. Arterial Spin Labeling (ASL) uses blood water as an endogenous tracer by inverting blood magnetization using RF pulses [7]. Although this method is frequently used to study arterial perfusion, it is not suitable for veins because of the lack of a single labeling plane. Primary non-invasive tools to probe the venous system are Time of Flight (TOF) MR Venography (MRV), which relies on inflow effects, and phase-contrast (PC) MRI that encodes instantaneous flow velocity into signal phase [9, 24, 25]. TOF MRI is limited to imaging the venous

structure and provides minimal information on flow dynamics. PC MRI requires very large velocity encoding gradients to capture slower flows, potentially leading to phase offset errors and reducing the accuracy of the measured velocities [26]. Therefore, it is mainly limited to probing flow velocity in sinuses and larger veins.

To address the challenges in venous imaging with MRI, I develop a venous perfusion source mapping method with DiSpect. In this application, the spatial information gets encoded into the magnetization of blood water spins across the entire brain during tagging and remotely detected once the tagged blood reaches the imaging region – often near the brain's surface, where the signal-to-noise ratio is 3-4× higher. This method can trace the origin of blood water that moves into the imaging slice over short (10 ms) to long (3 s) mixing times. This unique capability allows blood sources to be traced regardless of their path and velocity, enabling measurement of slow blood flow in smaller veins and potentially in capillary beds. Additionally, by placing the imaging slice on large veins where blood is quickly refreshed, blood sources can be probed through repeated imaging without disturbing perfusion. In this chapter, I demonstrate perfusion source mapping using DiSpect in the superior cerebral veins.

4.2 Methods

Signal Model for Perfusion Source Mapping

First, I would like to describe the signal model for the source displacement spectra that are acquired. For this application, the source displacement spectra are called **perfusion source maps**, as they depict the sources of perfused blood from capillary beds and smaller veins that drain into a larger cerebral vein.

The perfusion source map of a target image voxel represents a map of spins that moved into that target voxel at some time point, t. The perfusion source maps are in relative coordinates to the location of the target voxel. The source map amplitude of a target voxel $\vec{r}$, displacing from a source position $\vec{\Delta r}$ away is:

$$s_{\vec{r}}(\vec{\Delta r}, t) = M(\vec{r}) p_{\vec{r}}(\vec{\Delta r}, t) e^{\frac{-t}{T_1}}. \tag{4.1}$$

Here, $M(\vec{x})$ is a constant depending on the total amount of blood magnetization that moves into the target voxel, $p_{\vec{r}}(\vec{\Delta r}, t)$ is a function representing the ratio of blood that displaced into the voxel at time t from a source position $\vec{\Delta r}$ away, and $e^{\frac{-t}{T_1}}$ is a term representing T_1 decay. Therefore, qualitatively, the signal intensity at a source location reflects the relative portion of blood that moved from that source location to the target image voxel. It is possible to convert the blood magnetization amplitude, $M(\vec{r})$, to the volume of blood using a separate calibration scan, which can be performed in the future to obtain quantitative values of the volume of blood.

Implementation Details

For venous imaging acquisitions, the pulse sequence was designed and simulated using SpinBench (Vista.ai, Palo Alto, CA). The sequence was deployed on a 3T GE MR750W system (Waukesha, Wisconsin) using the RTHawk platform (Vista.ai, Palo Alto, CA), a vendor-neutral, proprietary platform for MRI sequence development. Cardiac gating was performed for all acquisitions. For image acquisitions, a single-shot spiral readout was employed, which allows for a shorter echo time and reduced sensitivity to flow effects [57].

Single-shot spiral acquisitions are prone to off-resonance artifacts due to their long readout durations ($12 - 14ms$). To correct these artifacts, I employed a multi-frequency reconstruction approach. Images were reconstructed at frequency offsets ranging from -50 Hz to 50 Hz in 10 Hz intervals. For different locations within the imaging slice, the frequency that yielded the best sharpness was determined.

Experiment 1: Perfusion Source Mapping of the Superior Sagittal Sinus

To demonstrate the ability to perform venous perfusion source mapping with DiSpect, a 2D coronal slice was imaged at the back of the head, placed on the superior sagittal sinus (Figure 4.1a). A saturation band was placed around the imaging slice to suppress signal from static tissue. During the mixing time between tagging and imaging, blood sources from superior veins as well as surrounding tissue will drain into the superior sagittal sinus where it gets imaged (Figure 4.1b). The DiSpect acquisition was performed with 2D displacement encoding in the AP and SI directions, resulting in a 2D sagittal perfusion source maps (projected along LR). The acquisition was performed with a TR of $2s$. The target image resolution was $4 \times 4\text{mm}^2$, $15 \times 15\text{cm}^2$ FOV and the source displacement resolution was $6 \times 6\text{mm}^2$, $14.4 \times 9\text{cm}^2$ source FOV. Image acquisitions were performed repeatedly after tagging, acquiring displacement spectra at mixing times from 100ms to 1.4s, in 100ms increments. For visualization, an ROI containing the superior sagittal sinus was selected from the image (Figure 4.1c).

Experiment 2: Perfusion Source Mapping of Individual Superior Veins

The initial experiment to map the perfusion sources of the superior sagittal sinus has several limitations. When the imaging slice is placed at the back of the head, blood from the entire superior venous system drains into a single location in the imaging slice. To prevent aliasing, the acquisition has to be made with a large source FOV. Additionally, displacement encoding is performed only along two directions, causing information to be projected along the LR axis, which cannot be recovered.

To address some of these limitations, in the second experiment, I placed an axial imaging slice towards the top of the head. The axial slice goes through the superior sagittal sinus

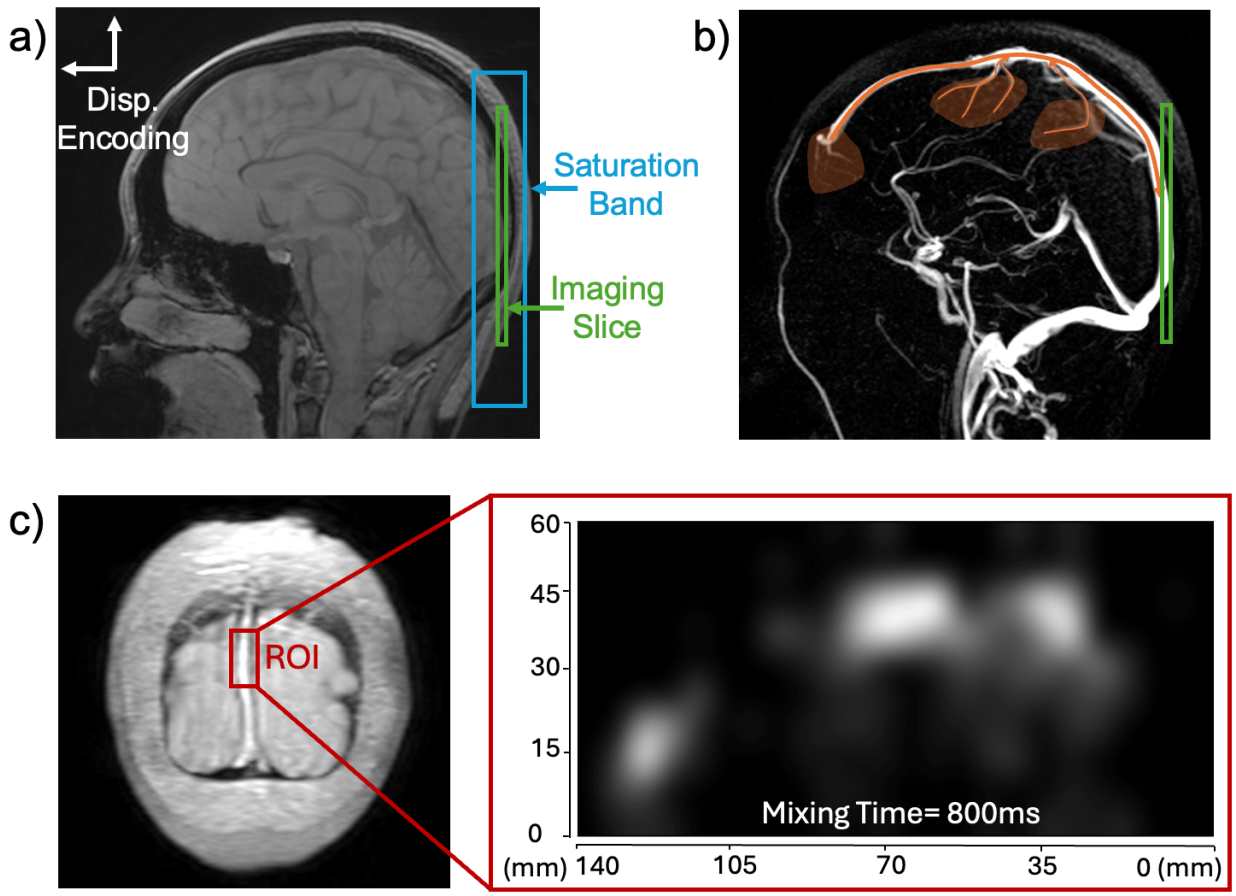

Figure 4.1: Perfusion source mapping of the superior sagittal sinus. a) A 2D coronal slice was imaged at the back of the head with a spatial saturation band placed around it to suppress static tissue signal. A DiSpect acquisition with 2D sagittal displacement encoding was performed. b) During the mixing time, blood from the superior veins and capillary beds will drain into the superior sagittal sinus where they will get imaged. c) An ROI containing the superior sagittal sinus was selected from the image. The perfusion source map for the selected ROI at a mixing time of $800ms$ is shown.

and several smaller superior veins (Figure 4.2a). In this case, different superior veins will drain into different locations in the imaging slice. By selecting regions from the imaging slice that contain different superior veins, the sources of each vein can be isolated and traced independently (Figure 4.2b). This creates the possibility for the acquisition to be made with a smaller source FOV.

A DiSpect acquisition with 2D coronal displacement encoding is performed. The resulting source maps are projected along the AP direction. However, this projection only occurs

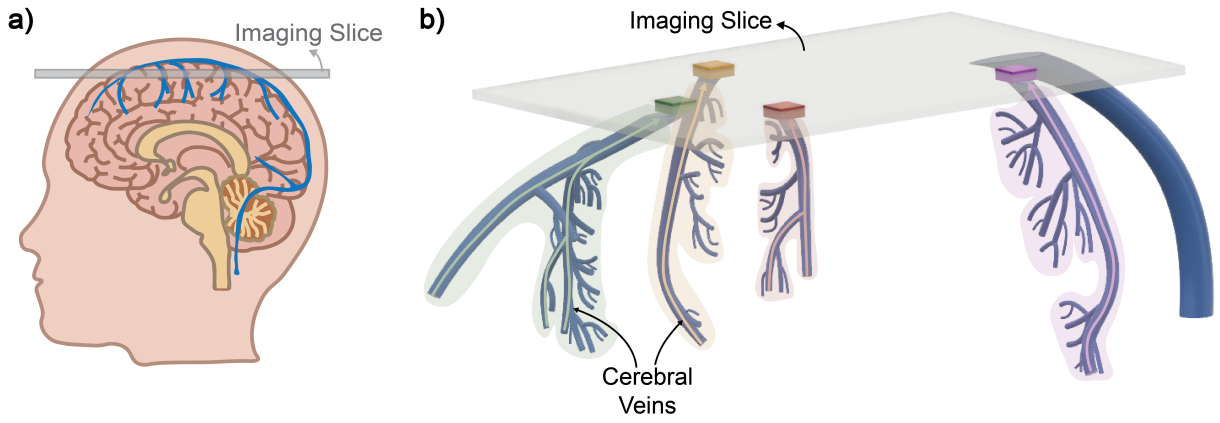

Figure 4.2: Concept of venous perfusion source mapping. a) An axial imaging slice that goes through the superior sagittal sinus and several smaller superior veins is placed at the top of the head. b) 3D view of the superior cerebral veins and the axial imaging slice. Different superior veins will drain into different regions of the imaging slice. While an axial slice is imaged, the tagged spins will hold information to re-trace the sources of blood coming into each image voxel.

across a thin slab, as the anatomical structure constrains the regions from which blood can drain within a single cortical vein, inherently limiting the blood sources along the AP dimension.

The DiSpect acquisition was performed with a TR of $3s$. The target image resolution for the acquisition was $4 \times 4\text{mm}^2$ with a target FOV of $16 \times 16\text{cm}^2$ and slice thickness of 5mm. A 30mm thick axial spatial saturation band was placed around the imaging slice (Figure 4.3a). The source displacement resolution was $6 \times 6\text{mm}^2$ and the source FOV was $13.2 \times 8.4\text{cm}^2$. Image acquisitions were performed repeatedly after tagging, acquiring displacement spectra at mixing times from $100ms$ to $2.8s$, in $150ms$ increments. Overall scan duration was variable due to cardiac gating but was close to 45 minutes.

Blood vessels flowing through the imaging slice can be identified by examining the displacement spectrum energy of target image voxels and detecting peaks, as marked in Figure 4.3b. From all of the detected regions, I select four that contain different superior veins.

Quantitative Susceptibility Mapping Venography

MR venography was performed to obtain a structure of the cerebral veins to be used for visualization and validation. Initially, I used 3D PC acquisition with a saturation band placed at the neck to suppress any arterial blood to obtain a venogram. Although PC venograms can depict the structure of larger vessels with fast flow, they are unable to resolve the smaller

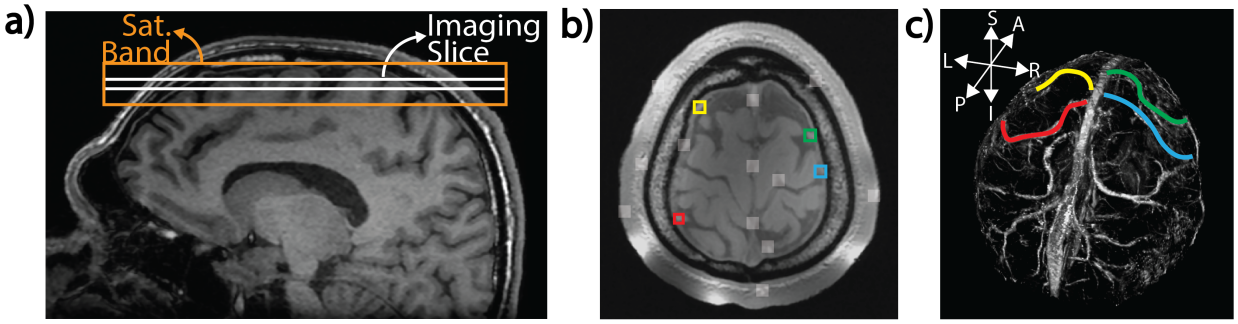

Figure 4.3: Imaging setup for perfusion source mapping of individual superior veins. a) A sagittal image showing the placement of the axial imaging slice and saturation band. b) From the DiSpect acquisition, different vessels that flow through the imaging slice can be identified by examining the displacement spectrum energy of target image voxels and detecting peaks. The detected peaks are overlaid with white ROIs on the image. Four color-coded ROIs are selected out of these regions each containing a different superior vein that drains into the slice. c) The color-coded draining veins overlaid on a 3D QSM-venogram.

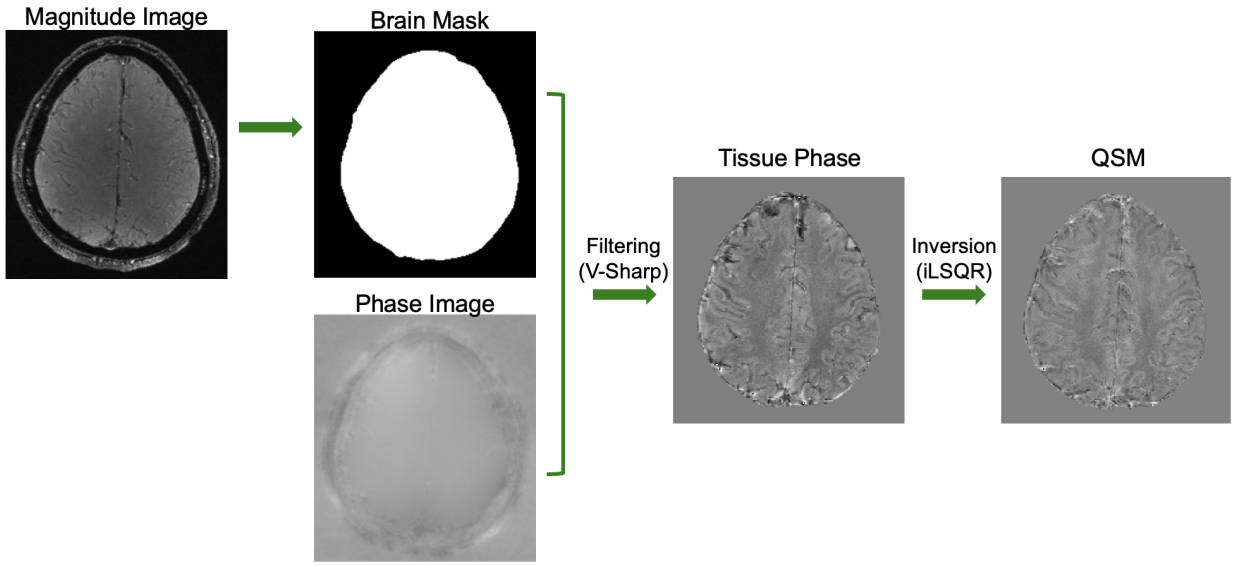

Figure 4.4: The QSM reconstruction pipeline. The magnitude images from the 3D multi-echo GRE acquisition were used to obtain a brain mask [58]. Next, the V-SHARP method is employed for background field removal from the phase images [59]. Finally, dipole inversion was performed using the iLSQR method to obtain QSM images [60].

vessels. To overcome this limitation, I utilized Quantitative Susceptibility Mapping (QSM) [61, 62], which produces a detailed map of the veins by measuring susceptibility differences rather than flow velocity, thereby resolving the structure of smaller veins.

An axial multi-echo 3D Gradient Echo (GRE) sequence was performed with 16 echo times, resolution = 0.8x0.8x0.8mm^3, first echo time (TE) of 2.12ms, ΔTE=2.42ms, TR=41.0ms, FOV=21x21x13cm^3, and Flip Angle =12^o. STI Suite V3.0 [63] was used to obtain susceptibility maps for each echo time. The QSM reconstruction pipeline is shown in Figure 4.4. The magnitude images from the multi-echo GRE acquisition were used to obtain a brain mask [58]. Next, the V-SHARP method is employed for background field removal from the phase images [59]. Finally, dipole inversion was performed using the iLSQR method to obtain QSM images [60]. The obtained QSM images were then averaged across echo times for visualization purposes.

To demonstrate the difference between PC and QSM venograms, axial and coronal projections of each venogram are shown in Figure 4.5. It is evident that the QSM venogram can reveal the detailed structure of smaller veins that the PC venogram cannot resolve.

4.3 Results

Experiment 1: Perfusion Source Mapping of the Superior Sagittal Sinus

The results of the first experiment mapping the perfusion sources of the superior sagittal sinus are shown in Figure 4.6. The perfusion source maps obtained from the selected ROI are overlaid on the sagittal projection of the PC venogram. The results are shown from 200ms to 1.2s in 200ms increments (Figure 4.6). At the initial mixing times, the perfusion source maps mainly show signal from the superior sagittal sinus. At the later mixing times, blood starts arriving from superior veins lower down, which is depicted by the source maps. The signal is more dispersed at the higher mixing times, which could be reflecting blood arriving from smaller veins.

Experiment 2: Perfusion Source Mapping of Individual Superior Veins

For visualization, the coronal perfusion source maps for each vein at different mixing times were overlaid on the corresponding venous anatomy. The coronal vein anatomy was visualized for each vein with a maximum intensity projection of the echo-averaged QSM along the AP direction. The slab thickness for the projection was determined based on the extent of the vein along the AP direction. The perfusion source maps were interpolated to match the resolution of QSM. Since the perfusion source map of each target voxel is relative to the position of that voxel, the interpolated maps were shifted to absolute spatial coordinates.

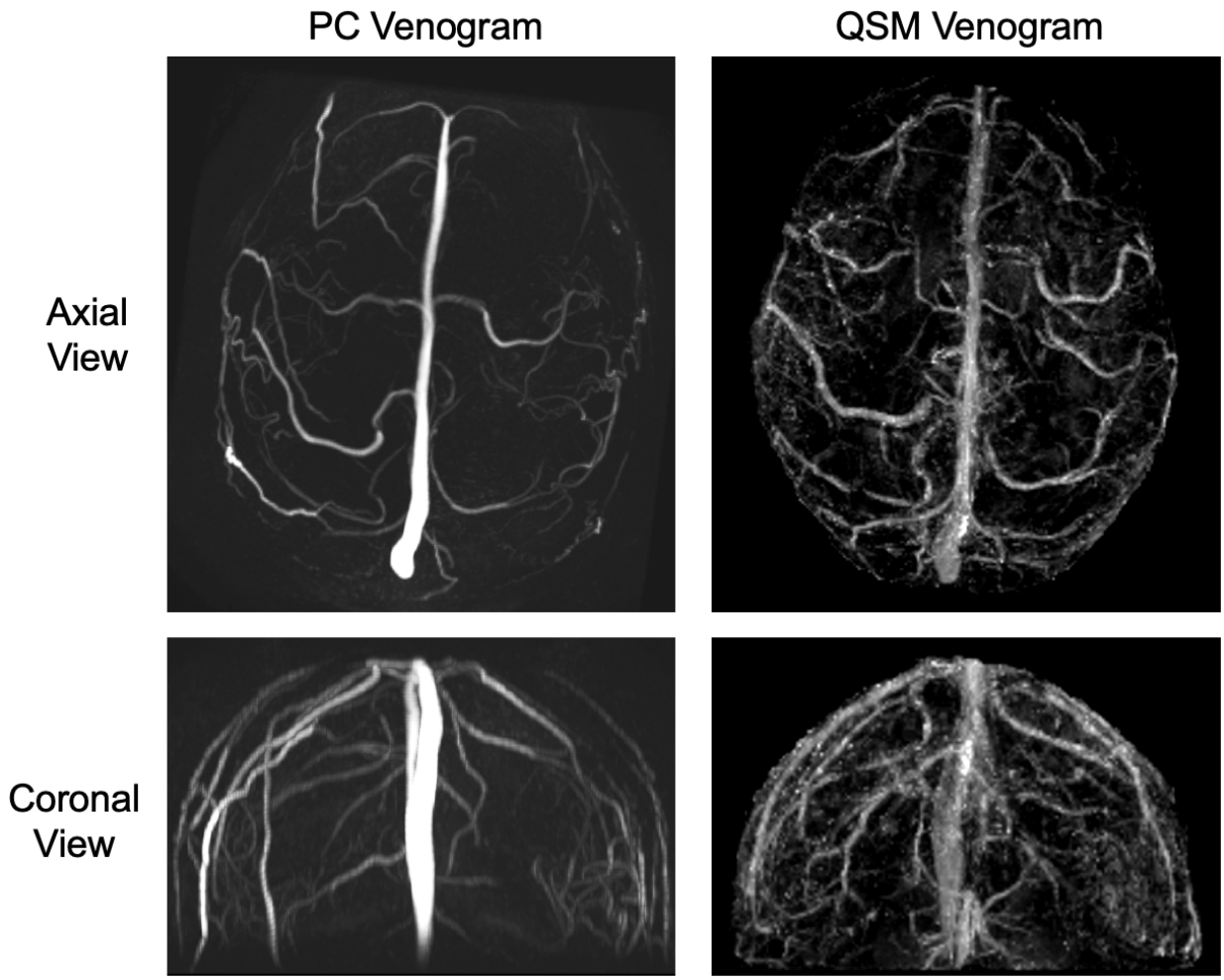

Figure 4.5: Illustration of the differences between PC and QSM venograms. Axial and coronal projections are shown for each case. The QSM venogram can reveal the detailed structure of smaller veins that the PC venogram cannot resolve. Note that some superficial veins are present in the PC venogram but not in the QSM venogram due to the brain mask.

During the mixing time between tagging and imaging, tagged blood moves from capillary beds into the superior veins where it gets imaged. The perfusion source maps delineate the sources of blood that move into the superior veins over 700, 1000, 1300, 1600 and 1900ms (Figure 4.7). By combining information from the perfusion source maps across different evolution times, the venous territory drained by each superior vein can be determined. The territory of each vein is marked with a dashed line.

To gain a deeper understanding of the signals in the perfusion source maps, I select various ROIs within the territory of each superior vein (Figure 4.8a). I then plot the perfusion source

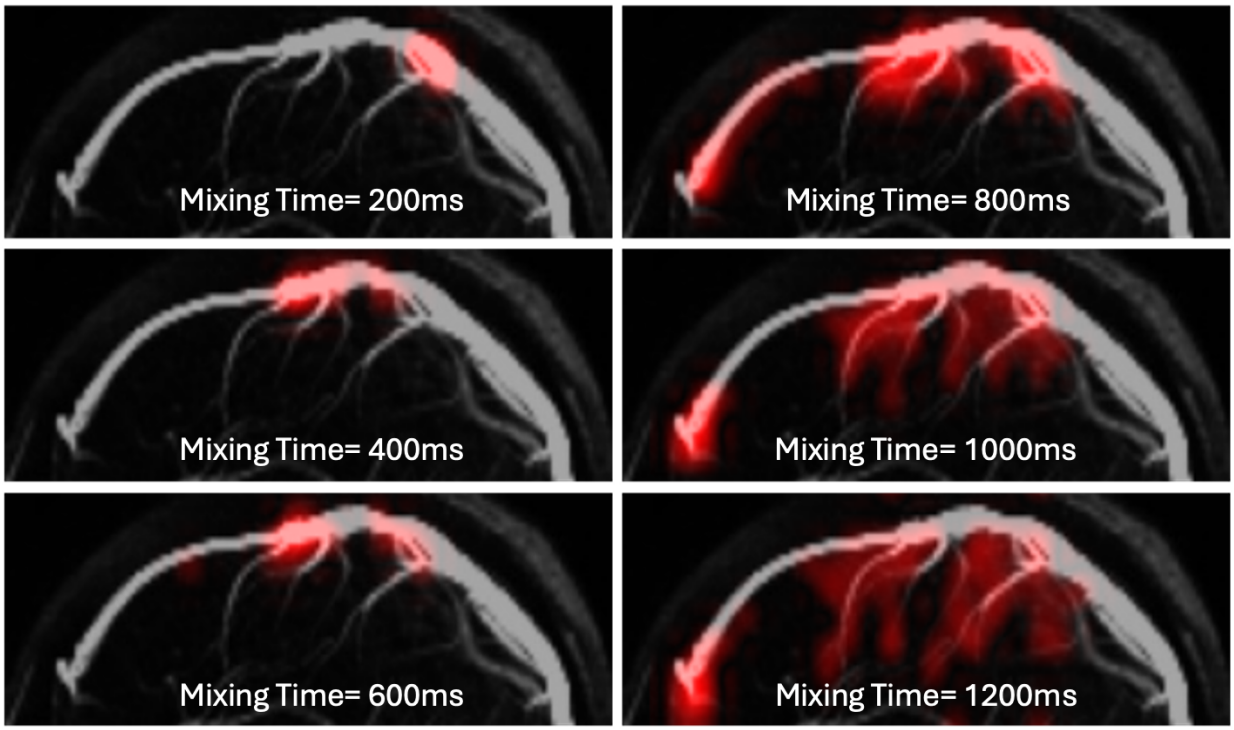

Figure 4.6: Perfusion source maps at different mixing times depicting the sources of blood draining into the superior sagittal sinus. At the shorter mixing times, the signal is mostly contained in the superior sagittal sinus. At longer mixing times, blood starts arriving from the superior veins lower down.

signal from this ROI as a percentage of the total source signal entering the target voxel at that mixing time, i.e $\frac{s_{\vec{x}}(\vec{\Delta x},t)}{\int_{\Delta\vec{x}} s_{\vec{x}}(\vec{\Delta x},t)}$ (Figure 4.8b). The definition of $s_{\vec{x}}(\vec{\Delta x},t)$ can be found in Equation (4.1).

4.4 Discussion

Perfusion source mapping with DiSpect is a versatile technique to probe cerebral venous dynamics. DiSpect's unique capability to trace the fluid pathway of blood spins across short to long time scales, regardless of the path and velocity, enables it to measure blood flow through a variety of vessels, ranging from capillary beds and smaller veins to larger sinuses.

Initially, I demonstrated DiSpect's ability to trace perfusion sources of the superior sagittal sinus. I show that the blood sources draining into the superior sagittal sinus can be dynamically mapped at different mixing times. However, the entirety of superior veins drain into a single location in the imaging slice, requiring a large source FOV to avoid aliasing.

Furthermore, this imaging setup does not allow for the geometry of the superior veins to be leveraged.

For the second experiment, I placed an axial slice towards the top of the head, intersecting the superior sagittal sinus and several superior veins. I can leverage the venous anatomy to select different target regions and dynamically resolve their sources of blood, mapping the perfusion of different superior veins individually. At shorter mixing times, the perfusion sources appear to be more focal, originating primarily from within large veins, whereas at longer mixing times, the sources appear more dispersed, as blood arrives from smaller veins and capillaries. Effectively, the temporal dynamics of venous perfusion are being imaged in reverse. For visualization, the perfusion source maps were overlaid on a QSM-venogram depicting the detailed structure of the veins. Notably, the maps overlap very well with the underlying venous structure depicted by the QSM-venogram images.

Across mixing times, the distribution of perfusion sources within the venous territory will change. These distribution changes can be visualized by looking at 1D source signal series of different ROIs within the venous territory. ROIs close to the large veins (ROI #1 in red) will have a peak followed by a sharp decay, whereas, ROIs closer to the smaller veins and tissue (ROI #1 in yellow) will have high signal across a wider range of mixing times.

Notwithstanding its versatility, perfusion source mapping is currently constrained by several limitations. One limitation is that the acquisition of the high-dimensional dataset is very time consuming. For this reason, 2D perfusion source maps were acquired with low source resolutions. However, the perfusion sources are highly sparse and since flow is continuous they exhibit substantial temporal and spatial redundancy. In addition, the sources of blood are constrained by the venous anatomy. Future work could accelerate acquisitions by using partial Fourier or variable density sampling, and a regularized reconstruction [64–66]. Moreover, physiological noise, especially due to the pulsatility of the static brain tissue, can play an important role at longer mixing times as additional cardiac cycles occur between tagging and imaging. Reducing physiological noise by periodically saturating signal from static tissue or detecting and accounting for the additional cardiac cycles is another area of future work.

Despite these limitations, the unique properties of the novel venous perfusion source mapping method can be summarized as follows:

1. **Remote detection:** During tagging, spatial information is encoded across the whole brain volume. This encoded information is remotely detected [67, 68] at an imaging slice placed close to the brain's surface, where the signal-to-noise ratio is $3-4\times$ higher.

2. **Geometry:** While it is generally possible to resolve the sources of each target voxel in 3D, this process is time-consuming due to the need for repeated spin-tagging and encoding. Here, I use 2D source encoding, projected along the third dimension. By selecting target regions containing different superior veins the sources of each vein can be isolated. This allows the sources to be projected over a thin slab that is constrained by venous anatomy.

3. **Dynamic Perfusion Sources:** The technique is particularly well-suited to image veins where blood from smaller branches merge together to form larger flows, in contrast to arteries, where blood diverges and spreads into smaller branches. To probe venous perfusion, I can image larger veins where blood is quickly refreshed and the sources of blood draining into these veins from tissue outside of the imaging slice can be traced dynamically without disrupting tissue perfusion. These dynamic maps reflect average perfusion as they are constructed from data collected from many DiSpect encodings over half an hour. The information from perfusion maps at different evolution times can be combined to determine the venous territory.

4.5 Conclusion

The approach could open new avenues for imaging various cerebral diseases and enhancing the success of existing imaging techniques. For example, it could facilitate the evaluation of arteriovenous malformations, where arteries and veins form abnormal, complex connections [69]. Perfusion source mapping with DiSpect also holds potential in investigating collateral circulation in ischemic stroke, particularly in cases involving complex vascular bypass networks within the venous drainage system [70]. This tool could also assist in performing hemodynamic analysis of cerebral aneurysms to assess risk [71].

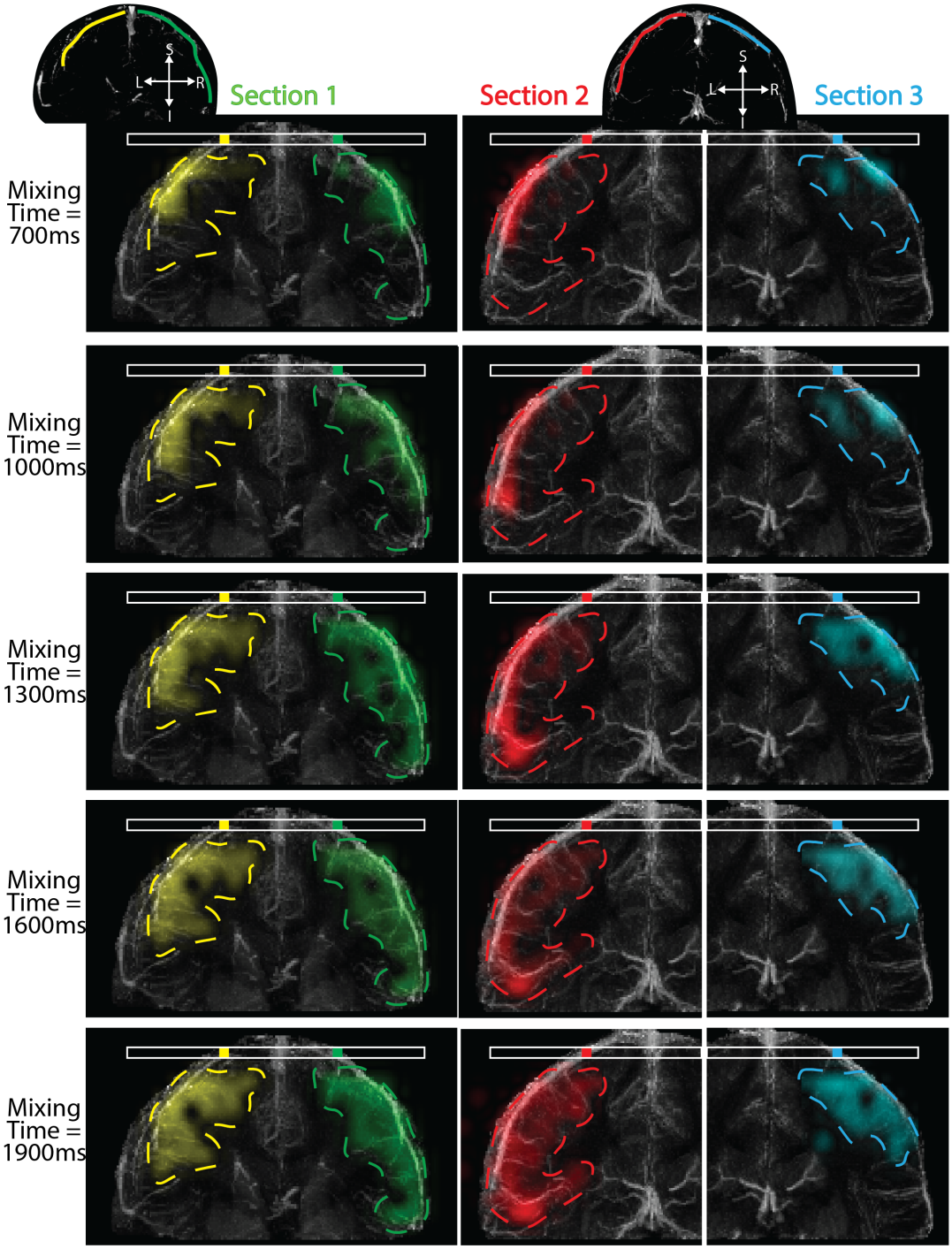

Figure 4.7: Perfusion source maps for four target vein ROIs selected from the imaging slice overlaid on the corresponding coronal sections of the QSM-venograms at mixing times from $700ms$ to $1900ms$ in $300ms$ intervals. For each superior vein, the venous territory is marked with a dashed line.

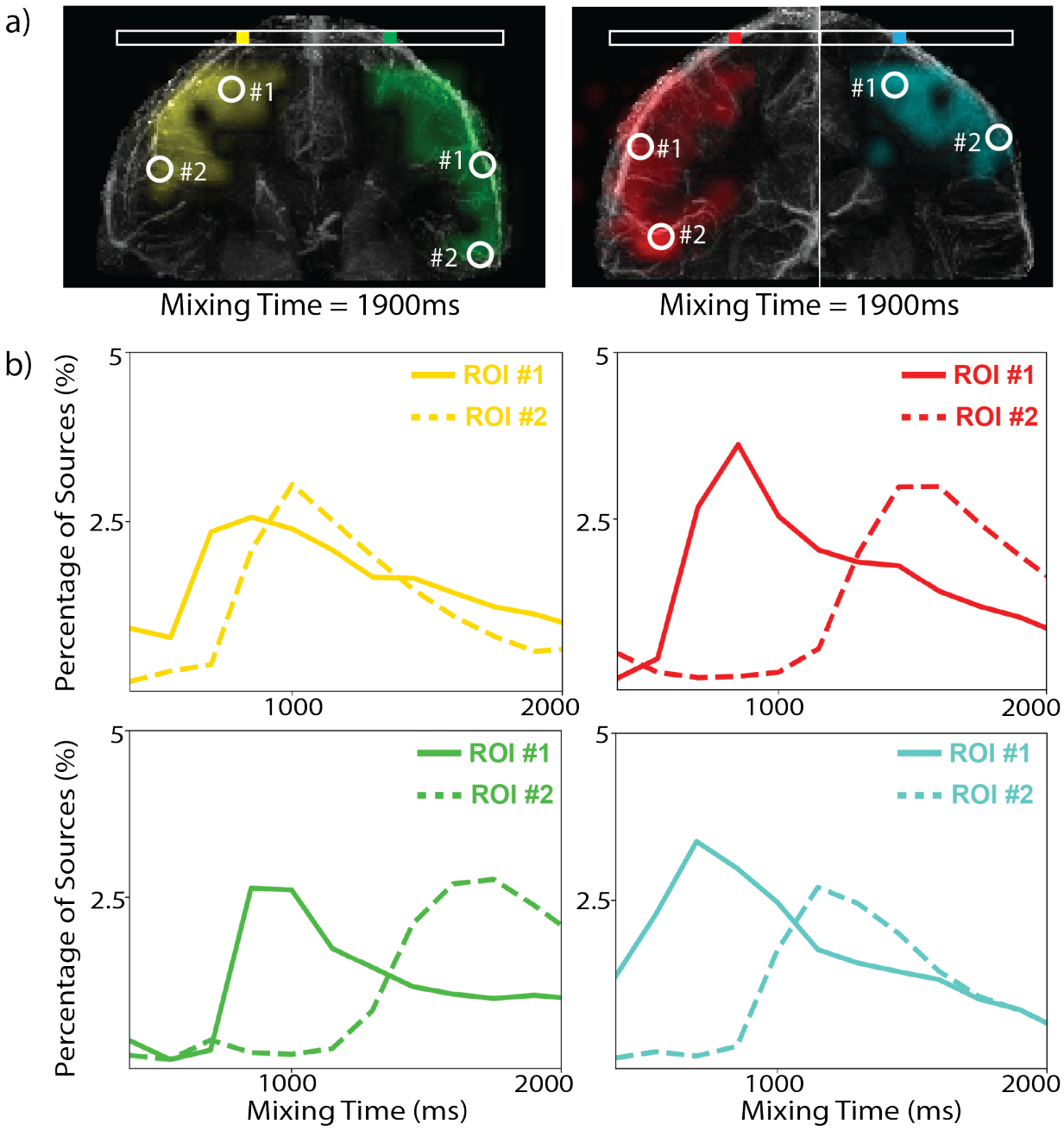

Figure 4.8: Plotting the 1D mixing time signal series at selected ROIs within venous territories of each superior vein. a) The perfusion source maps are displayed for each vein at a mixing time of 1900ms. Two ROIs are selected from the territory of each vein. b) The perfusion source signal from each ROI is plotted as a percentage of the total source signal entering the target image voxel at that mixing time. It is evident from the 1D signal series that the distribution of perfusion sources shows changes across mixing times.

Chapter 5

Sensitivity and Specificity of Venous Perfusion Source Mapping

5.1 Introduction

In the previous chapter, I presented venous perfusion source mapping with DiSpect, which can dynamically image venous perfusion sources spanning from larger veins to smaller veins and perhaps capillary beds. In this chapter, I will first demonstrate the sensitivity of the method to global changes in venous perfusion with a caffeine study. Then, I will establish its specificity by showing that it can consistently and repeatably detect local perfusion modulation due to neural activation. Before moving to more details on how this was achieved, I will present a literature overview on the effects of caffeine and neural activation on perfusion and how this has been previously measured using MRI.

Effects of Caffeine on Global Perfusion

Caffeine is a neurostimulant, which has been shown to globally reduce cerebral blood flow (CBF) using a pulsed ASL technique [72]. In [72], it was shown that the CBF was reduced by 22% to 30% in response to $250mg$ of caffeine. The changes in CBF after caffeine consumption were measured for low, moderate and high users of caffeine and the CBF changes were highest for the low caffeine users when tested in their native state. However, when each category of subjects was tested after abstaining for 30 hours, the changes in CBF were highest for high users of caffeine.

Caffeine has also been shown to reduce flow velocities in middle cerebral arteries using transcranial Doppler ultrasonography [73]. Although venous perfusion changes due to caffeine are not well established, caffeine has been shown to increase venous transit times, defined as the time for blood water to travel from capillaries to major veins [74]. The venous transit times were measured based on changes in T_1 relaxation of water when moving from tissue into veins. However, this method measures an aggregate venous transit time for

all blood draining into the superior sagittal sinus and is unable to resolve local changes in smaller superior veins.

Effects of Neural Activation on Local Perfusion

Neural activity in the brain results in local blood flow and volume modulation near the site of activation. The most widely used method to measure functional brain activity using MRI (fMRI) is called blood-oxygen-level-dependent (BOLD) fMRI. BOLD MRI indirectly measures neural activity by probing local blood oxygenation changes [75]. In the presence of a local blood flow and volume increase, the amount of oxyhemoglobin rises (Figure 5.1a), which in turn increases the local oxygenation levels. BOLD fMRI relies on measuring changes in T_2^*, which increase with higher oxygenation levels (Figure 5.1b).

Task-based fMRI studies are commonly performed in literature to investigate the BOLD response. In a task-based study, the subject performs a task on and off for a specific duration (Figure 5.1c). During each on and off state, the BOLD signal fluctuates according to a hemodynamic response function [75]. This function can be combined with the task timings to fit the acquired signal to a general linear model. Regions where the signal shows a statistically significant fit (usually determined with a T-test) to the model are identified as activated regions.

Venous Effects on BOLD Contrast

Venous effects also contribute significantly to BOLD fMRI. Veins draining the site of neural activity may carry BOLD signals that are displaced from the activated site. This mis-localization of neural activation limits the spatial specificity of the BOLD signal [17–20]. Moreover, veins may exhibit very large BOLD signals, however, this high signal does not necessarily reflect fine-scale neural activity [20, 76–79]. Overall, the venous vasculature has very complex effects on the BOLD signal, and these effects vary across the brain. They are thus difficult to mitigate and cannot be eliminated by averaging out data from an individual subject or across multiple subjects [20]. In addition, there is a limited understanding on how the changes in venous blood flow are regulated during functional activation. Non-invasive methods that measure blood perfusion, flow and volume may help decipher the complex biophysics.

5.2 Global Modulation of Venous Perfusion with Caffeine

Experimental Setup and Acquisition Parameters

Caffeine was used to investigate the capability of perfusion source mapping with DiSpect to detect global venous perfusion changes. To enhance the modulation, the subject, who was

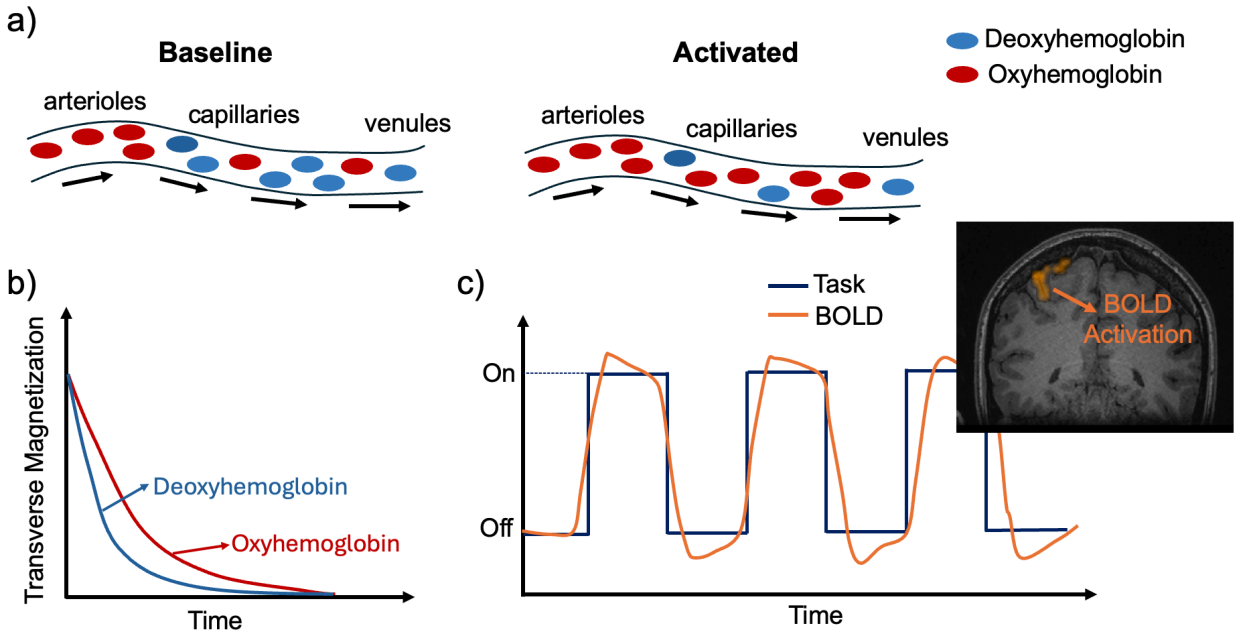

Figure 5.1: Summary of BOLD fMRI. a) During neural activation, the blood flow near the activated site increases. This results in a rise in the amount of oxyhemoglobin. b) The rise in oxyhemoglobin increases the local blood oxygenation. BOLD fMRI relies on measuring changes in T_2^*, which increases with higher oxygenation levels. c) In a task-based fMRI study, the subject performs a task on and off and the BOLD signal fluctuates according to a hemodynamic response function. The acquired signal can be fit to a general linear model to identify regions that are activated.

a regular caffeine consumer, abstained from caffeine consumption for 72 hours prior to the scan. DiSpect acquisitions were performed with the setup shown in Figure 4.3a to map the sources of individual superior veins.

An initial DiSpect acquisition was performed with a TR of $3s$, target image resolution of $4 \times 4\text{mm}^2$ with a target FOV of $16 \times 16\text{cm}^2$ and slice thickness of 5mm. A 30mm thick axial spatial saturation band was placed around the imaging slice. Displacement encoding was performed along the LR and SI directions, resulting in 2D coronal perfusion source maps. The source displacement resolution was $6 \times 6\text{mm}^2$ and the source FOV was $12 \times 7.8\text{cm}^2$. Following this, the subject consumed 225mg of caffeine while retaining the same position on the scanner bed. A second acquisition was performed after a 20 minute delay with identical acquisition parameters. Consequently, two perfusion source maps were obtained for each image voxel: one captured at baseline and one post-caffeine ingestion.

Data Processing and Visualization

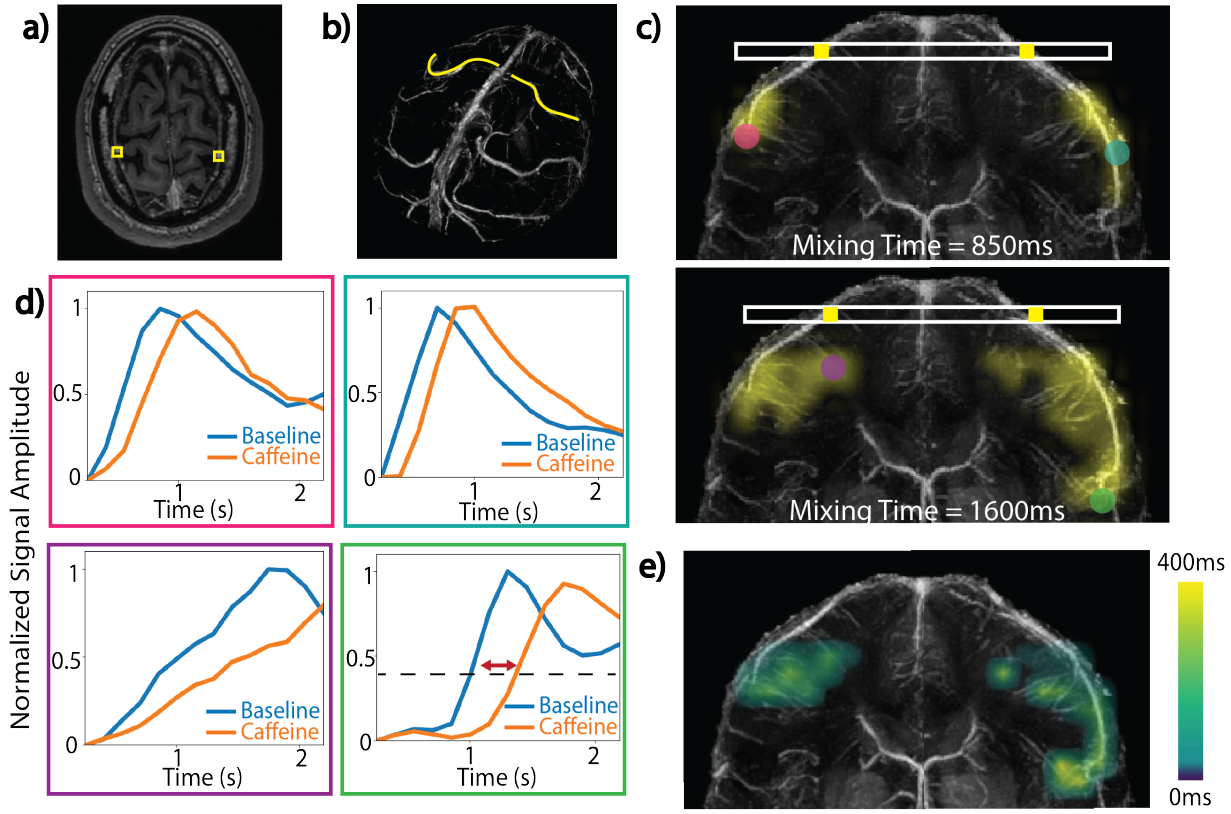

Figure 5.2: Caffeine study demonstrating the ability of DiSpect to detect global changes in perfusion. a) Imaged slice with two selected vein ROIs. b) Selected veins overlaid on a 3D venogram. c) The blood source maps of the selected veins at two mixing times (850ms and 1600ms). d) Two color-coded source ROIs are selected from the blood source maps of each vein. The signal amplitude of each ROI is corrected for T_1 decay, normalized by maximum amplitude and plotted at different mixing times for baseline and post-caffeine states. For all ROIs the peak of the baseline signal occurs earlier than post-caffeine suggesting a delayed arrival after caffeine. e) The delay in arrival time was estimated for each source location in the displacement spectra and displayed for a range of $0 - 400ms$.

To visualize changes in venous perfusion resulting from caffeine, I selected two target image voxels corresponding to different cortical veins as shown in Figures 5.2a-b. The perfusion source maps for the selected veins are shown at mixing times of 850ms and 1600ms (Figure 5.2c). I then picked two regions from the territories of each cortical vein in different colors. The source signal amplitude at each region was corrected for T_1 decay, i.e. multiplied by $e^{\frac{t_{mix}}{T_1}}$ where $T_1 = 1600$ms [80]. Then the signal amplitude was normalized by the maximum

signal amplitude across baseline and post-caffeine states and plotted (Figure 5.2d). The peak signal amplitude is achieved at a shorter mixing time at baseline compared to post-caffeine for all selected regions.

Next, to show the changes in venous arrival times, I first interpolated the mixing time signal series to a $15ms$ time interval. For each source location I identified the shortest mixing time at which the signal amplitude exceeded 40% of its maximum value across all mixing times. The value determined at baseline was subtracted from the post-caffeine value to determine the delay in arrival time. The delay in arrival time was plotted for the range from $0ms$ to $400ms$ (Figure 5.2e). No delays were observed outside of this range.

5.3 Local Modulation of Venous Perfusion with Neural Activation

Modified DiSpect Acquisition for Functional Imaging

Unlike caffeine, which globally affects perfusion, neural activation induces local modulation of venous perfusion. The goal was to investigate the specificity of perfusion source mapping in detecting these local changes. As a proof-of-concept study, I conducted experiments to evaluate changes in perfusion source maps at baseline and during simple motor cortex activation tasks. For this purpose, I developed a modified DiSpect pulse sequence (Figure 5.3). To maintain short functional task durations, the full DiSpect acquisition (20-30 minutes) was split into 20-second partitions. At each partition, 6 repetitions of the DiSpect acquisition were performed. This corresponds to two samples of the displacement k-space, as each displacement k-space sample requires three acquisitions for phase-cycling.

At the beginning of each partition, the subjects were prompted with automated voice commands to "begin" or "stop" a motor cortex functional task. Each partition was repeated during the task and at baseline before proceeding to the next. At the end of the acquisition, the acquired data from different partitions was combined to obtain two blood source maps: one at baseline and one during task (Figure 5.3).

Due to the need to perform the DiSpect acquisition at baseline and during task, the overall acquisition time was on the order of 40-50 minutes. In order to ensure that neural activation was occurring consistently across the long scan duration, a custom multi-slice Spiral-BOLD acquisition was developed. This acquisition was interleaved at the beginning of each DiSpect partition as shown in Figure 5.3.

During neural activation, blood flow and volume in the veins and capillaries within an activated region are modulated. I hypothesized that these perfusion changes can be detected downstream when blood from this region moves into the imaging slice (Figure 5.4). Some of the blood entering a single target image voxel may come from areas within the activated region, while some may come from surrounding non-activated regions. By looking at differences in perfusion source maps obtained at baseline and during task, I expect to determine the regions of the venous territory, which show modulation during neural activation.

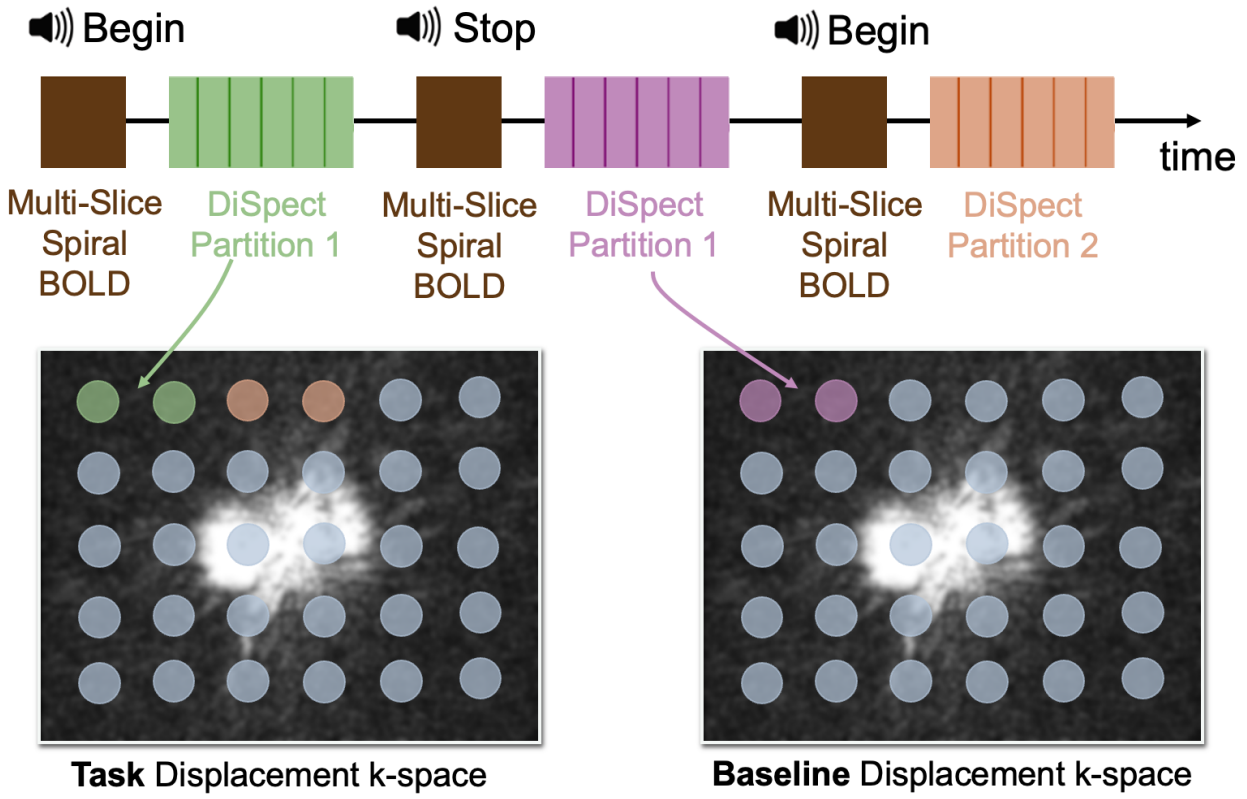

Figure 5.3: Acquisition strategy for the functional study. The DiSpect acquisition is split into 20s partitions, each containing 6 TRs. This corresponds to two points sampled in the displacement k-space. Each partition is repeated during the task and at baseline before moving to the next. A multi-slice Spiral-BOLD acquisition is interleaved between partitions to ensure that activation occurs consistently throughout the scan. Volunteers are instructed to begin and stop the task using automated voice commands. At the end of the acquisition, the acquired data from different partitions is combined to obtain two blood source maps: one at baseline and one during task.

Experimental Setup and Acquisition Parameters

Two subjects were scanned with the modified functional DiSpect acquisition. Each subject underwent two scans on two separate days. For all experiments, 2D displacement encoding was performed along the LR and SI directions, resulting in coronal perfusion source maps. The axial imaging slice was placed close to the top of the head where it intersects the superior sagittal sinus and several superior veins as shown in Figure 5.4. For all acquisitions, the target image resolution was 4x4mm^2, FOV = 16x16cm^2, TR = 3s and slice thickness = 5mm. Image acquisitions were performed repeatedly after tagging, acquiring displacement

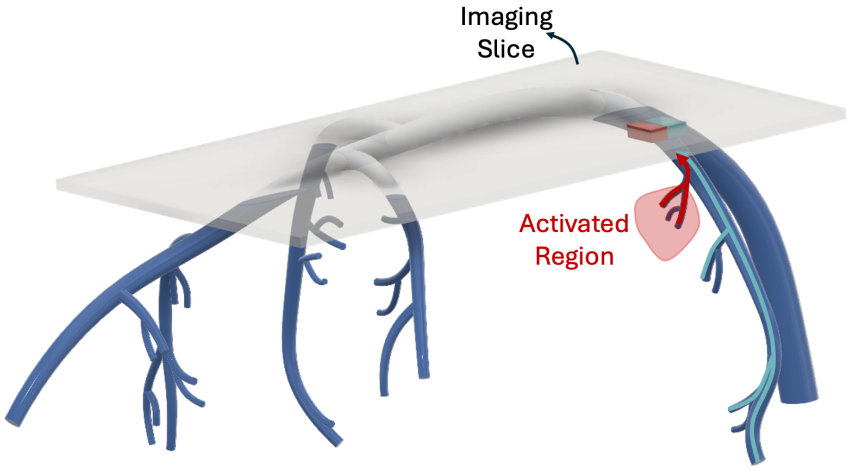

Figure 5.4: Conceptualization of the detection of local perfusion changes. During neural activation, blood flow and volume in the veins and capillaries within an activated region are modulated. I hypothesize that these perfusion changes can be detected downstream when blood from this region moves into the imaging slice. Some of the blood entering a single target image voxel may come from areas within the activated region, while some may come from surrounding non-activated regions.

spectra at mixing times from 100ms to 2.8s, in 150ms increments. A 30mm thick axial spatial saturation band was placed around the imaging slice.

For Subject 1, the first scan was performed with a source displacement resolution of 8x8mm^2 and a source FOV of 11.2x8cm^2, while the subject was instructed to squeeze both hands. A second repeat scan was performed on a different day with a higher source resolution of 6x6mm^2 and a source FOV of 7.2x4.8cm^2, while the subject was instructed to squeeze only their left hand. Subject 2 underwent the same protocol with a source resolution of 8x8mm^2 and a source FOV of 11.2x8cm^2 on two separate days, while being instructed to squeeze their right hand.

For each scan session, a product 2D EPI-BOLD sequence was performed with 29 slices, resolution = 3.3x3.3mm^2, FOV=21x21cm^2, TE=28ms and TR=2s. The subject was cued with vocal commands to perform the same task as during the DiSpect acquisition for 20s on and 20s off for a total duration of 5 minutes. For the custom Spiral-BOLD acquisitions conducted between DiSpect interleaves, a lower image resolution of 4x4mm^2 was selected to reduce off-resonance artifacts. The remaining parameters were identical between the product EPI-BOLD and custom Spiral-BOLD acquisitions. The Spiral-BOLD acquisitions were performed for 5 TRs (10s) at the beginning of each DiSpect partition.

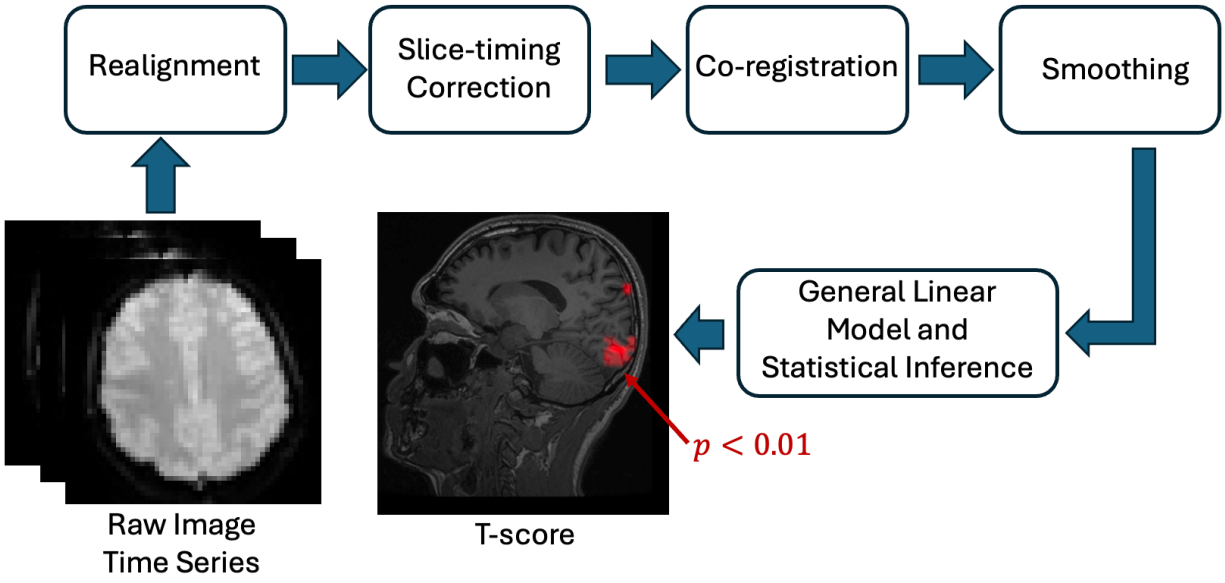

Figure 5.5: Overview of BOLD fMRI processing. The acquired raw image time series is pre-processed by performing realignment, slice-timing correction, co-registration to the 3D QSM volume and smoothing with a kernel size of 3x3x3mm^3. The pre-processed data is then fit to a general linear model and statistical inference is performed to obtain t-statistic images with a significance threshold of $p < 0.01$.

Data Processing and Visualization

EPI BOLD fMRI

The EPI BOLD datasets were pre-processed using SPM12 (`https://www.fil.ion.ucl.ac.uk/spm/`) with the following steps:

1. **Realigning** all volumes to the first volume in the acquired time-series.
2. **Slice-timing correction** to correct for timing differences across different slices in the volume.
3. **Co-registration** to 3D QSM.
4. **Smoothing** with a kernel size of 3x3x3mm^3.

The overall processing pipeline is shown in Figure 5.5. T-statistic images were obtained with a cluster significance threshold of $p < 0.01$ and cluster extent threshold of 10. To visualize the functional activation in the right motor cortex of Subject 1 in more detail, t-statistic images were obtained with a higher cluster significance threshold of $p < 0.05$ and cluster extent threshold of 3.

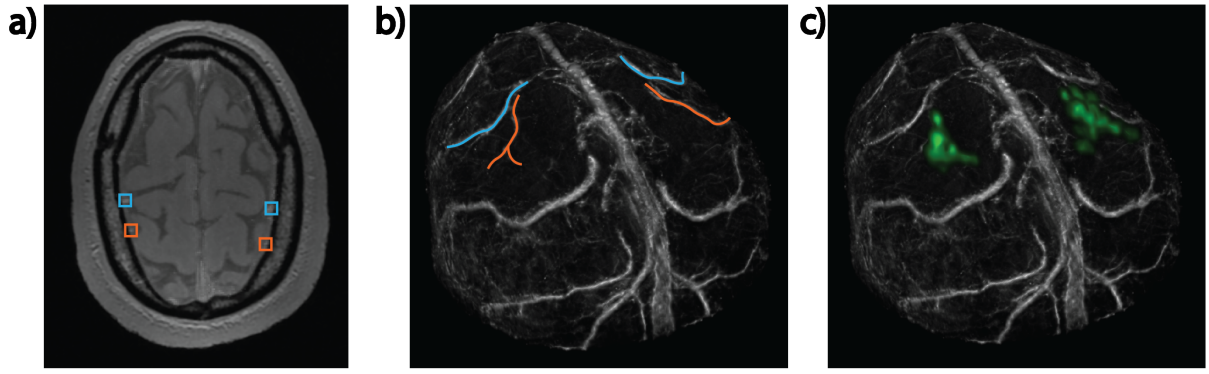

Figure 5.6: Processing setup for bilateral motor cortex activation in Subject 1. a) Imaging slice showing four selected veins: two (orange) drain the activated motor cortices and two (blue) that do not and used as control. b) The color-coded veins overlaid on a 3D QSM-venogram. c) BOLD activations (green) overlaid on the 3D QSM-venogram showing bilateral motor cortex activation.

Percentage Changes in Perfusion Source Maps

To illustrate local blood flow modulation, I selected four veins from Subject 1 during bilateral motor cortex activation: two (orange) veins draining the activated motor cortices and two (blue) veins selected as controls (Figure 5.6a-b). The activated and control veins were chosen based on the significantly activated regions in the EPI BOLD acquisition (Figure 5.6c).

First, I show the perfusion source maps for each of the selected veins at mixing times of $1000ms$ and $1750ms$ (top of Figure 5.7). Next, I determine the percentage change between task and baseline perfusion source maps as

$$\% \quad \text{Change} = \frac{s_{task} - s_{baseline}}{s_{baseline}} \tag{5.1}$$

I display the percentage change for the same two mixing times (middle of Figure 5.7). In the percent change maps, any region exhibiting positive percentage change, where the task signal exceeds baseline, are displayed in red, whereas, any region with negative percentage change is displayed in blue. Coronal projections of the BOLD T-score for the sections containing each vein are shown in the bottom row of Figure 5.7. The territory that each vein is draining is outlined with a dashed line.

Similarly, the results from the first scan of Subject 2 with left motor cortex activation are displayed in Figure 5.8. Here, one activated vein (orange) draining the left motor cortex and one control vein (blue) was selected based on the activated regions in the EPI BOLD acquisition (Figure 5.8a-c). Perfusion source maps and the percentage change between task

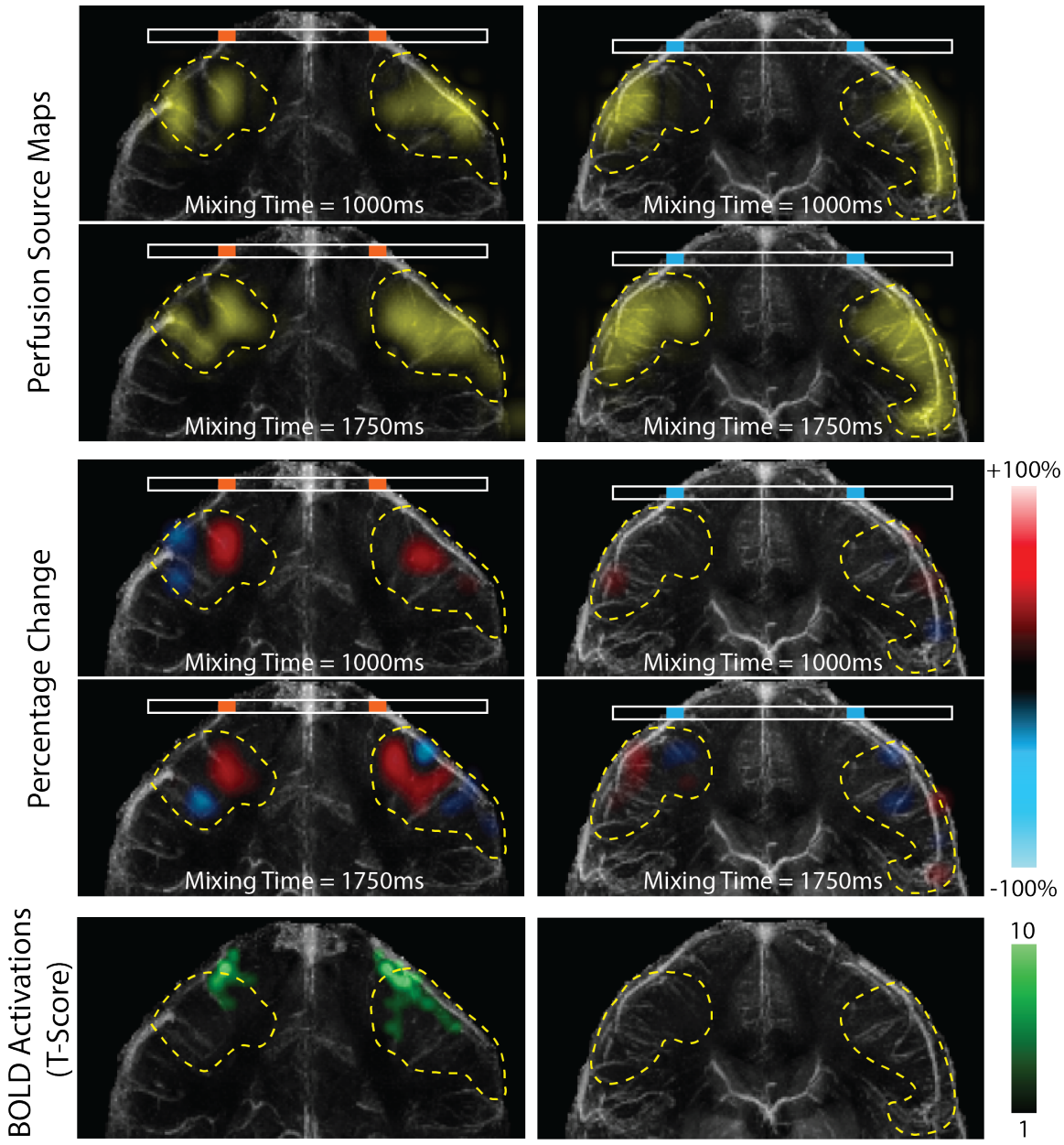

Figure 5.7: Results for bilateral motor cortex activation in Subject 1. **Top:** Perfusion source maps for activated and control veins at two mixing times. **Middle:** The percentage change showing mostly positive and some negative percentage differences in veins draining the activated regions. Little or no percentage change is observed in the veins selected as control. Bottom: BOLD activation map for the coronal sections containing each vein. Venous territories are marked with yellow dashed lines.

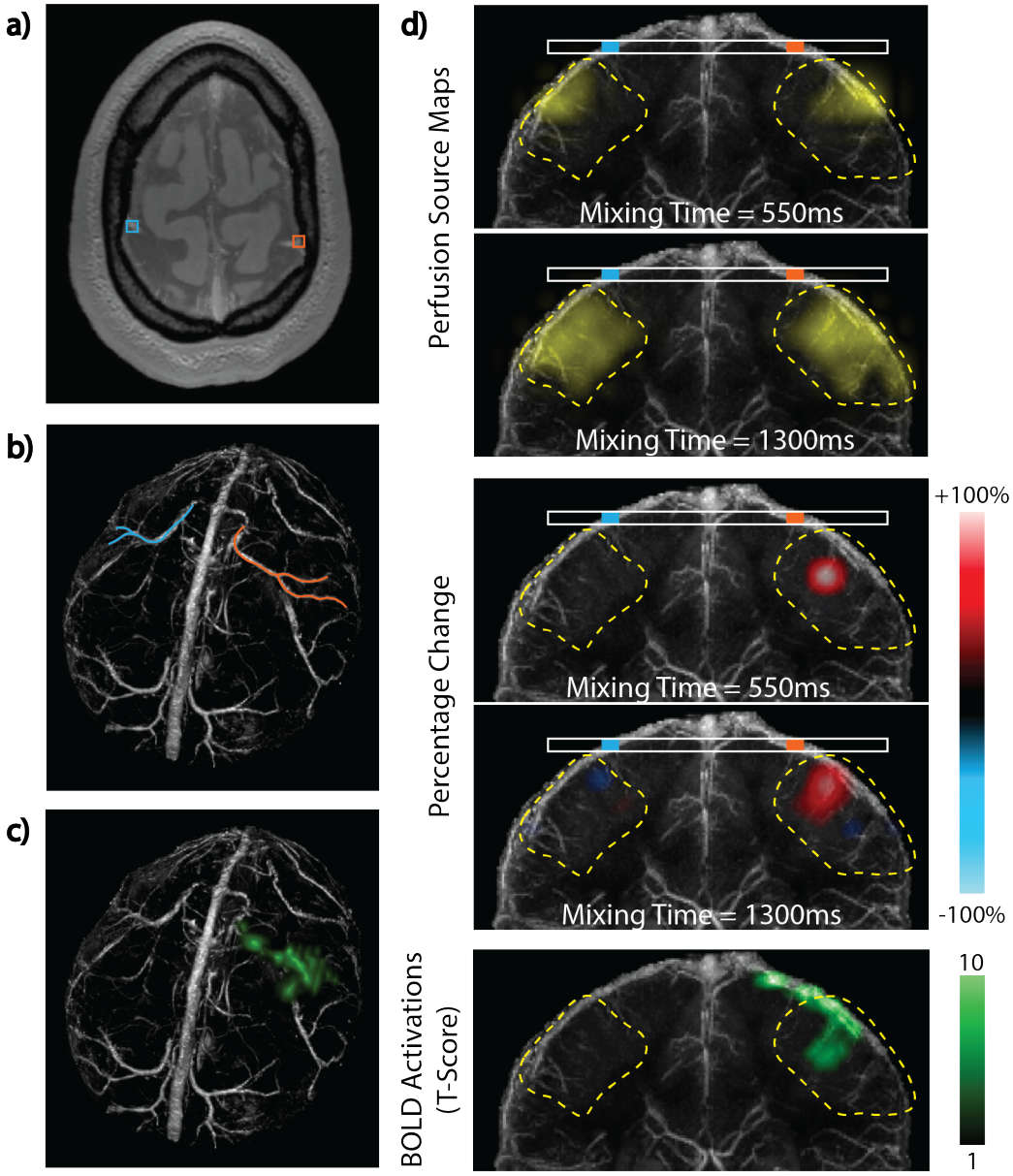

Figure 5.8: Left motor cortex activation in Subject 2. a) Imaging slice showing two selected veins: one (orange) drains the activated left motor cortex and one (blue) is selected as control. b) The color-coded veins overlaid on a 3D QSM-venogram. c) BOLD activations (green) overlaid on the 3D QSM-venogram. d) **Top:** Perfusion source image for activated and control veins at two mixing times. **Middle:** The percentage change showing positive local changes near the BOLD activated regions. **Bottom:** BOLD activation map for the coronal sections containing each vein. Venous territories are marked with yellow dashed lines.

and baseline perfusion source maps at mixing times of 550 and 1150ms are displayed in Figure 5.8d.

In both subjects, there is a large local signal increase in the perfusion source maps for the veins that drain the activated motor cortices. Notably, this increase was observed in the regions of the venous territory close to the BOLD activation, while other regions of the territory exhibited minimal or no modulation. Subject 1 also exhibited a significant local decrease in perfusion in the right motor cortex, located slightly further away from the BOLD activated region. The blood source maps of the control veins in both subjects showed little or no percent change between baseline and task.

Repeatability and ROI Analysis

Next, I investigated the repeatability of the observed modulations. To illustrate repeatability, I show the percentage change in perfusion source maps for the vein draining the same activated motor cortex from two scans. For Subject 1, I chose the vein draining the right motor cortex (Figure 5.9), while for Subject 2, I selected the vein draining the left motor cortex (Figure 5.10). For Subject 1, positive perfusion changes are observed repeatably close to the focal site of BOLD activation while negative perfusion changes are observed slightly further away. For Subject 2, positive perfusion changes are observed in both scans near the focal site of BOLD activation.

To investigate the repeatability of observed modulations in more detail, ROIs were selected from venous territories, their source signal amplitude was normalized by the maximum amplitude and displayed at task and baseline. Two ROIs were selected from the right motor cortex of Subject 1 (Figure 5.11). The first ROI, near the focal site of BOLD activation, showed an increase in source signal amplitude for both scans, while the second ROI slightly further away consistently showed a decrease in signal amplitude.

For Subject 2, two ROIs were selected from the left motor cortex as shown in Figure 5.12. In this case, the first ROI near the focal site of BOLD activation consistently showed an increase in source signal amplitude, whereas, the second ROI showed no change.

Statistical Analysis of Perfusion Source Maps

To assess the consistency of observed modulations, t-tests were conducted on the initial scan data from each subject, comparing the mixing time source signal series at baseline and during task at every source location in the perfusion source maps. The t-statistic images with a significance threshold of $p < 0.05$ are displayed in Figure 5.13, highlighting the venous territory regions exhibiting significant perfusion modulation during task relative to baseline. For Subject 1 with bilateral motor cortex activation, both veins drain activated motor cortices, therefore, significant perfusion modulations are observed in both veins. In contrast, for Subject 2 where only one vein drains the activated left motor cortex, significant perfusion modulations are observed unilaterally.

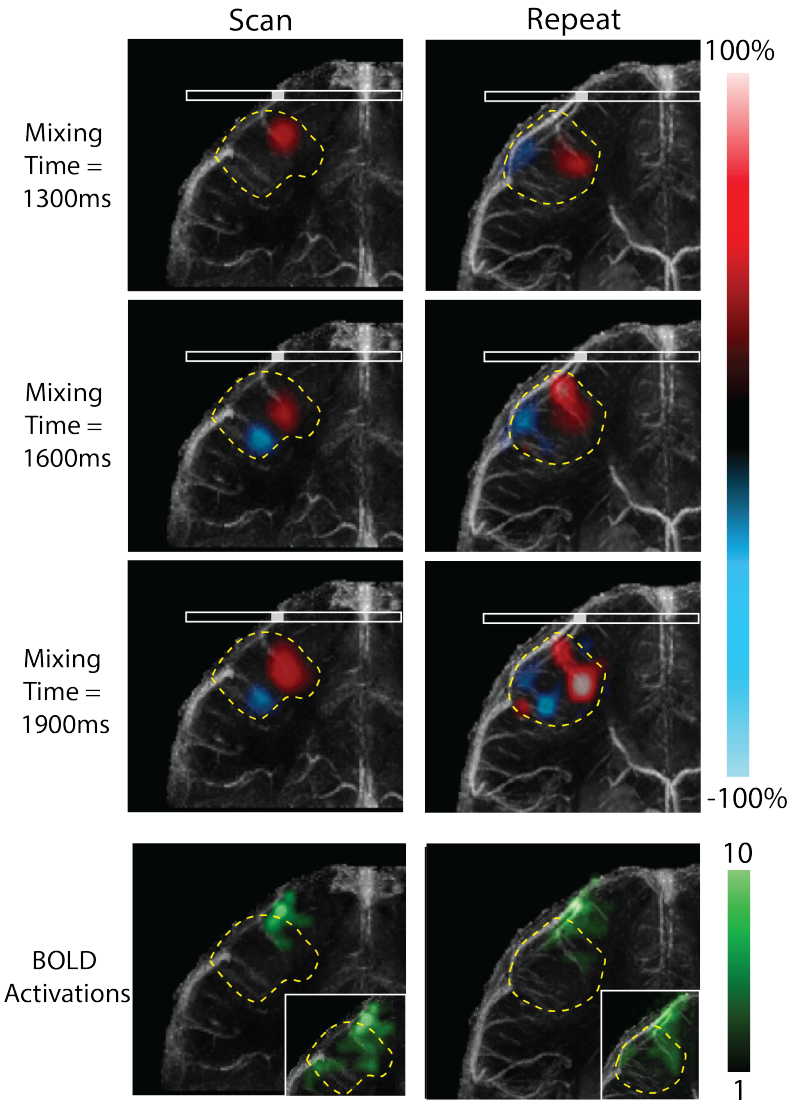

Figure 5.9: Repeatability analysis for Subject 1. Percentage change in perfusion source maps at three mixing times for the vein draining the right motor cortex shown for the initial and repeat scans. BOLD activations (green) of the coronal section containing the vein are shown as a reference on the bottom. To visualize functionally activated regions in more detail, the BOLD activations are shown with a higher significance threshold on the right bottom corner. The initial and repeat scans show good overlap, in regions that exhibit positive and negative percentage change. Note that the scans were performed on different sessions leading to some differences in the head orientation and imaging slice position. Venous territories are marked with yellow dashed lines.

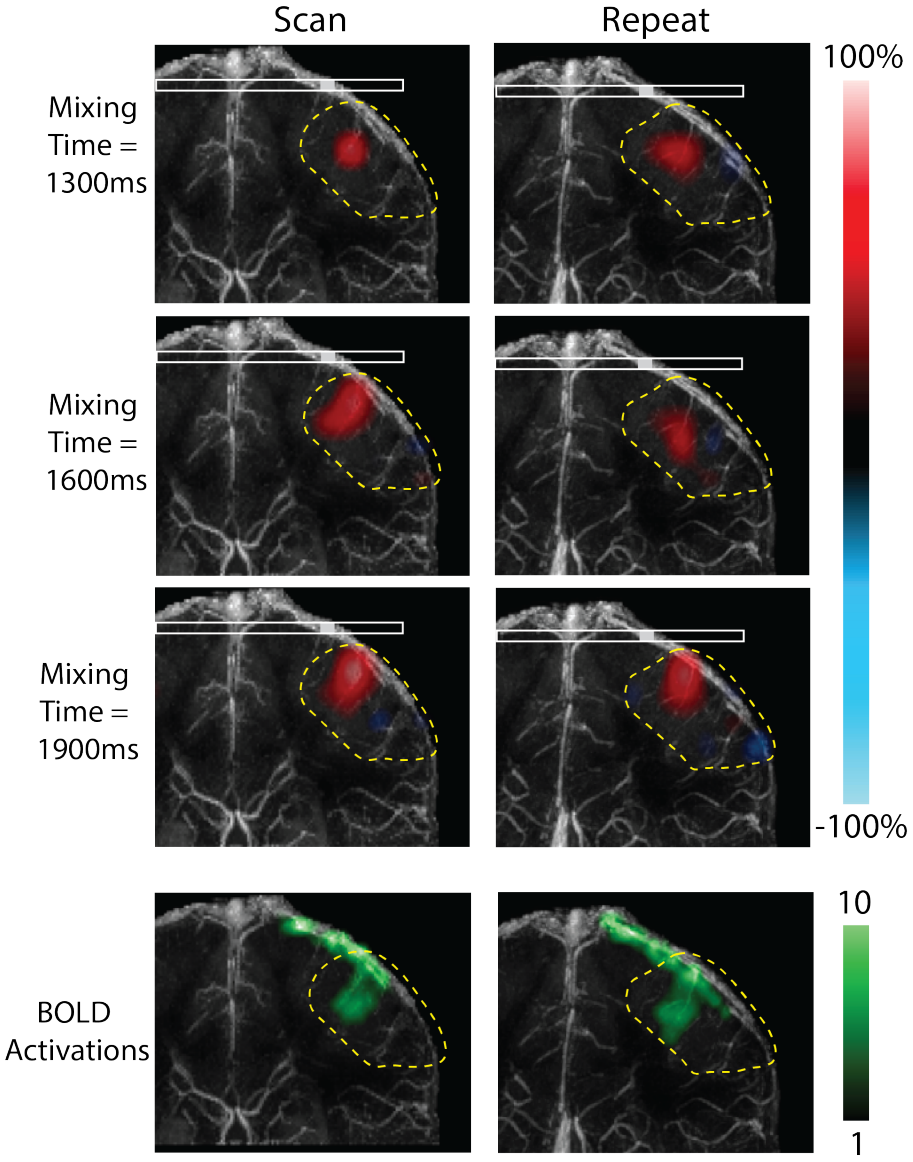

Figure 5.10: Repeatability analysis for Subject 2. Percentage change in perfusion source maps at three mixing times for the vein draining the left motor cortex shown for the initial and repeat scans. BOLD activations (green) of the coronal section containing the vein are shown as a reference on the bottom. The initial and repeat scans show good overlap, in regions that exhibit positive percentage change. Note that the scans were performed on different sessions leading to some differences in the head orientation and imaging slice position. Venous territories are marked with yellow dashed lines.

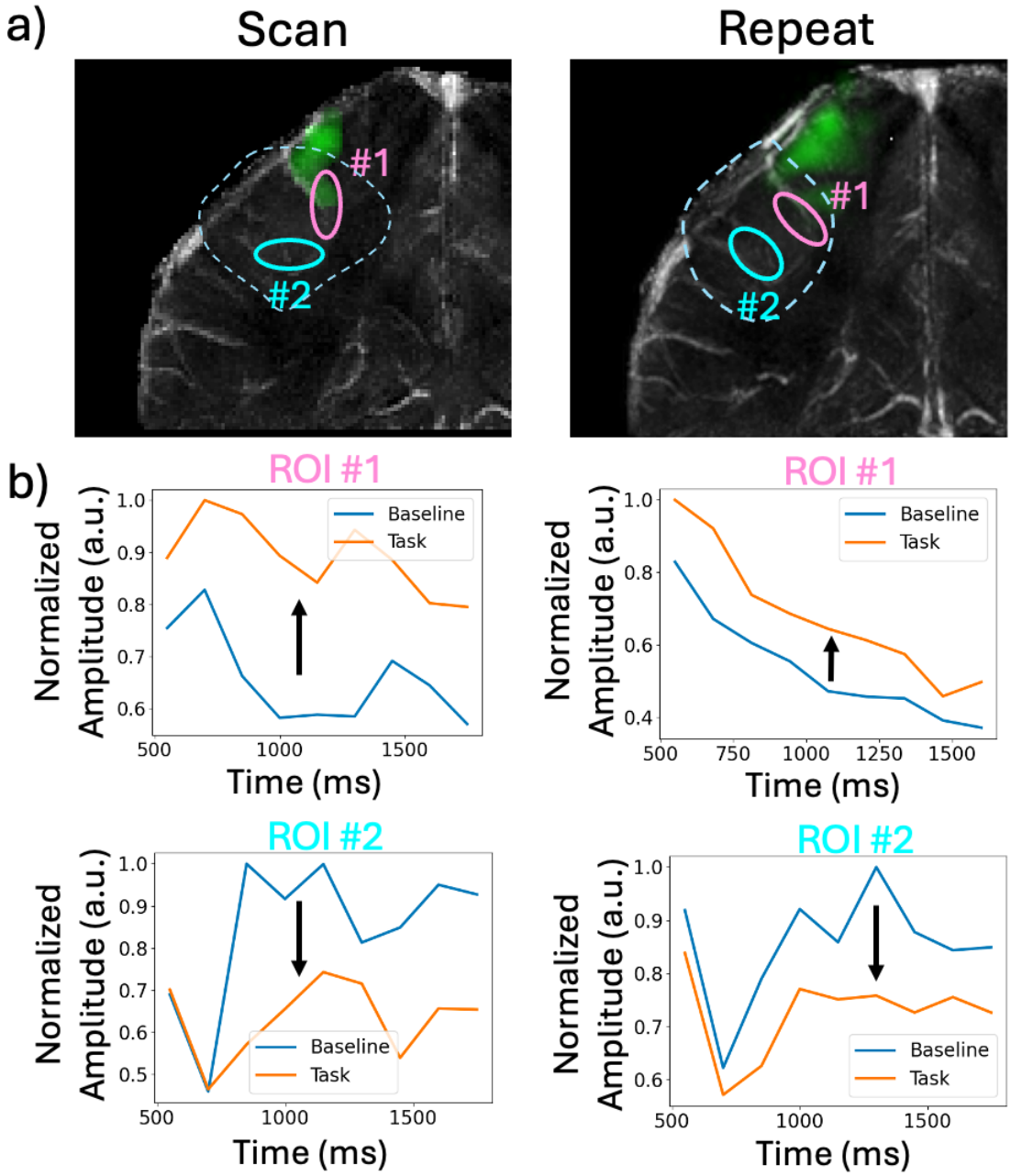

Figure 5.11: ROI analysis for Subject 1. a) BOLD activations (green) of the coronal section containing the vein draining the right motor cortex. b) Two ROIs are selected from the venous territory and their normalized perfusion source map amplitude during task (orange) and at baseline (blue) are shown across mixing times for the first scan and repeat scan. The first ROI shows consistent increase in source signal amplitude while the second ROI shows consistent decrease.

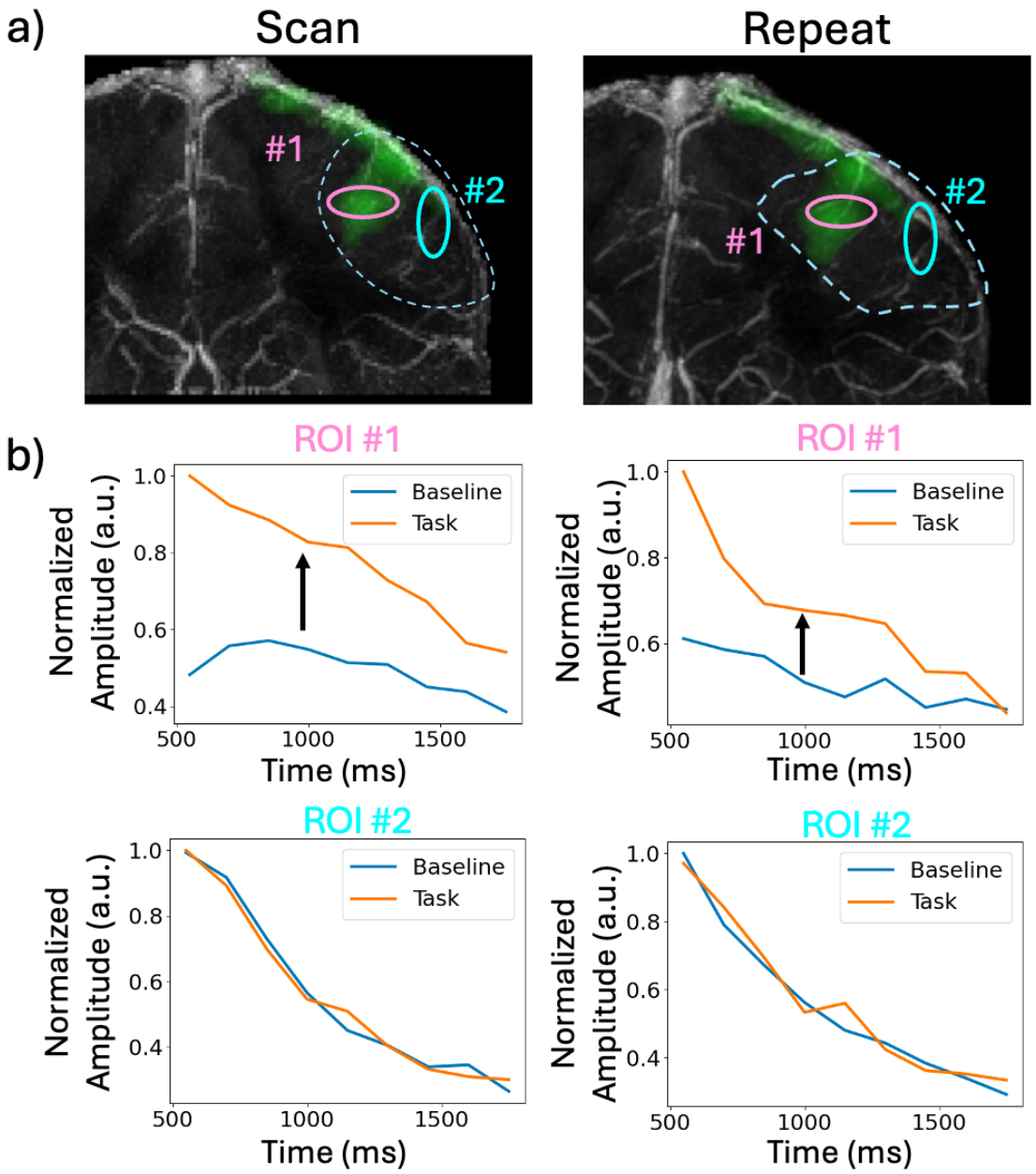

Figure 5.12: ROI analysis for Subject 2. a) BOLD activations (green) of the coronal section containing the vein draining the left motor cortex. b) Two ROIs are selected from the venous territory and their normalized perfusion source map amplitude during task (orange) and at baseline (blue) are shown across mixing times for the first scan and repeat scan. The first ROI shows consistent increase in source signal amplitude while the second ROI shows no change.

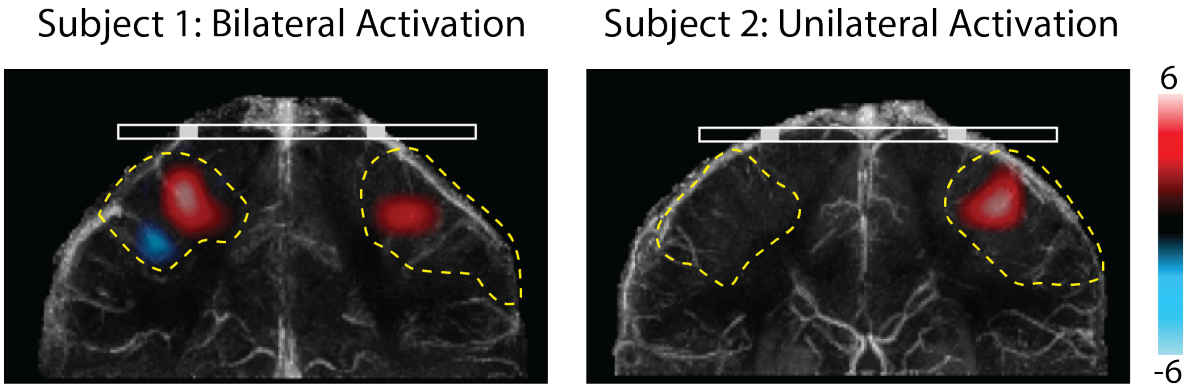

Figure 5.13: DiSpect T-test results for Subject 1 with bilateral activation (left) and Subject 2 with unilateral left motor cortex activation (right). For Subject 1 with bilateral activation, regions with significant changes in perfusion source signal amplitude are identified in veins draining both motor cortices, whereas for Subject 2, significant changes are only identified in the vein draining the left motor cortex.

Spiral BOLD fMRI

In order to demonstrate that the motor cortices are getting consistently activated across the DiSpect scans, I analyzed the data collected during the Spiral-BOLD acquisitions performed at the beginning of each partition. I selected three ROIs within the functionally activated regions (Figure 5.14a). Next, I display the signal from the custom Spiral-BOLD acquisitions for each selected ROI (Figure 5.14b). The red markers indicate the last Spiral-BOLD acquisition during task and the green markers indicate the last acquisition during rest. The plotted signal amplitudes indicate that all ROIs exhibit consistent activation throughout the scan as anticipated.

5.4 Discussion

In the previous chapter, I showed that DiSpect can be used to trace perfusion sources of different cerebral veins. In addition to its ability to trace venous perfusion sources dynamically, perfusion source mapping also exhibits sensitivity to global changes in blood flow due to caffeine. The perfusion source maps revealed a delayed arrival of blood to the imaging slice after caffeine intake. The delayed arrival was observed consistently for different veins as well as across different source locations within each venous territory. Interestingly, the delay in arrival time was longer towards the boundaries of the venous territories, further from the imaging slice, compared to regions closer to the imaging slice (Figure 5.2e). This

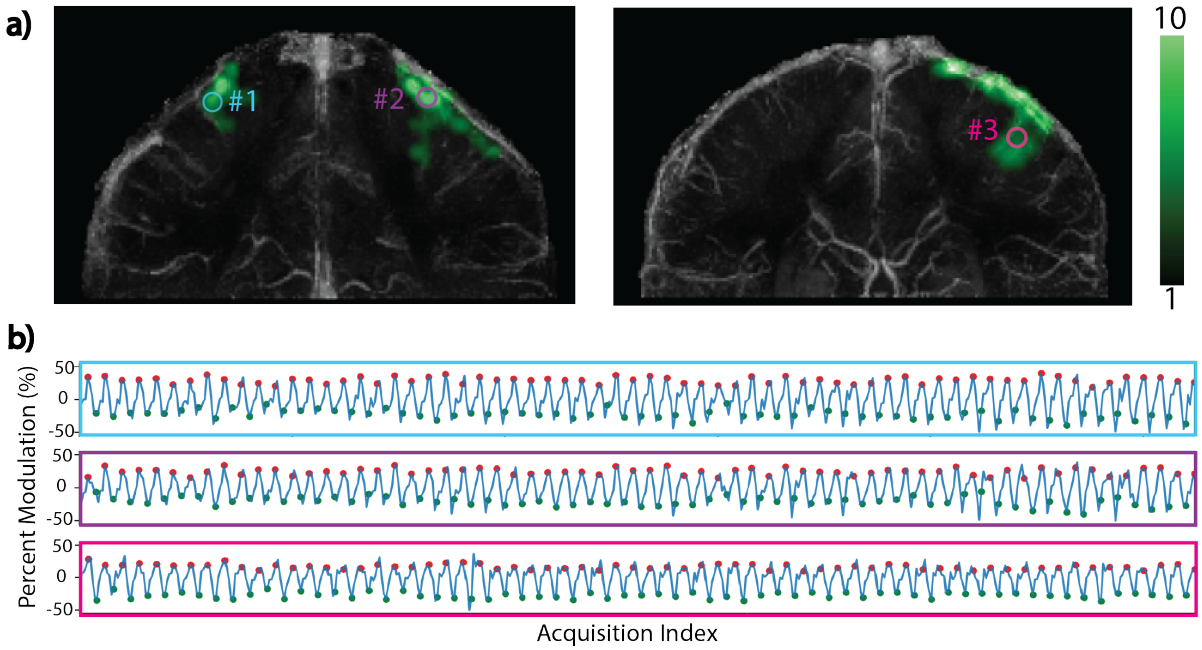

Figure 5.14: Analysis of Spiral BOLD acquisitions at the beginning of DiSpect partitions for the first scan of each subject. a) EPI BOLD activations for the coronal sections containing veins draining left and right motor cortices of each subject. Three ROIs are selected on the activated regions determined by the commercial BOLD acquisition. b) The percent modulation for each ROI measured by the custom Spiral-BOLD performed at each DiSpect partition is displayed across the entire acquisition. Red markers indicate the last Spiral-BOLD acquisition performed during task and green markers indicate the last Spiral-BOLD acquisition performed during rest. All three regions exhibit consistent activation throughout the scan.

difference may be attributed to two factors. First, since it takes longer for blood to arrive from the boundaries, the absolute change in arrival time could be larger, even though the relative change is similar. Second, there could be effects due to the projection along the AP direction, which might be more pronounced near the edges where the veins branch out more.

DiSpect also shows specificity to detecting local changes in venous perfusion during a motor cortex activation task. In this case, local changes are observed only in the territories of veins that drain functionally activated regions. Remarkably, even though imaging is performed at a location downstream of the activated area, the perfusion source maps can be used to discern the blood within the imaged volume originating from an activated region upstream. The modulations within the territories are mainly located in the vicinity of BOLD

activated regions, however, they are not identical to the BOLD activation. This is because the perfusion source maps and BOLD signals are inherently different. The perfusion source maps provide dynamic information on the amount of blood that drains into an image voxel from a particular source location. In contrast, BOLD measures blood oxygenation changes mainly due to modulations in blood flow and volume. BOLD contrast is affected by arteries, capillaries and veins whereas the perfusion source maps are solely sensitive to capillaries and veins. Another difference is that the DiSpect acquisitions were performed at a lower resolution (6-8mm) compared to the BOLD resolution of 3mm.

In general, an increase in source signal amplitude is observed during task near sites of neural activation. Interestingly, near the right motor cortex of Subject 1, I observed positive changes in DiSpect signal near the focal site of activation, while observing significant negative changes in some veins slightly further away. This observation was consistent across two repeated scans, with the negative changes observed in the vicinity of less statistically significant positive BOLD activations. Previous literature has reported negative changes in venous blood volume during activation when using hyperoxia as a contrast agent, observed in regions with positive changes in BOLD signal [81]. I hypothesize that the negative changes in source signal amplitude could be a result of the redistribution of venous blood volume from neighboring regions to the activated area. It is known that the arterial blood volume increases as a result of neural activation, potentially leading to a compensatory decrease in blood volume in nearby cerebral regions because the brain is a closed system. Further investigation involving additional subjects need to be conducted to comprehensively understand and characterize this behavior.

For the repeatability analysis, the two scans were performed during different scan sessions for both subjects, resulting in differences in head orientation. Consequently, due to this orientation mismatch, the percentage change maps were not identical. Nevertheless, the regions of the venous territory with large perfusion modulation show significant overlap, supporting the claim that DiSpect can repeatably detect modulations in venous perfusion due to neural activation. The repeatability of the results were also confirmed by performing an ROI analysis and observing that for all ROIs the source signal change was in the same direction for both scans.

The main limitation of the functional DiSpect acquisitions is that the scan time is long due to the need to acquire perfusion source maps during task and at baseline. I use the custom Spiral-BOLD acquisitions performed at the beginning of each DiSpect partition to confirm that the motor cortices were getting activated consistently across this long scan. However, any motion between different displacement encodings could cause inconsistencies and corrupt the perfusion source maps. To mitigate this issue, future work includes investigating prospective motion correction methods.

The ability of the perfusion source maps to detect changes in venous perfusion during functional activation can contribute to a better understanding of venous contributions to the BOLD signal, thereby eliminate any mis-localization of functional activation and enhance its spatial specificity. Furthermore, it could allow for a better understanding of the complex biophysics that regulate venous blood flow during functional activation.

5.5 Conclusion

In this chapter, I verify the sensitivity of the perfusion source mapping method to detecting global perfusion changes with a caffeine study. I further establish its specificity by showing that this method can consistently and repeatably detect local perfusion changes due to the neural activation of the motor cortices. Remarkably, even though imaging is performed at a location downstream of the neural activation, the method can discern the blood within the imaged volume that originates from a activated region upstream.

Chapter 6

Advances in Venous Perfusion Source Mapping

6.1 Introduction

In the previous two chapters, I have described venous perfusion source mapping and established its sensitivity and specificity. In this chapter, I will show some advancements and additional validations of the method. To this end, I will start by presenting two flow phantom studies. In the first study, I further validate our method by comparing the perfusion source maps to flow particle trajectories simulated from a 4D flow acquisition in a phantom mimicking the superior cerebral veins. For the second study, I designed a phantom to mimic a dural arteriovenous fistula (DAVF) and show that the perfusion source maps can potentially be used to distinguish between a high risk and low risk fistula in a simplified setting.

Following this, I show several advancements in acquisition techniques. This will include performing multi-slice imaging after tagging in order to dynamically trace the perfusion of multiple vein groups simultaneously and demonstrating 3D displacement encoding in a scenario where the perfusion sources are limited to smaller regions.

6.2 Methods

Flow Phantom to Simulate the Superior Cerebral Veins

Flow Phantom Design and Experimental Setup

A flow phantom was designed to mimic the superior cerebral veins (Figure 6.1). The phantom design was 3D printed using a Formlabs Form 3 Printer (Somerville, Massachusetts). The phantom had four sets of tubes merging at the top. It was placed inside a water pool and a continuous peristaltic pump was used to draw water out of the tubes (Figure 6.1a). As water is drawn out from the top of the tubes, more water gets pulled from the water pool

into the tubes. Throughout the experiment, water is continuously fed back into the main pool. The water being fed back to the main pool cause some local turbulent flow in that area. To avoid this turbulent flow from affecting the image quality, walls are placed around the phantom.

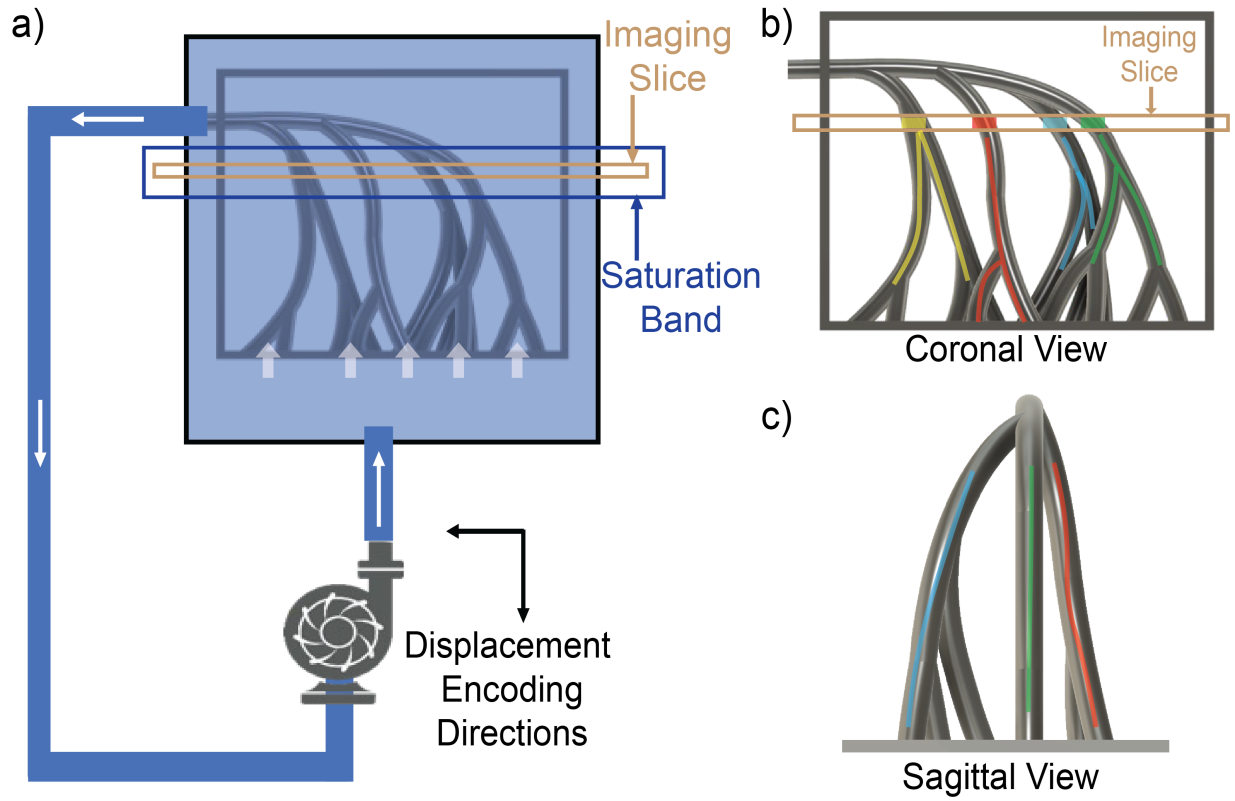

Figure 6.1: Setup for flow phantom experiment mimicking the superior cerebral veins. a) A phantom is constructed and 3D printed to mimic the superior cerebral veins. The phantom is placed in a large pool and a peristaltic pump is used to draw water out of the tubes. As water is drawn out, more water gets drawn into the tubes from the main pool (as shown by the white arrows). The placement of the imaging slice and spatial saturation band for the DiSpect acquisition are shown. b) Coronal and c) Sagittal View of the phantom marking four sets of tubes in different colors. Tubes shown in each color carry flow into a different location within the imaging slice.

Acquisition Parameters

A DiSpect acquisition is performed with 2D coronal displacement encoding and an axial imaging slice (Figures 6.1a-b). A 20mm thick saturation band was placed around the imaging

slice to suppress signal from static water spins. The acquisition was performed with a TR of $6s$. The target image resolution for the acquisition was $4 \times 4\text{mm}^2$ with a target FOV of $18 \times 18\text{cm}^2$ and slice thickness of 5mm. I used a source displacement resolution of $3 \times 3\text{mm}^2$ and the source FOV was $4.2 \times 5.4\text{cm}^2$. The overall scan duration was 75 minutes. Image acquisitions were performed repeatedly after tagging, acquiring displacement spectra at mixing times from $100ms$ to $5.8s$, in $150ms$ increments. Image voxels containing the four tubes were selected and their source maps were visualized.

For validation and comparison, the tubes were imaged with a 4D flow [82, 83] sequence. The acquisition was performed with a resolution of $1 \times 1 \times 1\text{mm}^3$, TE=$5.22ms$, TR=$35.63ms$, Flip Angle=$5^o$ and 2 repetitions. The velocity encoding was set to the smallest value of $v_{enc} = 5cm/s$. The overall scan duration was 30 minutes.

Flow Particle Trajectory Simulations

Particle trajectories were simulated from a velocity map obtained by the 4D flow acquisition using the Runge-Kutta integration method. These trajectories were simulated from 0 to 4.45 seconds in $10ms$ increments. To mitigate for any accumulated errors, Gaussian random noise with a variance of 0.1 cm/s was introduced at each time point to the velocity measurements. 50 trajectories with random noise were simulated for each location within the volume.

Next, source maps were simulated from the 4D flow particle trajectories. A region corresponding to the image voxel shown in yellow in Figure 6.1b was selected, and the number of trajectories arriving to this target voxel from each location within the volume were determined at different time points. These should correspond to the sources of simulated particles that arrive into the image voxel at different time points.

Flow Phantom to Simulate DAVFs

Risk Stratification of DAVFs

DAVFs are a potentially dangerous acquired vascular malformation in the brain where several arteries with high blood pressure directly connect to the typically low-pressure veins and can result in life threatening intracranial hemorrhage (ICH) [84–86]. Digital subtraction angiography (DSA), which is based on x-ray and contrast injection, remains the gold standard for diagnosis, determining the full angioarchitecture, and the only means for grading [87] the risk of the DAVF (Figure 6.2). There are three DAVF angiographic stages: no fistula, low risk DAVF and high risk DAVF. In the case where there is no fistula, cortical veins drain normally into the sinus. There are no connections from the arteries into the veins. When there is a low risk DAVF, arteries form direct connections into the veins, however, this direct connection does not cause the flow direction to reverse in the cortical veins. With a high risk DAVF, cortical flow reversal is observed, where blood from the arteries directly drain into the cortical veins, reversing the direction of blood flow.

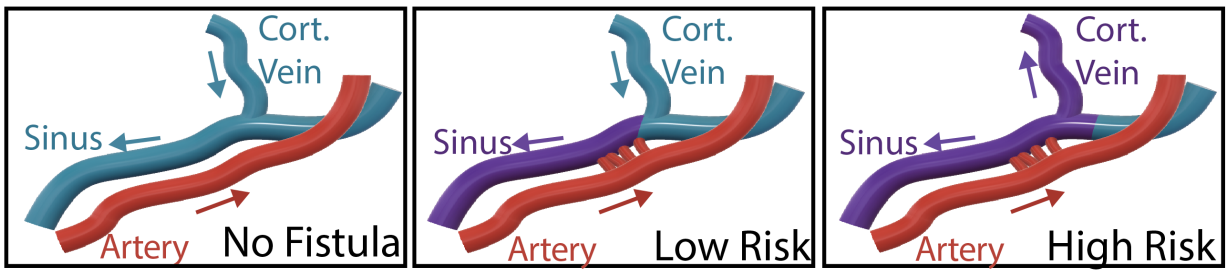

Figure 6.2: DAVF angiographic stages: no fistula, low risk DAVF and high risk DAVF. In the case where there is no fistula, cortical veins drain normally into the sinus. When there is a low risk DAVF, arteries form direct connections into the veins, however, there is no cortical flow reversal. With a high risk DAVF, cortical flow reversal is observed where blood from the arteries directly drain into the cortical veins, reversing the direction of blood flow.

Flow Phantom Design and Experimental Setup

To demonstrate the potential of DiSpect to risk stratify DAVFs, I performed another flow phantom experiment. A phantom was constructed to simulate a fistula located near a cortical vein and a sinus (Figure 6.3a). The designed phantom was printed using a Formlabs Form 3 Printer (Somerville, Massachusetts). The phantom was placed inside a large water pool. A continuous peristaltic pump was used to draw water out of the tubes. The pump was connected to the tubes in two configurations (Figure 6.3b). To simulate the low risk DAVFs, the pump only draws water from the sinus. In this case, the water should be pulled from the main pool into the fistula and cortical vein tubes and feed into the sinus. For the high risk scenario, the pump draws water from both the sinus and the cortical vein. Consequently, the water should be pulled from the water pool into the fistula and feed into both the sinus and cortical vein tubes, corresponding to a flow reversal in the cortical vein. It is important to note that this study is a simple proof of concept designed only to simulate the flow directions in the presence of fistulas with different angiographic stages but not the pressures that cause these changes in flow.

Acquisition Parameters

For the DiSpect acquisition, 2D coronal displacement encoding was performed with an axial imaging slice placed across the cortical vein and sinus tubes (Figure 6.3a). A 20mm thick saturation band was placed around the imaging slice to suppress signal from static water spins. The acquisition was performed with a TR of $3s$. The target image resolution for the acquisition was $4 \times 4\text{mm}^2$ with a target FOV of $16 \times 16\text{cm}^2$ and slice thickness of 5mm. I used a source displacement resolution of $4 \times 4\text{mm}^2$ and the source FOV was $5.6 \times 8.8\text{cm}^2$. Image acquisitions were performed repeatedly after tagging, acquiring displacement spectra at mixing times from $100ms$ to $2.8s$, in $150ms$ increments. Overall scan duration was 46

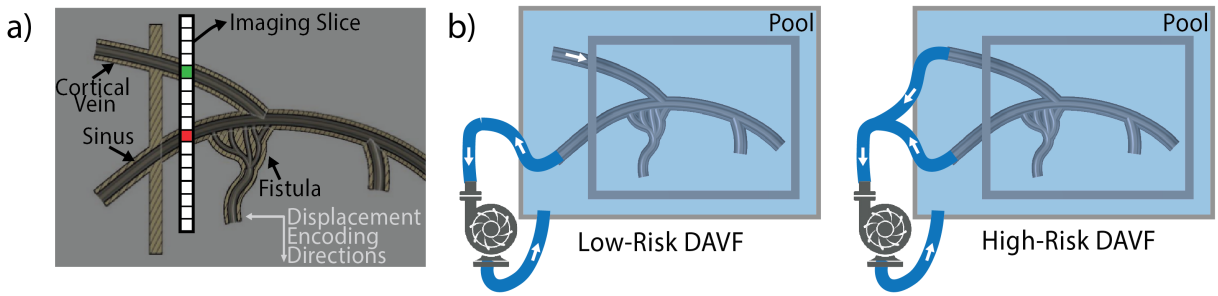

Figure 6.3: Flow phantom experiment to demonstrate the potential of DiSpect to risk-stratify DAVFs. a) The phantom was constructed to simulate flow in a cortical vein located near a DAVF. An imaging slice was positioned to cover the cortical vein and sinus. b) The pump was connected in two configurations to simulate low risk and high risk DAVFs.

minutes. Image voxels containing cortical vein and sinus tubes were selected and their source maps were visualized (Figure 6.3a).

Multi-Slice Imaging

In the previously reported experiments, only a single slice was imaged. Imaging multiple slices could be advantageous for tracing the sources of veins that drain into different regions of the brain, which cannot be covered using a single imaging plane. By leveraging the delay between repeated image acquisitions performed after tagging, an additional slice can be imaged without increasing the scan time.

In order to demonstrate this ability, an interleaved two slice DiSpect acquisition was developed to simultaneously image superior cerebral veins and deep cerebral veins. Two axial slices were chosen: one to image the superior cerebral veins and another to image the deep cerebral veins (Figure 6.4a-b). The target image resolutions for both slices were $4 \times 4\text{mm}^2$. A smaller target FOV of $16 \times 16\text{cm}^2$ was sufficient to cover the top slice while the bottom slice had a larger FOV of $22 \times 22\text{cm}^2$. At each of the repeated image acquisitions ($100ms$-$2.8s$, in $150ms$ increments), the two slices were imaged consecutively (Figure 6.4c). The DiSpect acquisition was performed with 2D sagittal displacement encoding with a source displacement resolution of $6 \times 6\text{mm}^2$ and a source FOV was $12 \times 7.2\text{cm}^2$. Overall scan duration was variable due to cardiac gating but was close to 36 minutes. Target image voxels containing different veins were selected and their source maps were visualized (Figure 6.4b).

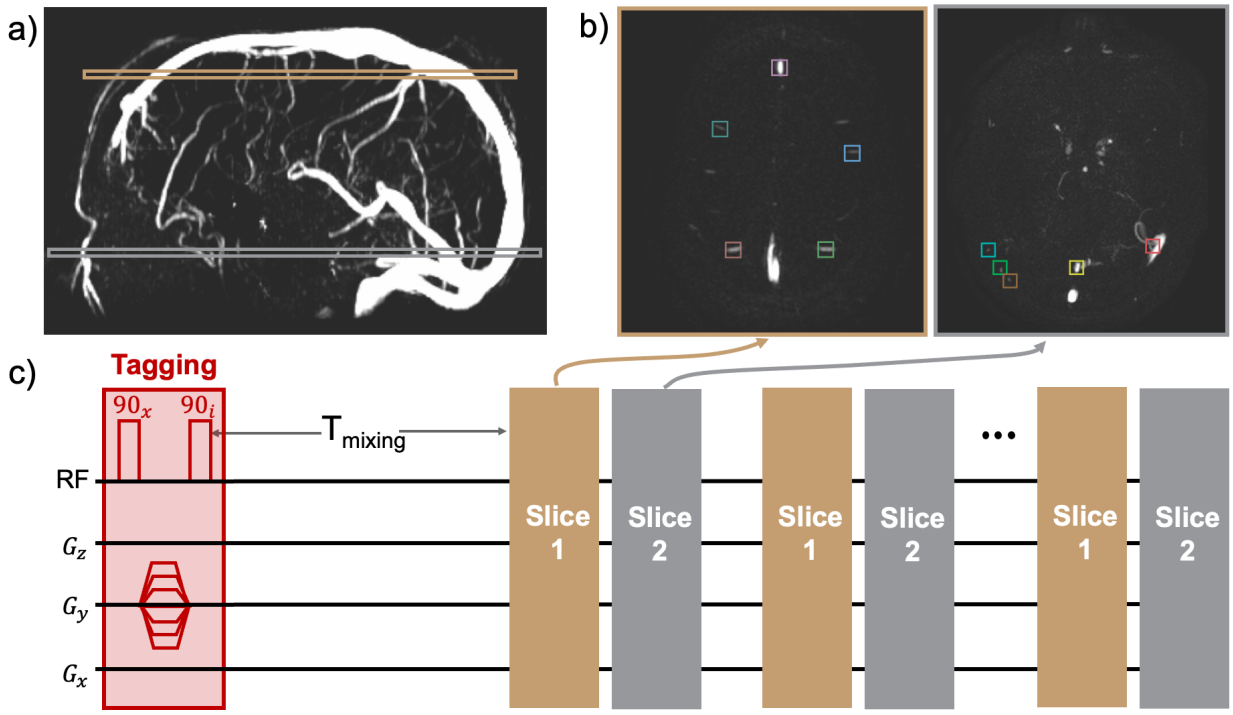

Figure 6.4: Setup for two-slice DiSpect acquisition. a) Two slices are selected to image the superior (top) and deep (bottom) cerebral veins. b) The two imaging slices with vein ROIs selected in different colors. c) Modified pulse sequence showing two slices acquired consecutively for each of the repeated image acquisitions after tagging.

3D Displacement Encoding

All previously reported experiments were performed with 2D displacement encoding due to acquisition time considerations. However, information gets projected along the third dimension, which can obscure important perfusion dynamics for certain anatomies. Here, I demonstrate that acquiring 3D displacement spectra within a reasonable acquisition time is feasible when the sources entering a target voxel come from a smaller region, allowing a smaller displacement FOV to be prescribed. In this scenario, instead of sampling the displacement k-space with a large FOV in 2D, a similar number of points are sampled in 3D with a smaller FOV. For this experiment, an axial imaging slice was placed to intersect the superior sagittal sinus and superior veins at a lower position of the head (Figure 6.5a). Consequently, the sources of each superior vein in the imaging slice will come from a smaller FOV below it.

For the DiSpect acquisition the target axial image resolution was $4 \times 4\text{mm}^2$ with a target FOV of $18 \times 18\text{cm}^2$. 3D displacement encoding with a source displacement resolution of $6 \times 6 \times 6\text{mm}^3$ and a source FOV of $3.6 \times 3.6 \times 3.6\text{cm}^3$ was performed. Image acquisitions

were performed repeatedly after tagging, acquiring displacement spectra at mixing times from 100ms to 2.8s, in 150ms increments. Overall scan duration was variable due to cardiac gating but was close to 32 minutes. Target image voxels containing three different veins were selected and their source maps were visualized in 3D (Figure 6.5b).

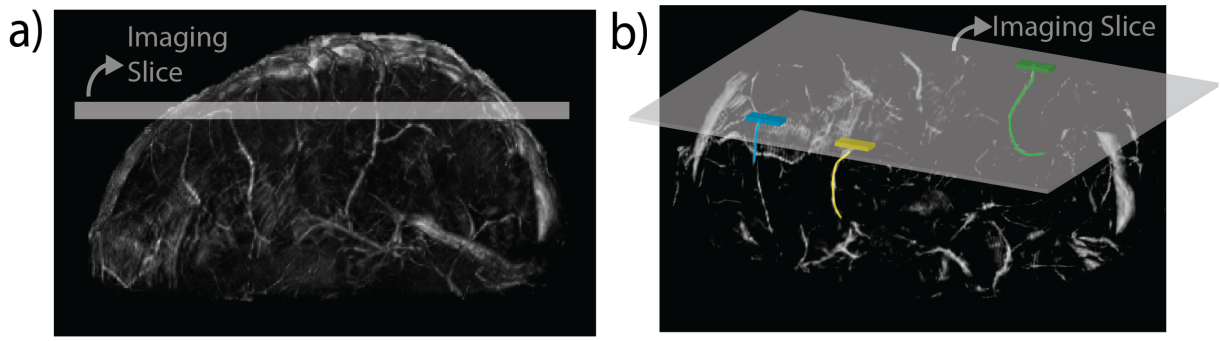

Figure 6.5: 3D displacement encoding. a) A sagittal projection of the 3D QSM-venogram showing the axial imaging slice placed lower down in the head. b) Three target vein ROIs are selected from the imaging slice and shown in different colors. The sources of each vein ROI will come from a smaller region below it.

6.3 Results

Flow Phantom to Simulate the Superior Cerebral Veins

The source maps for image voxels containing the four tubes are overlaid on the CAD model of the tubes for mixing times of 1300ms, 2800ms and 4300ms in Figure 6.6. For the tubes with slower flows (green and blue) the source maps show water coming from within the tubes. On the other hand, for the faster flowing tubes (yellow and red) water comes from within the tubes as well as from the main pool. The source maps can be clearly visualized for a very long evolution time of 4.3s.

A coronal slice of the velocity maps in the z and x directions obtained from the 4D flow acquisition are displayed for one section of tubes in Figure 6.7a. The measured velocities are shown for the range between -3 and 3 cm/s. Example 4D flow particle trajectories simulated from regions selected towards the bottom of the tubes are shown in Figure 6.7b. Due to accumulated errors throughout the trajectory, only some of the simulated particles reach the top of the tubes.

The source maps simulated from the particle trajectories are compared to the source maps acquired with DiSpect at four mixing times in Figure 6.7c. The source maps show

good overlap for the shorter mixing times (1000ms and 1600ms), however, for the longer mixing times (2200ms and 2800ms) there are discrepancies as pointed out by the red arrows.

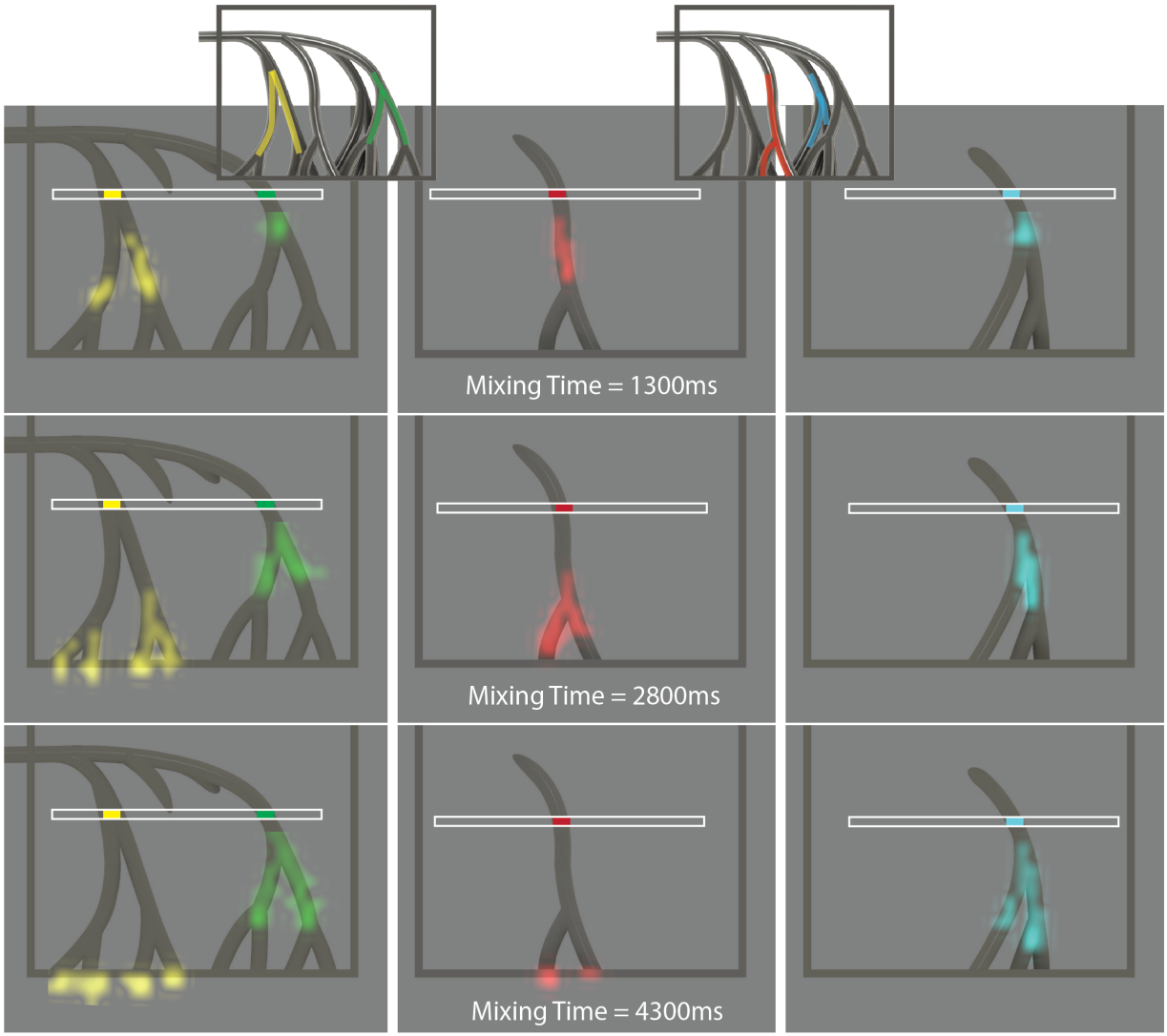

Figure 6.6: Results for flow phantom mimicking the superior veins. The source maps for image voxels containing the four tubes are shown for mixing times of 1300ms, 2800ms and 4300ms. For the tubes with slower flows (green and blue) the source maps show water coming from within the tubes, while for the faster flowing tubes (yellow and red) water comes from within the tubes as well as from the main water pool.

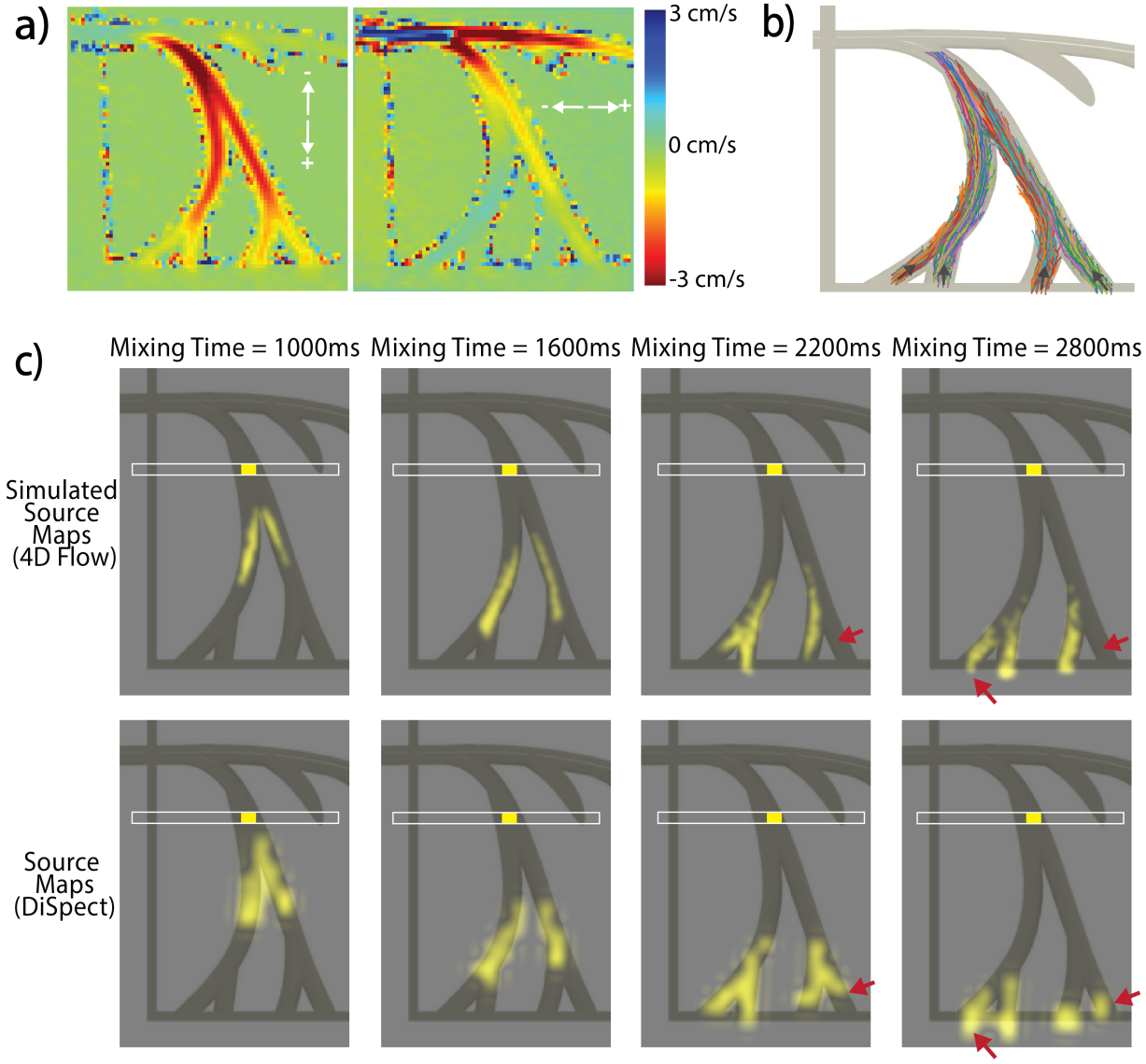

Figure 6.7: Results of particle trajectory simulations from the 4D flow acquisitions. a) A coronal slice of the velocity maps in the z (left) and x (right) directions for one set of tubes. The measured velocities are shown for the range between -3 and 3 cm/s. b) Example particle trajectories simulated from regions selected towards the bottom of the tubes. c) A comparison between the **Top:** simulated source maps from the particle trajectories and **Bottom:** measured source maps from DiSpect. While the measured and simulated source maps show good overlap for the shorter mixing times, there are several discrepancies at the longer mixing times as shown by the red arrows. The simulated source maps from the 4D flow acquisition completely miss water coming from one region of the tubes.

Flow Phantom to Simulate DAVFs

The results of the flow phantom simulating DAVFs are shown in Figure 6.8. The source maps for the image voxels containing cortical vein and sinus tubes are overlaid on the CAD model of the tubes for low risk and high risk configurations at mixing times of $400ms$, $700ms$ and $1000ms$. For the low risk scenario, the source maps show that the water in the cortical vein tube comes from the outer water pool (green), while the water in the sinus tube comes from the fistula as well as the cortical vein (red). In the high risk scenario, the source maps depict that water in both the sinus and the cortical vein tubes come from the fistula. For the high risk DAVF configuration, the source maps can also identify the different arterial branches of the DAVF that feed the sinus (left three branches) and the cortical vein (right two branches).

Multi-Slice Imaging

For the two-slice acquisition, five vein ROIs are selected from each of the imaging slices. The perfusion source maps for each vein ROI in the top (Figure 6.9) and bottom (Figure 6.10) slice are overlaid on the sagittal projection of the PC-venogram for the section covering the corresponding vein. For the top slice five superior vein ROIs are selected and their source maps are displayed. For the bottom slice, one ROI (yellow) is placed on the straight sinus and the other four ROIs are placed on various smaller cortical veins. The acquisition is able to simultaneously image perfusion source maps in the superior and deep cerebral veins enabling more brain coverage. Similar to previous single slice results, at the initial mixing times sources of perfusion are more focal, whereas at longer mixing times they are more dispersed and farther from the imaging slice. By imaging the second slice during the dead time between image acquisitions, both slices can be acquired without an increase in the scan time.

3D Displacement Encoding

For each selected target vein ROI, 3D perfusion source maps at a mixing time of $1200ms$ are overlaid on the 3D QSM-venogram (Figure 6.11). 3D displacement encoding provides the ability to visualize perfusion sources in different orientations. Consequently, each of the perfusion source maps are shown at two orientations for each target vein ROI. The corresponding orientation marker for each case is also displayed. The ability to visualize different orientations can provide more flexibility. Veins can branch out in multiple directions, and visualizing a 2D projection from just one angle might not give a complete picture. For example, for the results of the green vein ROI displayed on the left in Figure 6.11, the top orientation shows a long branch extending sideways in the lower part of the vein. However, this long branch gets obscured due to projection when visualizing it from the bottom orientation. Even though an orientation may be ideal for visualizing the dynamics

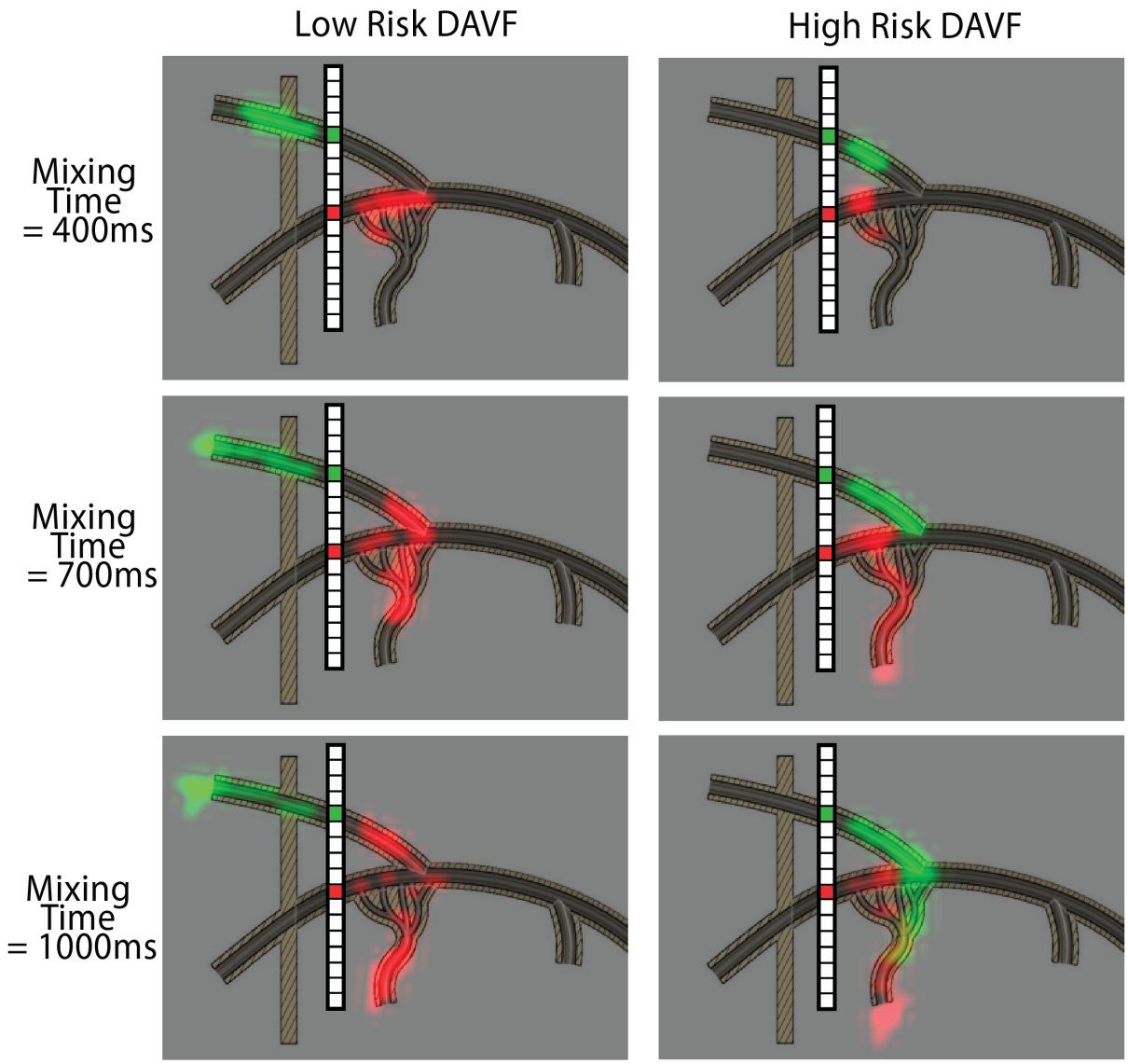

Figure 6.8: Results for the flow phantom simulating **left:** low risk and **right:** high risk DAVFs. The source maps for the image voxels containing cortical vein and sinus tubes are shown for low risk and high risk configurations at three mixing times. For the low risk scenario (left) source maps show that water in the cortical vein comes from upstream venous flow whereas for the high risk scenario (right) source maps show water coming from the fistula.

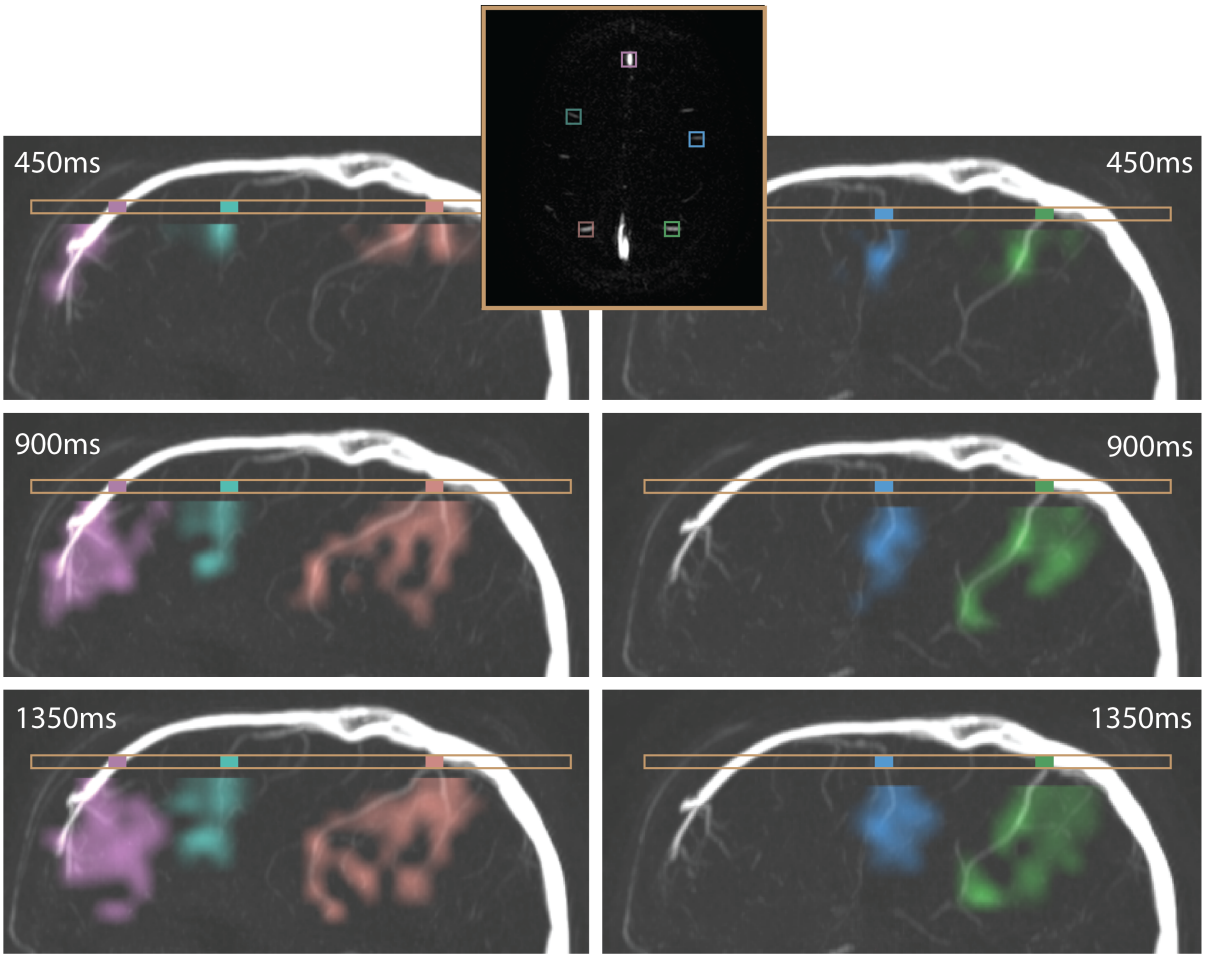

Figure 6.9: Perfusion source maps for five vein ROIs selected from the **top** slice of the two-slice acquisition are overlaid on the corresponding sagittal section of the PC venogram. The maps are shown at mixing times of $450ms$, $900ms$ and $1350ms$ in the corresponding colors. The imaging slice with the selected vein ROIs is shown at the top as a reference.

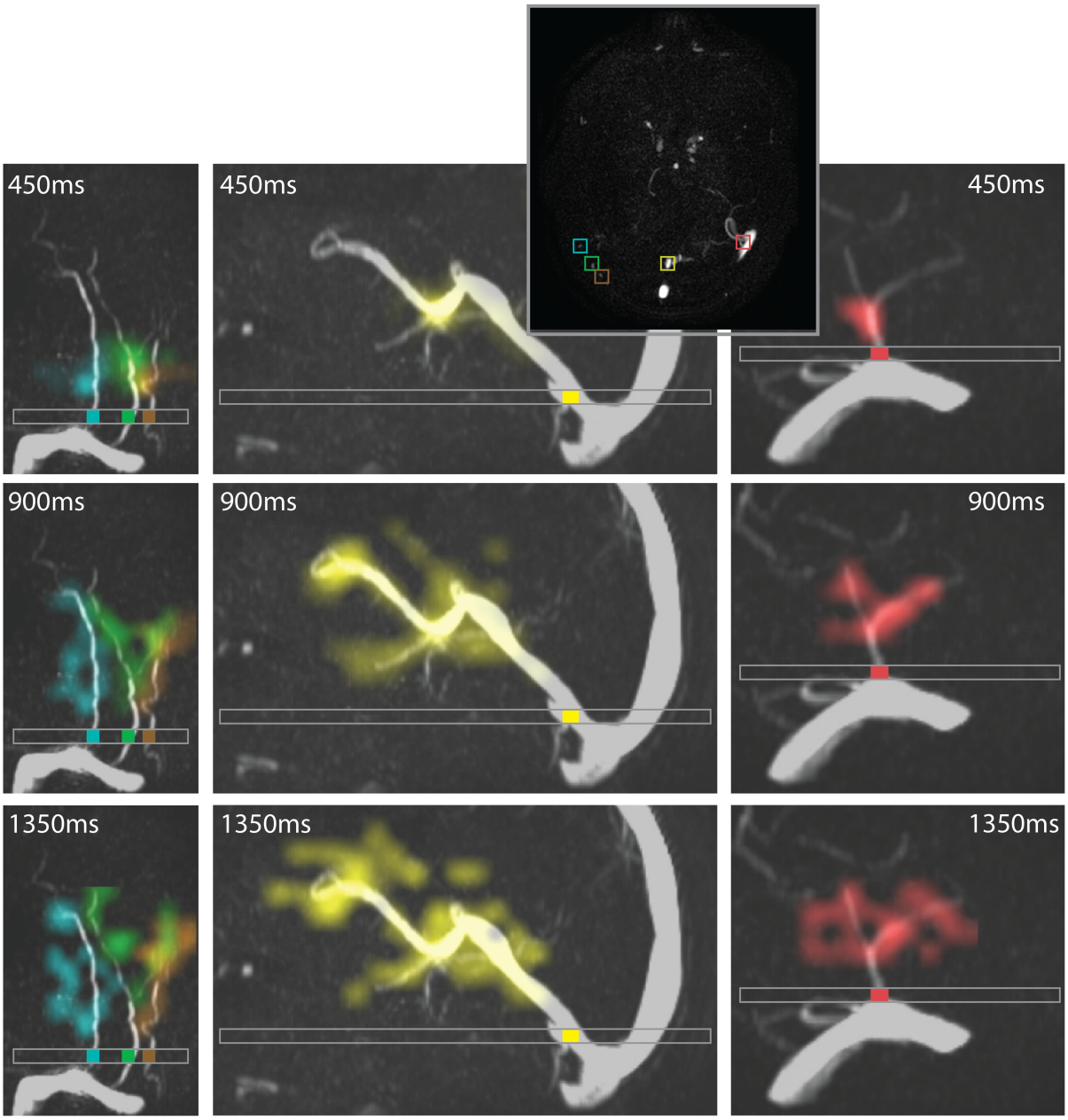

Figure 6.10: Perfusion source maps for five vein ROIs selected from the **bottom** slice of the two-slice acquisition are overlaid on the corresponding sagittal section of the PC venogram. The maps are shown at mixing times of $450ms$, $900ms$ and $1350ms$ in the corresponding colors. The imaging slice with the selected vein ROIs is shown at the top as a reference.

of one superior vein, a different orientation could be more suitable for seeing the details of another vein.

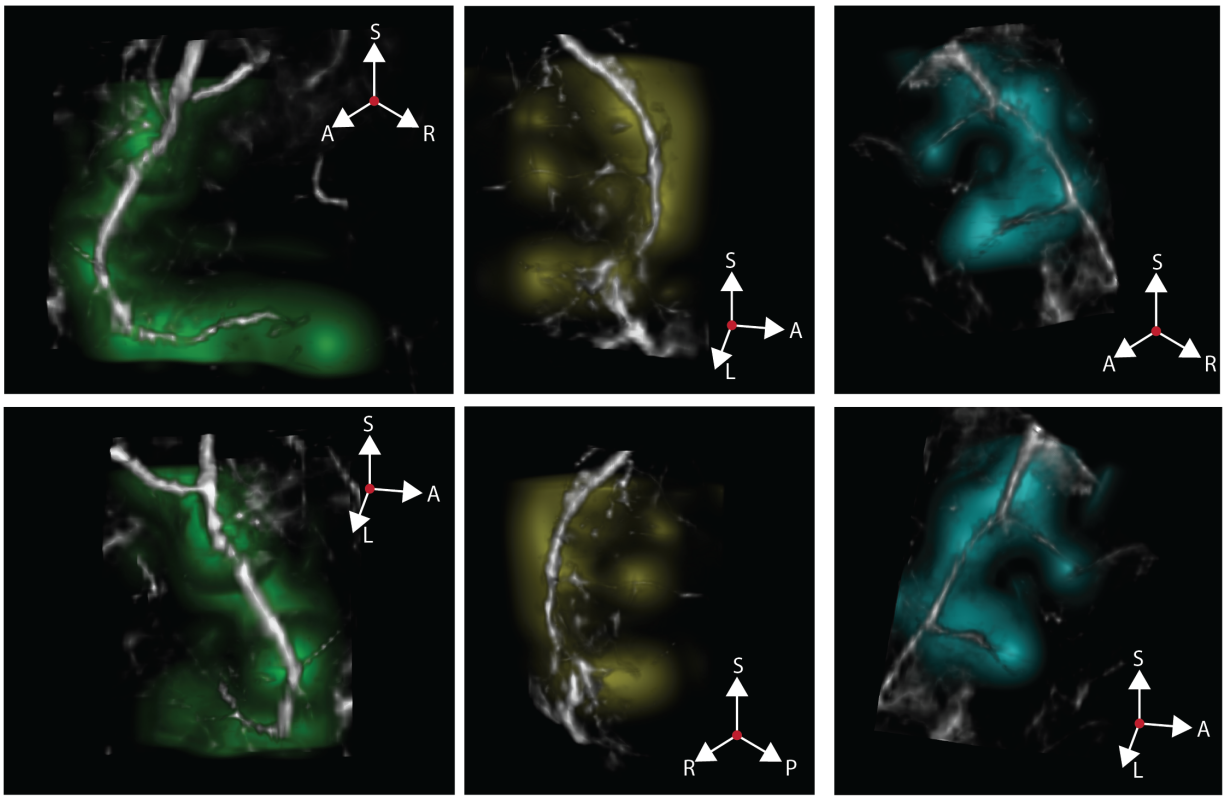

Figure 6.11: 3D perfusion source maps at a mixing time of 1200ms overlaid on a 3D QSM-venogram. The source maps are shown at two orientations for each vein. The orientation of each image is depicted with the corresponding orientation marker.

6.4 Discussion

In this chapter, I have presented results from two flow phantom experiments to further validate this method and demonstrate its potential to be used in a clinical application. Furthermore, I present two advancements to the DiSpect acquisition including multi-slice imaging and 3D displacement encoding.

For the first flow phantom study, I show that the source maps obtained from DiSpect can trace water flowing in a set of tubes mimicking the superior cerebral veins. The source maps can be used to trace the water flowing within the tubes as well as water coming from the main pool into the tubes. Remarkably, the source maps can be clearly visualized even at a very

long evolution time of $4.3s$. In contrast, for the in-vivo experiments, the perfusion source maps become dominated by noise at earlier evolution times. One reason for this difference could be that water has a longer T_1 compared to blood, increasing the signal at longer mixing times. Another reason could be the fact that the flow phantom study was not impacted by any physiological noise, for example, cardiac pulsatility, which could be corrupting in-vivo datasets. During in-vivo acquisitions, although the tagging is cardiac triggered, repeated image acquisitions are performed for several seconds after tagging, where additional cardiac cycles occur. These additional cardiac cycles could happen at different times after tagging for different displacement encodings, resulting in inconsistencies in the acquired data and leading to physiological noise.

When comparing the source maps measured with DiSpect to those simulated from 4D flow particle trajectories, there was good overlap at the shorter mixing times, validating the method. However, at the longer mixing times there were some discrepancies. For example, water sources arriving from one section of the tubes is completely missed in the simulated source maps (depicted by red arrows in Figure 6.7c). In addition, the simulated source maps only show water coming from within the tubes, while the measured source maps show water arriving to the imaging slice from the main pool. These discrepancies could be due to the fact that at longer mixing times errors in the simulated particle trajectories accumulate, resulting in larger deviations. Additionally, near the bottom of the tubes, the measured velocities are smaller and may be more affected by noise.

The second phantom study showed the potential of the source maps to risk-stratify DAVFs. When the flow phantom was connected in low risk and high risk configurations, the source maps were able to correctly identify the presence of flow reversal in the cortical vein. Furthermore, when both the cortical vein and sinus were fed by the fistula, the source maps were able to resolve a complex flow scenario where two right small arteries in the fistula feed the cortical vein, while the three left ones feed the sinus. This demonstrates the potential of the method to not only risk-stratify DAVFs but also to correctly resolve the arteries that feed them, which is highly important for treatment planning. Nevertheless, the flow phantom represented a very simplified version of DAVF anatomy. The setup only mimicked high risk and low risk DAVFs by altering how the tubes are routed. A more advanced setup could simulate the pressure changes that lead to these flow variations, providing a more realistic model for in-vivo DAVFs. In order to translate this method into the clinic, more realistic models are necessary to further optimize the acquisition parameters and imaging geometries.

In the two-slice acquisition I demonstrate the ability to simultaneously image superior and deep cerebral veins. This gives an opportunity to measure perfusion dynamics of a higher number of veins without increasing the total acquisition time. It is also possible to increase the number of slices to cover even more vein groups. However, prescribing too many slices could constrain the temporal resolution of the consecutive image acquisitions. In this case, simultaneous multi-slice imaging strategies can be implemented for the ability to image more slices without any reduction in temporal resolution [88]. When placing multiple imaging slices, it is important to consider the geometry of the imaged veins. If positioned incorrectly, one imaging slice could saturate the sources of blood draining into another slice.

Finally, in the 3D DiSpect acquisition, I show the ability to resolve 3D perfusion source maps in a case where blood sources are limited to small regions. For this experiment, the displacement FOV was limited to a smaller region by changing the placement of the imaging slice. However, in cases where this cannot be achieved solely by moving the position of the imaging slice, it is also possible to add spatial saturation bands to suppress sources coming from particular regions or use selective excitation during tagging to limit the sources to a certain region. One limitation with this acquisition is that the imaging slice was placed lower down in the head, where physiological noise due to pulsatility of the static brain tissue is stronger. Due to this fact, the perfusion source maps show more artifacts after $1.2s$ evolution time, which approximately corresponds to the timing of the second heart beat. Reducing physiological noise by periodically saturating signal from static tissue or detecting and accounting for the additional cardiac cycles is an area of future work.

6.5 Conclusion

In this chapter, I validated the perfusion source mapping method and demonstrated its clinical potential through two flow phantom experiments. The first experiment showed that this method can trace water flow in tubes mimicking cerebral veins, producing clear source maps even at long evolution times. When compared with source maps obtained from 4D flow simulations, our measured source maps showed good overlap at shorter times but discrepancies at longer times. These discrepancies were mainly due to limitations of the simulated particle trajectories from the 4D flow acquisition. The second flow phantom experiment demonstrated the ability of the perfusion source maps to risk-stratify DAVFs. Additionally, advancements in DiSpect acquisition, such as multi-slice imaging and 3D displacement encoding, were presented. Multi-slice imaging allows for simultaneous imaging of more veins without extending acquisition time, while 3D encoding can resolve the perfusion source maps in different orientations.

Chapter 7

Conclusions and Future Work

7.1 Summary of Contributions

In this dissertation, I presented a new MRI method, venous perfusion source mapping, targeted to probe the dynamics of venous blood flow. This novel method employs DiSpect, a highly versatile technique for measuring complex tissue dynamics that uses blood water as an endogenous contrast agent. DiSpect performs multiple DENSE acquisitions with increasing displacement encodings to resolve the multi-dimensional map of sources that enter each image voxel during the evolution time between tagging and imaging.

In venous perfusion source mapping with DiSpect, spatial information is encoded into the magnetization of blood water spins across the entire brain during tagging and remotely detected once the tagged blood reaches the imaging region – often near the brain's surface, where the signal-to-noise ratio is 3-4× higher. DiSpect can resolve the sources of blood water entering the imaging slice across short to long evolution times, effectively capturing venous perfusion sources in reverse. Blood sources can be traced regardless of their path and velocity, allowing the measurement of both faster blood flow in the sinuses and slower flow in smaller veins and capillary beds in a single acquisition. Additionally, by placing the imaging slice on large veins where blood is quickly refreshed, blood sources can be probed through repeated imaging without disturbing perfusion. Through experiments, I show that venous perfusion source mapping can be used to trace the sources of blood in individual superior veins as shown in Figure 7.1.

In order to establish the sensitivity and specificity of venous perfusion source mapping, a series of experiments were conducted. First, the sensitivity of the method to global changes in venous perfusion was demonstrated using a caffeine study. After the consumption of caffeine, an increase in arrival times to the imaging slice was measured with the source maps globally across venous territories. Next, the specificity of the method to local perfusion changes was shown during functional activation. These local perfusion changes were detected consistently and repeatably in the vicinity of BOLD activated regions. Remarkably, even though imaging was performed at a location downstream of the neural activation, the perfusion source maps

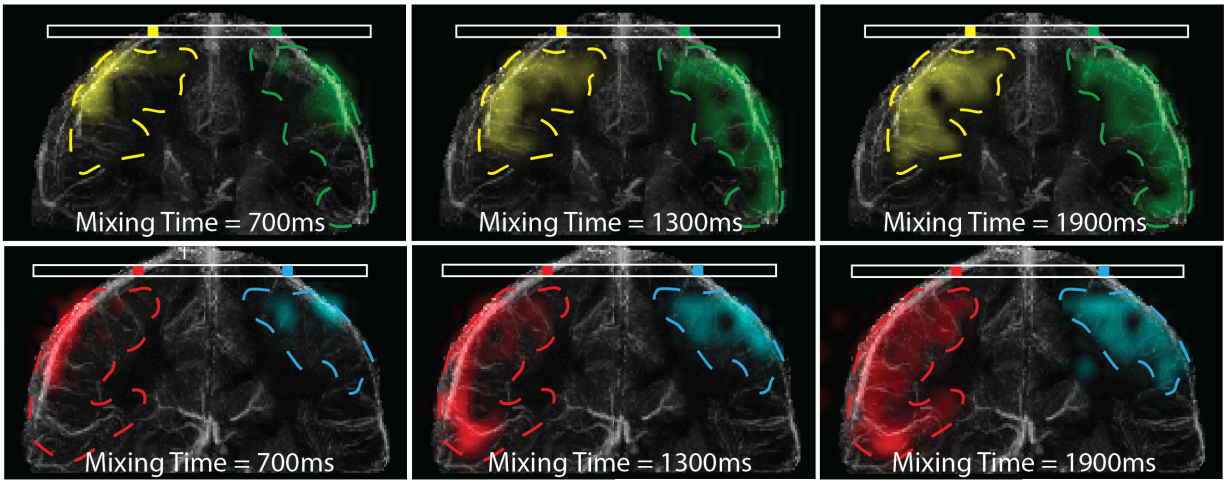

Figure 7.1: The perfusion source maps for four superior veins shown at different evolution times demonstrating the ability to trace the sources of blood in individual veins.

can be used to discern the blood within the imaged volume that originates from an activated region upstream.

Additional validations and advancements of venous perfusion source mapping were presented with flow phantom and in-vivo experiments. A flow phantom was constructed to mimic the superior veins and used to compare the measured source maps to flow particle trajectories simulated from a 4D flow acquisition. The measured and simulated source maps showed good overlap for shorter evolution times. At longer evolution times, the measured maps were able to reveal sources that the simulated maps missed. A second flow phantom was designed to simulate a DAVF and the source maps obtained from low risk and high risk configurations of the DAVF phantom were able to correctly detect the presence of cortical vein flow reversal. In addition, the source maps contained information to identify the arteries feeding the fistula, which could also be useful for treatment planning.

Following this, several advancements in acquisition techniques were shown. This included performing multi-slice imaging after tagging in order to dynamically trace the perfusion of multiple vein groups simultaneously and demonstrating 3D displacement encoding in a scenario where the perfusion sources are limited to smaller regions. These different acquisition strategies can be employed to tailor the method to different applications.

7.2 Suggestions for Future Work

In this dissertation I have demonstrated a novel method to image venous blood flow and validated it with several experiments. Despite the progress, there are several additional

challenges and opportunities for future work. This section summarizes some of these potential directions.

Acceleration

Currently, one of the main limitations of the DiSpect is that the acquisition is slow. The displacement k-space is sampled point-by-point resulting in typical scan times on the order of 20-40 minutes for 2D displacement encoding (depending on the resolution and FOV). This hinders the ability of this technique to be translated into clinical practice, especially in pediatric applications. However, the perfusion source maps are highly sparse and since flow is continuous they also exhibit much spatial/temporal redundancy. In addition, the sources of blood are constrained by the venous anatomy. Future work could accelerate acquisitions by using partial Fourier or variable density sampling, and a regularized reconstruction [64–66]. For example, low-rank regularization has been successfully used for diffusion MRI [89, 90] and for DCE MRI [91–93]. The regularization could also be learned from acquired data, similar to how dictionary learning is applied for the reconstruction of undersampled diffusion spectrum imaging [94].

Another potential method to accelerate DiSpect acquisitions is to extract the displacement echo from a reduced number of phase cycles. This can be achieved by leveraging prior knowledge about the T_1 echo and the conjugate displacement echo. Since the T_1 echo is unaffected by displacement, the T_1 echoes at different displacement encodings share mutual information. Furthermore, as the displacement encoding gradients increase, the conjugate echo moves out of the imaged field of view, making its removal unnecessary. Undersampling in phase cycling can be combined with undersampling of the displacement k-space to further accelerate acquisitions.

Artifact Reduction

The SNR of the perfusion source maps decreases at longer evolution times due to the T_1 decay of blood water between tagging and imaging. Additionally, physiological noise, particularly from the pulsatility of static brain tissue, becomes more significant at longer mixing times as additional cardiac cycles occur between tagging and imaging. This combination of physiological noise and reduced SNR diminishes the fidelity of perfusion source maps at longer mixing times. To obtain high-quality source maps under these conditions, reducing physiological noise is essential. One potential approach is to periodically saturate the signal from static tissue by performing repeated image acquisitions at a higher temporal resolution or using inversion pulses to null the signal from static tissue. Another approach could be to detect and account for variability in the timing of the second or potentially third cardiac cycles that occur after tagging.

Motion during the scan can also pose a problem, especially for acquisitions with longer scan times. Retrospective motion correction is challenging in the case of 2D displacement encodings, as the perfusion source maps will be projected along different directions depending

on the head's orientation. Prospective motion correction strategies can be employed by adjusting gradient and RF waveforms to compensate for the observed motion. Volume navigators can be inserted during the dead time right before tagging and be used to detect motion [95].

Visualization

The visualization of the perfusion source maps is another direction for improvement. Currently a coronal projection of the QSM-venogram is used to visualize the venous anatomy of each cerebral vein. The perfusion source maps are overlaid on this coronal projection of the QSM-venogram. However, this method is simplistic and may include contributions from neighboring veins. More advanced vessel segmentation techniques could be employed to isolate the structure of each vein [96, 97]. This process can be automated to detect veins in the target imaging slice and overlay their perfusion source maps on the segmented structure of each vein.

Potential Applications

Perfusion source mapping with DiSpect could open new avenues for imaging various cerebral diseases and enhancing the understanding of different pathophysiologies. For example, it could facilitate the evaluation of arteriovenous malformations (AVMs), where arteries and veins form abnormal, complex connections [69]. I have demonstrated that this method can distinguish between high risk and low risk DAVFs, which are a type of AVMs, using a flow phantom experiment. Venous perfusion source mapping could also provide insights into changes in blood flow and volume due to developmental venous anomalies (DVAs). While DVAs are generally asymptomatic, they can occasionally become symptomatic. Perfusion source mapping can be used to investigate the relationship between venous congestion and the risk of developing symptomatic DVAs [98].

DiSpect also holds potential in investigating collateral circulation in ischemic stroke, particularly in cases involving complex vascular bypass networks within the venous drainage system [70]. This tool could also assist in performing hemodynamic analysis of cerebral aneurysms to assess risk [71].

In recent years, there has been significant interest in investigating the body's and brain's clearance mechanisms, called the lymphatic and glymphatic systems [99]. Since perfusion source maps can track blood sources regardless of velocity, it could be useful for measuring the very slow lymphatic and glymphatic flows. For this application, the acquisition can be adapted, for example, by using T_2 preparation pulses to selectively measure these flows.

Bibliography

[1] D Le Bihan. "Diffusion/perfusion MR imaging of the brain: from structure to function." In: *Radiology* 177.2 (1990), pp. 328–329.

[2] David T Wymer et al. "Phase-contrast MRI: physics, techniques, and clinical applications". In: *Radiographics* 40.1 (2020), pp. 122–140.

[3] Jonathan H Gillard, Adam D Waldman, and Peter B Barker. *Clinical MR neuroimaging: diffusion, perfusion and spectroscopy*. Cambridge University Press, 2004.

[4] Steven P Sourbron and David L Buckley. "Classic models for dynamic contrast-enhanced MRI". In: *NMR in Biomedicine* 26.8 (2013), pp. 1004–1027.

[5] Hannu J Aronen and Jussi Perkiö. "Dynamic susceptibility contrast MRI of gliomas". In: *Neuroimaging Clinics* 12.4 (2002), pp. 501–523.

[6] Bernd Jung and Michael Markl. "Phase-contrast MRI and flow quantification". In: *Magnetic Resonance Angiography: Principles and Applications*. Springer, 2011, pp. 51–64.

[7] David C Alsop et al. "Recommended implementation of arterial spin-labeled perfusion MRI for clinical applications: a consensus of the ISMRM perfusion study group and the European consortium for ASL in dementia". In: *Magnetic Resonance in Medicine* 73.1 (2015), pp. 102–116.

[8] Eric C Wong. "Vessel-encoded arterial spin-labeling using pseudocontinuous tagging". In: *Magnetic Resonance in Medicine: An Official Journal of the International Society for Magnetic Resonance in Medicine* 58.6 (2007), pp. 1086–1091.

[9] Souraya Stoquart-ElSankari et al. "A phase-contrast MRI study of physiologic cerebral venous flow". In: *Journal of Cerebral Blood Flow & Metabolism* 29.6 (2009), pp. 1208–1215.

[10] Lu Liu et al. "Anatomy imaging and hemodynamics research on the cerebral vein and venous sinus among individuals without cranial sinus and jugular vein diseases". In: *Frontiers in Neuroscience* 16 (2022), p. 999134.

[11] Roya Behrouzi and Martin Punter. "Diagnosis and management of cerebral venous thrombosis". In: *Clinical Medicine* 18.1 (2018), p. 75.

[12] Xi Chen et al. "Overview of multimodal MRI of intracranial Dural arteriovenous fistulas". In: *Journal of Interventional Medicine* 5.4 (2022), pp. 173–179.

[13] Maysa A Ridha et al. "Magnetic resonance imaging findings of elevated intracranial pressure in cerebral venous thrombosis versus idiopathic intracranial hypertension with transverse sinus stenosis". In: *Neuro-Ophthalmology* 37.1 (2013), pp. 1–6.

[14] Eleuterio F Toro. "Brain venous haemodynamics, neurological diseases and mathematical modelling. A review". In: *Applied Mathematics and Computation* 272 (2016), pp. 542–579.

[15] Clive B Beggs. "Venous hemodynamics in neurological disorders: an analytical review with hydrodynamic analysis". In: *BMC Medicine* 11 (2013), pp. 1–17.

[16] Sorin Tuță. "Cerebral venous outflow implications in idiopathic intracranial hypertension—from physiopathology to treatment". In: *Life* 12.6 (2022), p. 854.

[17] Cheryl A Olman, Souheil Inati, and David J Heeger. "The effect of large veins on spatial localization with GE BOLD at 3 T: Displacement, not blurring". In: *Neuroimage* 34.3 (2007), pp. 1126–1135.

[18] Jonathan R Polimeni et al. "Laminar analysis of 7 T BOLD using an imposed spatial activation pattern in human V1". In: *Neuroimage* 52.4 (2010), pp. 1334–1346.

[19] Kendrick Kay et al. "A critical assessment of data quality and venous effects in ultra-high-resolution fMRI". In: *BioRxiv* (2018), p. 337667.

[20] Kendrick Kay et al. "A temporal decomposition method for identifying venous effects in task-based fMRI". In: *Nature Methods* 17.10 (2020), pp. 1033–1039.

[21] Dheeraj Gandhi et al. "Intracranial dural arteriovenous fistulas: classification, imaging findings, and treatment". In: *American Journal of Neuroradiology* 33.6 (2012), pp. 1007–1013.

[22] Jean-Claude Sadik et al. "Imaging of cerebral venous thrombosis". In: *Life* 12.8 (2022), p. 1215.

[23] Stephen J Riederer et al. "Recent advances in 3D time-resolved contrast-enhanced MR angiography". In: *Journal of Magnetic Resonance Imaging* 42.1 (2015), pp. 3–22.

[24] RH Ayanzen et al. "Cerebral MR venography: normal anatomy and potential diagnostic pitfalls". In: *American Journal of Neuroradiology* 21.1 (2000), pp. 74–78.

[25] Alasdair G Morgan et al. "4D flow MRI for non-invasive measurement of blood flow in the brain: a systematic review". In: *Journal of Cerebral Blood Flow & Metabolism* 41.2 (2021), pp. 206–218.

[26] Ramona Lorenz et al. "Influence of eddy current, Maxwell and gradient field corrections on 3D flow visualization of 3D CINE PC-MRI data". In: *Magnetic Resonance in Medicine* 72.1 (2014), pp. 33–40.

[27] Dwight G Nishimura. *Principles of magnetic resonance imaging*. Standford Univ., 1996.

[28] Masayuki Kanematsu et al. "Diffusion/perfusion MR imaging of the liver: practice, challenges, and future". In: *Magnetic Resonance in Medical Sciences* 11.3 (2012), pp. 151–161.

[29] Jacques-Donald Tournier, Susumu Mori, and Alexander Leemans. "Diffusion tensor imaging and beyond". In: *Magnetic Resonance in Medicine* 65.6 (2011), p. 1532.

[30] Jacob Ellegood, Chris C Hanstock, and Christian Beaulieu. "Diffusion tensor spectroscopy (DTS) of human brain". In: *Magnetic Resonance in Medicine: An Official Journal of the International Society for Magnetic Resonance in Medicine* 55.1 (2006), pp. 1–8.

[31] Lan Lu et al. "Diffusion-prepared fast imaging with steady-state free precession (DP-FISP): a rapid diffusion MRI technique at 7 T". In: *Magnetic Resonance in Medicine* 68.3 (2012), pp. 868–873.

[32] Aleksandra E Szubert-Franczak et al. "Intravoxel incoherent motion magnetic resonance imaging: basic principles and clinical applications". In: *Polish Journal of Radiology* 85 (2020), e624.

[33] Hugo Alexandre Ferreira and Joana N Ramalho. "Basic principles of time-of-flight magnetic resonance angiography (TOF MRA) and MRV". In: *Vascular Imaging of the Central Nervous System: Physical Principles, Clinical Applications, and Emerging Techniques* (2014), pp. 125–136.

[34] Michael Markl. "Velocity encoding and flow imaging". In: *University Hospital Freiburg, Dept of Diagnostic Radiology, Germany* (2005).

[35] Liliana E Ma et al. "Aortic 4D flow MRI in 2 minutes using compressed sensing, respiratory controlled adaptive k-space reordering, and inline reconstruction". In: *Magnetic Resonance in Medicine* 81.6 (2019), pp. 3675–3690.

[36] VC Rispoli and JLA Carvalho. "Deriving high-resolution velocity maps from low-resolution Fourier velocity encoded MRI data". In: *2013 IEEE 10th International Symposium on Biomedical Imaging*. IEEE. 2013, pp. 334–337.

[37] Julie C DiCarlo et al. "Variable-density one-shot Fourier velocity encoding". In: *Magnetic Resonance in Medicine: An Official Journal of the International Society for Magnetic Resonance in Medicine* 54.3 (2005), pp. 645–655.

[38] M Grade et al. "A neuroradiologist's guide to arterial spin labeling MRI in clinical practice". In: *Neuroradiology* 57 (2015), pp. 1181–1202.

[39] Patricia Clement et al. "A beginner's guide to arterial spin labeling (asl) image processing". In: *Frontiers in Radiology* 2 (2022), p. 929533.

[40] Donald S Williams et al. "Magnetic resonance imaging of perfusion using spin inversion of arterial water." In: *Proceedings of the National Academy of Sciences* 89.1 (1992), pp. 212–216.

[41] John A Detre et al. "Perfusion imaging". In: *Magnetic Resonance in Medicine* 23.1 (1992), pp. 37–45.

[42] Wen-Chau Wu et al. "A theoretical and experimental investigation of the tagging efficiency of pseudocontinuous arterial spin labeling". In: *Magnetic Resonance in Medicine: An Official Journal of the International Society for Magnetic Resonance in Medicine* 58.5 (2007), pp. 1020–1027.

[43] Weiying Dai et al. "Continuous flow-driven inversion for arterial spin labeling using pulsed radio frequency and gradient fields". In: *Magnetic Resonance in Medicine: An Official Journal of the International Society for Magnetic Resonance in Medicine* 60.6 (2008), pp. 1488–1497.

[44] Eric C Wong, Richard B Buxton, and Lawrence R Frank. "Implementation of quantitative perfusion imaging techniques for functional brain mapping using pulsed arterial spin labeling". In: *NMR in Biomedicine: An International Journal Devoted to the Development and Application of Magnetic Resonance In Vivo* 10.4-5 (1997), pp. 237–249.

[45] Nigel P Davies and Peter Jezzard. "Selective arterial spin labeling (SASL): perfusion territory mapping of selected feeding arteries tagged using two-dimensional radiofrequency pulses". In: *Magnetic Resonance in Medicine: An Official Journal of the International Society for Magnetic Resonance in Medicine* 49.6 (2003), pp. 1133–1142.

[46] Jeroen Hendrikse et al. "Flow territory mapping of the cerebral arteries with regional perfusion MRI". In: *Stroke* 35.4 (2004), pp. 882–887.

[47] Richard Werner et al. "Continuous artery-selective spin labeling (CASSL)". In: *Magnetic Resonance in Medicine: An Official Journal of the International Society for Magnetic Resonance in Medicine* 53.5 (2005), pp. 1006–1012.

[48] Greg Zaharchuk et al. "Multislice perfusion and perfusion territory imaging in humans with separate label and image coils". In: *Magnetic Resonance in Medicine: An Official Journal of the International Society for Magnetic Resonance in Medicine* 41.6 (1999), pp. 1093–1098.

[49] Sasitorn Petcharunpaisan, Joana Ramalho, and Mauricio Castillo. "Arterial spin labeling in neuroimaging". In: *World Journal of Radiology* 2.10 (2010), p. 384.

[50] Zhiyong Zhang et al. "DiSpect: Displacement spectrum imaging of flow and tissue perfusion using spin-labeling and stimulated echoes". In: *Magnetic Resonance in Medicine* 86.5 (2021), pp. 2468–2481.

[51] Anthony H Aletras et al. "DENSE: displacement encoding with stimulated echoes in cardiac functional MRI". In: *Journal of Magnetic Resonance (San Diego, Calif.: 1997)* 137.1 (1999), p. 247.

[52] Wesley D Gilson et al. "Complementary displacement-encoded MRI for contrast-enhanced infarct detection and quantification of myocardial function in mice". In: *Magnetic Resonance in Medicine: An Official Journal of the International Society for Magnetic Resonance in Medicine* 51.4 (2004), pp. 744–752.

[53] Leon Axel and Lawrence Dougherty. "MR imaging of motion with spatial modulation of magnetization." In: *Radiology* 171.3 (1989), pp. 841–845.

[54] Frederick H Epstein and Wesley D Gilson. "Displacement-encoded cardiac MRI using cosine and sine modulation to eliminate (CANSEL) artifact-generating echoes". In: *Magnetic Resonance in Medicine: An Official Journal of the International Society for Magnetic Resonance in Medicine* 52.4 (2004), pp. 774–781.

[55] Ilya A Verzhbinsky et al. "Estimating aggregate cardiomyocyte strain using *In Vivo* diffusion and displacement encoded MRI". In: *IEEE Transactions on Medical Imaging* 39.3 (2019), pp. 656–667.

[56] B. Schaller. "Physiology of cerebral venous blood flow: from experimental data in animals to normal function in humans". In: *Brain Research Reviews* 46.3 (2004), pp. 243–260. ISSN: 0165-0173. DOI: https://doi.org/10.1016/j.brainresrev.2004.04.005. URL: https://www.sciencedirect.com/science/article/pii/S0165017304000530.

[57] Andreas Sigfridsson et al. "Spiral readouts for 4D flow MRI". In: *Journal of Cardiovascular Magnetic Resonance* 14.Suppl 1 (2012), W31.

[58] Stephen M Smith. "Fast robust automated brain extraction". In: *Human Brain Mapping* 17.3 (2002), pp. 143–155.

[59] Wei Li, Bing Wu, and Chunlei Liu. "Quantitative susceptibility mapping of human brain reflects spatial variation in tissue composition". In: *Neuroimage* 55.4 (2011), pp. 1645–1656.

[60] Wei Li et al. "A method for estimating and removing streaking artifacts in quantitative susceptibility mapping". In: *Neuroimage* 108 (2015), pp. 111–122.

[61] Chunlei Liu et al. "Quantitative susceptibility mapping: contrast mechanisms and clinical applications". In: *Tomography* 1.1 (2015), pp. 3–17.

[62] Taisuke Harada et al. "Quantitative susceptibility mapping: basic methods and clinical applications". In: *Radiographics* 42.4 (2022), pp. 1161–1176.

[63] Wei Li, Bing Wu, and Chunlei Liu. "STI Suite: A software package for quantitative susceptibility imaging". In: *Proc Int Soc Magn Reson Med*. Vol. 22. 2014, p. 3265.

[64] Michael Lustig et al. "Application of Compressed Sensing for Rapid MR Imaging (2005)". In: *DOI: https://doi. org/10.1002/mrm* 21391 (), pp. 1182–1195.

[65] Joseph Y Cheng et al. "Free-breathing pediatric MRI with nonrigid motion correction and acceleration". In: *Journal of Magnetic Resonance Imaging* 42.2 (2015), pp. 407–420.

[66] G McGibney et al. "Quantitative evaluation of several partial Fourier reconstruction algorithms used in MRI". In: *Magnetic Resonance in Medicine* 30.1 (1993), pp. 51–59.

[67] Vikram S Bajaj et al. "Zooming in on microscopic flow by remotely detected MRI". In: *Science* 330.6007 (2010), pp. 1078–1081.

[68] Juliette A Seeley, Song-I Han, and Alexander Pines. "Remotely detected high-field MRI of porous samples". In: *Journal of Magnetic Resonance* 167.2 (2004), pp. 282–290.

[69] Eric Tranvinh et al. "Contemporary imaging of cerebral arteriovenous malformations". In: *American Journal of Roentgenology* 208.6 (2017), pp. 1320–1330.

[70] Gino Maguida and Ashfaq Shuaib. "Collateral circulation in ischemic stroke: an updated review". In: *Journal of Stroke* 25.2 (2023), p. 179.

[71] Melissa C Brindise et al. "Multi-modality cerebral aneurysm haemodynamic analysis: in vivo 4D flow MRI, in vitro volumetric particle velocimetry and in silico computational fluid dynamics". In: *Journal of the Royal Society Interface* 16.158 (2019), p. 20190465.

[72] Merideth A Addicott et al. "The effect of daily caffeine use on cerebral blood flow: How much caffeine can we tolerate?" In: *Human Brain Mapping* 30.10 (2009), pp. 3102–3114.

[73] Catarina Gaspar et al. "Effects of caffeine on cerebral blood flow". In: *Nutrition* 117 (2024), p. 112217.

[74] Wen Shi et al. "VICTR: Venous transit time imaging by changes in T1 relaxation". In: *Magnetic Resonance in Medicine* (2024).

[75] Elizabeth MC Hillman. "Coupling mechanism and significance of the BOLD signal: a status report". In: *Annual Review of Neuroscience* 37.1 (2014), pp. 161–181.

[76] Adrian T Lee, Gary H Glover, and Craig H Meyer. "Discrimination of large venous vessels in time-course spiral blood-oxygen-level-dependent magnetic-resonance functional neuroimaging". In: *Magnetic Resonance in Medicine* 33.6 (1995), pp. 745–754.

[77] Ravi S Menon et al. "4 Tesla gradient recalled echo characteristics of photic stimulation-induced signal changes in the human primary visual cortex". In: *Magnetic Resonance in Medicine* 30.3 (1993), pp. 380–386.

[78] Yi He et al. "Ultra-slow single-vessel BOLD and CBV-based fMRI spatiotemporal dynamics and their correlation with neuronal intracellular calcium signals". In: *Neuron* 97.4 (2018), pp. 925–939.

[79] Xin Yu et al. "Sensory and optogenetically driven single-vessel fMRI". In: *Nature Methods* 13.4 (2016), pp. 337–340.

[80] Hanzhang Lu et al. "Determining the longitudinal relaxation time (T1) of blood at 3.0 Tesla". In: *Magnetic Resonance in Medicine: an Official Journal of the International Society for Magnetic Resonance in Medicine* 52.3 (2004), pp. 679–682.

[81] Nicholas P Blockley et al. "Measuring venous blood volume changes during activation using hyperoxia". In: *Neuroimage* 59.4 (2012), pp. 3266–3274.

[82] Michael Markl et al. "4D flow MRI". In: *Journal of Magnetic Resonance Imaging* 36.5 (2012), pp. 1015–1036.

[83] Joseph Y Cheng et al. "Comprehensive motion-compensated highly accelerated 4D flow MRI with ferumoxytol enhancement for pediatric congenital heart disease". In: *Journal of Magnetic Resonance Imaging* 43.6 (2016), pp. 1355–1368.

[84] Mohammad Y Chaudhary et al. "Dural arteriovenous malformation of the major venous sinuses: an acquired lesion." In: *American Journal of Neuroradiology* 3.1 (1982), pp. 13–19.

[85] OW Houser et al. "Arteriovenous malformation affecting the transverse dural venous sinus–an acquired lesion." In: *Mayo Clinic Proceedings*. Vol. 54. 10. 1979, pp. 651–661.

[86] J Marc C van Dijk et al. "Clinical course of cranial dural arteriovenous fistulas with long-term persistent cortical venous reflux". In: *Stroke* 33.5 (2002), pp. 1233–1236.

[87] Oh Young Bang, Mayank Goyal, and David S Liebeskind. "Collateral circulation in ischemic stroke: assessment tools and therapeutic strategies". In: *Stroke* 46.11 (2015), pp. 3302–3309.

[88] Markus Barth et al. "Simultaneous multislice (SMS) imaging techniques". In: *Magnetic Resonance in Medicine* 75.1 (2016), pp. 63–81.

[89] Yuxin Hu et al. "Motion-robust reconstruction of multishot diffusion-weighted images without phase estimation through locally low-rank regularization". In: *Magnetic resonance in medicine* 81.2 (2019), pp. 1181–1190.

[90] Yujiao Zhao et al. "Joint denoising of diffusion-weighted images via structured low-rank patch matrix approximation". In: *Magnetic Resonance in Medicine* 88.6 (2022), pp. 2461–2474.

[91] Jichang Zhang et al. "Improved dynamic contrast-enhanced mri using low rank with joint sparsity". In: *IEEE Access* 10 (2022), pp. 121193–121203.

[92] Ricardo Otazo, Emmanuel Candes, and Daniel K Sodickson. "Low-rank plus sparse matrix decomposition for accelerated dynamic MRI with separation of background and dynamic components". In: *Magnetic Resonance in Medicine* 73.3 (2015), pp. 1125–1136.

[93] Frank Ong et al. "Extreme MRI: Large-scale volumetric dynamic imaging from continuous non-gated acquisitions". In: *Magnetic Resonance in Medicine* 84.4 (2020), pp. 1763–1780.

[94] Berkin Bilgic et al. "Accelerated diffusion spectrum imaging with compressed sensing using adaptive dictionaries". In: *Magnetic Resonance in Medicine* 68.6 (2012), pp. 1747–1754.

[95] M Dylan Tisdall et al. "Prospective motion correction with volumetric navigators (vNavs) reduces the bias and variance in brain morphometry induced by subject motion". In: *Neuroimage* 127 (2016), pp. 11–22.

[96] Marshall Xu et al. "VesselBoost: A python toolbox for small blood vessel segmentation in human magnetic resonance angiography data". In: *bioRxiv* (2024), pp. 2024–05.

[97] Adam Hilbert et al. "BRAVE-NET: fully automated arterial brain vessel segmentation in patients with cerebrovascular disease". In: *Frontiers in Artificial Intelligence* 3 (2020), p. 552258.

[98] Rie Aoki and Kittipong Srivatanakul. "Developmental venous anomaly: benign or not benign". In: *Neurologia Medico-chirurgica* 56.9 (2016), pp. 534–543.

[99] Toshiaki Taoka and Shinji Naganawa. "Glymphatic imaging using MRI". In: *Journal of Magnetic Resonance Imaging* 51.1 (2020), pp. 11–24.